Distribution Agreement

In presenting this thesis or dissertation as a partial fulfillment of the requirements for an advanced degree from Emory University, I hereby grant to Emory University and its agents the non-exclusive license to archive, make accessible, and display my thesis or dissertation in whole or in part in all forms of media, now or hereafter known, including display on the world wide web. I understand that I may select some access restrictions as part of the online submission of this thesis or dissertation. I retain all ownership rights to the copyright of the thesis or dissertation. I also retain the right to use in future works (such as articles or books) all or part of this thesis or dissertation.

Signature:

_____ _____

Amanda Reed Dermer Date

Photoelectron Velocity Map Imaging Spectroscopy of Small Beryllium-Containing Anions

By

Amanda Reed Dermer
Master of Science
Chemistry

_____

Michael C. Heaven, Ph. D.
Advisor

_____

James T. Kindt, Ph. D.
Committee Member

_____

Susanna L. Widicus Weaver, Ph. D.
Committee Member

Accepted:

_____

Lisa A. Tedesco, Ph.D.
Dean of the James T. Laney School of Graduate Studies

_____

Date

Photoelectron Velocity Map Imaging Spectroscopy of Small Beryllium-Containing Anions

By

Amanda Reed Dermer
B.S., Erskine College, 2014

Advisor: Michael C. Heaven, Ph. D.

An abstract of
a thesis submitted to the Faculty of the
James T. Laney School of Graduate Studies of Emory University
in partial fulfillment of the requirements for the degree of
Master of Science
in Chemistry
2017

Abstract

Photoelectron Velocity Map Imaging Spectroscopy of Small Beryllium-Containing Anions
By Amanda Reed Dermer

Photoelectron velocity map imaging spectroscopy, also known as slow electron velocity map imaging spectroscopy (SEVI), was used to study small beryllium-containing molecules. The anion to neutral ground state transition, $X\ ^2\Sigma^+ \rightarrow X\ ^1\Sigma^+$, of both BeO^- and BeS^- was studied using a home-built SEVI spectrometer. Rotational constants, electron binding energies, and vibrational intervals were determined experimentally for the first time. The electron binding energy of BeO^- and BeS^- was found to be 2.174 and 2.248 eV, respectively. Upon rotational analysis, it was seen that both species underwent changes in the molecular rotational angular momenta (ΔN = -1, -2, -3 and -4) when the photodetachment energy was near the detachment threshold. Also observed were dipole-bound state transitions, and for BeS^- these transitions (DBS $^2\Sigma^+$, $v' = 0$ – X $^2\Sigma^+$, $v'' = 0$) were measured using autodetachment spectroscopy. Predictions made using electronic structure calculations, performed at the RCCSD(T) and MRCI levels of theory, were found to be in reasonable agreement with experimental results for both species.

The BeO^- and BeS^- produced in the laser ablation source were relatively hot, with several populated vibrational levels (up to $v = 3$). It was decided that it was necessary to add a quadrupole ion trap to the velocity map imaging system to cool the ions to relatively low temperatures, thus decreasing the population in higher vibrational states. Presented in this report are details regarding the design of the quadrupole ion trap system as well as its basic operating principles.

Photoelectron Velocity Map Imaging Spectroscopy of Small Beryllium-Containing Anions

By

Amanda Reed Dermer
B.S., Erskine College, 2014

Advisor: Michael C. Heaven, Ph. D.

A thesis submitted to the Faculty of the
James T. Laney School of Graduate Studies of Emory University
in partial fulfillment of the requirements for the degree of
Master of Science
in Chemistry
2017

Acknowledgements

Enrolling at Emory University in the chemistry Ph. D. program began a new journey in my life. I was leaving my home state and moving away from my family and friends to pursue research and live on my own. Throughout the entirety of this journey, I have had someone who supports me and is always there to talk to me about my stress and life decisions. This person is my rock, support system, and my best friend. My husband, Alexander Dermer, is the reason I decided to attend Emory University to earn a Ph.D. and the reason I am choosing to leave this wonderful place with a Master of Science degree. He helped me realize my passion for the field of Student Affairs and encouraged me to take a risk: leave this program to start a new one for something about which I am passionate. I am grateful that God placed him in my life, and I am thankful and appreciative for all of his support and love.

I must also thank my Savior, Jesus Christ, for He always provides for me. My faith allowed me to survive the graduate school and financial struggles, and knowing God watches out for me helps me move forward and take risks. It may seem cheesy, but I owe everything to Him and am eternally grateful for His love and mercy. I see his miracles working in my life each day, and I know I never need to fear the future for I am in His hands.

My family was also a strong support system in my life, and they alway tell me how proud they are of my accomplishments and have supported me in my endeavors. I would like to especially thank my aunt, Deanna Luvene, as she is a wonderful role model. She is strong, brave, and nurturing. She takes all the problems life throws at her and shapes them

into something great. Deanna and my uncle, Juan Luvene, took me into their home and raised me when I needed it most. They chiseled away bad habits and baggage that I had carried with me, and worked to mold me into a model citizen. I would not be where I am today without them, and I only hope that they know how appreciative I am of their love and kindness. I also must acknowledge my grandmother. She is always encouraging and has watched out for me since I was a child. Her continuous love has helped me push through my graduate studies at Emory University. My parents, along with my step-dad, siblings, and cousins have also had my back and have kept me sane throughout these past few years.

I have made many friends while at Emory University, but I want to especially thank Rachel Kozlowski for being a strong Christian friend who is always ready to goof around or have serious conversations. It is cathartic to complain about our research together, and our long talks about life and hikes in the mountains are always fun and memorable. It has been great getting to know Rachel, and I am appreciative of her friendship. She will make a great Ph.D. chemist and professor one day!

Last but certainly not least, I must thank my research group and advisor. Everyone in the group has been supportive of my abilities and my decisions, but I must extend a special shout-out to Dr. Kyle Mascaritolo as he was my research mentor. I gained many new skills while at Emory University, and he has been instrumental in shaping my lab skills. I also thank Mallory Theis (soon to be Mallory Green!) for her friendship and all our great discussions in and out of the office. Dr. Michael Heaven, my advisor, is the best advisor for which anyone can ask, in my opinion. He is supportive, understanding, and helpful. He challenges his lab students to grow and move forward while setting expectations that are not unattainable. Even though I know he isn't particularly happy to

see me to leave the program, he has supported my choices. His humor is wonderful and his professionalism is welcomed. I am so grateful to have been allowed the opportunity to perform research in his laboratory. Dr. Heaven is everything you need in an advisor and more.

Emory University provided the right atmosphere for my development, and I will cherish the time I had here. Thank you to all the wonderful faculty and staff who helped me along the way (you know who you are)!

Table of Contents

Table of Contents

Listing of Figures

Listing of Figures

Listing of Tables

Chapter 1

Applying Photoelectron Velocity Map Imaging Spectroscopy to the Study of Beryllium-Containing Molecules

Beryllium-containing molecules and beryllium clusters have been attracting more attention over the years, as many applications of these molecules have been discovered along with the strong covalent tendencies beryllium exhibits when bonding. However, few experimental studies have been done on such molecules because beryllium is toxic to humans and can cause berylliosis, a chronic lung disease. The purpose of this chapter is to outline the photoelectron velocity map imaging technique, which was used in this research as a safe and efficient means to study beryllium-containing molecules, and highlight the importance of beryllium studies. The photoelectron velocity map imaging spectrometer used for this research was recently completed in our lab, and the process of designing and fine-tuning this experiment was described in the dissertation of Dr. Kyle Mascaritolo.[1] The reader is referred to this source for more detailed information about the construction and details of the spectrometer.

1.1 Beryllium, Beryllium Clusters, and Beryllium-Containing Molecules

There has been a plethora of studies on beryllium, beryllium clusters, and beryllium-containing molecules, and they can be used in a wide variety of applications.[2-24]

An important motivation for studying beryllium is that its clusters serve as a prototypical series that can be used to answer questions that are essential to understanding metal clusters and their bonding motifs. These questions include, at what size does the cluster begin to obtain characteristics of bulk metal, and how does bonding evolution affect the properties of growing clusters? These questions are especially challenging as the answers depend upon properties that are often difficult to measure, such as electron affinity (EA), geometric structure, bond energies, ionization energy, and the energy gap between the highest occupied molecular orbital (HOMO) and the lowest unoccupied molecular orbital (LUMO).

Beryllium, due to its small atomic radius and high ionization potential (9.32 eV), exhibits unique chemistry with a large degree of covalency when compared to other metals in Group IIA.[10] The small *np*-*ns* energy intervals also contribute to the covalent tendencies of beryllium, and the evolution of covalency is theoretically predicted as the size of a pure beryllium cluster increases. The degree of hybridization increases, and the bond energy substantially increases when the beryllium cluster grows from the dimer to the cyclic trimer. A large increase in the s-p hybridization is also observed. However, other physical properties of the clusters evolve non-monotonically.

It has been demonstrated that a nonrelativistic Hamiltonian is sufficient for studying the Be atom, which indicates that, when paired with large basis sets, high-level computational treatments are plausible methods for studying beryllium clusters. Experimental and theoretical studies have shown that Be_2 has a weak bond with a formal bond order of zero while bulk beryllium exhibits a high melting point and is a hard metal.[11] These findings also indicate nonmonotonic cluster evolution, where many-body

nonadditive forces affect the cluster energies. Electronic structure calculations have predicted that the ionization energy and HOMO-LUMO band gap of Be clusters oscillate in a pattern that is indicative of an electronic shell structure and could be due to the close relationship between the electronic and geometric structure of the clusters.[25-38] Understanding beryllium clusters and determining their properties can shed light on the bonding evolution within metal clusters. Studying these molecules will allow us to improve upon the conventional models describing bonding modes that are currently not well-characterized and provide details about the properties that are relevant and necessary for understanding cluster growth and at what size does the cluster start behaving like the bulk metal.

Although beryllium is a small atom with only four electrons, electron correlation effects can dominate bonding in beryllium compounds, making it a challenge to study computationally.[5,6,10,11,20,22,39-55] New models are needed to more adequately describe the chemistry and properties of beryllium-containing molecules, as these models can improve our ability to use them in a variety of applications. Beryllium-containing molecules have the potential to serve as good candidates for reversible hydrogen storage[12,21], can be used in optoelectronic, microelectronic devices, and nano-devices[14,56-58], has nuclear, electronic, and aerospace applications[59], and can potentially form thermodynamically stable complexes with noble gases.[23] These molecules often behave as Lewis acids[60-70] and can accept protons in systems such as molecules containing multiple hydrogen bonds. There have also been studies that demonstrate that the rhombic isomer of $Be_2O_2^-$ has a large quadrupole moment, indicating it could support a quadrupole-bond state.[71-73] Other molecules, such as BeS^- and BeO^-, exhibit dipole moments strong enough to allow for the

existence of dipole bound states.[48,74-79] Studies have also shown that Be can form half-sandwich complexes[80,81], and BeF can associate to ADP, thus inhibiting the action of certain proteins.[82-88]

Gaining new insight into the bonding and properties of beryllium-containing molecules and beryllium clusters will allow them to be more efficiently used in several applications. The objectives of the research described in this thesis include providing more information to allow for assessment of the theoretical tools that are used to predict the chemistry of Be and gaining a deeper understanding of beryllium-bonding motifs and cluster growth. While there have been a large number of theoretical studies performed on beryllium molecules, there are significantly fewer experimental studies done on these compounds, primarily due to its toxicity to humans and safety protocols. This thesis presents research on beryllium oxide and beryllium sulfide anions and was obtained using the photoelectron velocity map imaging spectroscopy technique.

1.2 Photoelectron Velocity Map Imaging Spectroscopy and its Application to Small Beryllium-Containing Molecules

Photoelectron velocity map imaging spectroscopy (also called slow electron velocity map imaging spectroscopy, SEVI) combines the best properties of photoelectron spectroscopy and zero electron kinetic energy spectroscopy (ZEKE) by employing the velocity map imaging (VMI) detection method, enabling it to overcome many inherent drawbacks of other commonly used photoelectron spectroscopy methods. Eppink and Parker developed the VMI optics in 1997 by replacing the grid electrodes that were commonly used in ion imaging with open-hole electrodes.[89] When used together with

electron photodetachment techniques, these electrodes create an electrostatic lens that maps photodetached electrons, called photoelectrons, with the same initial electron kinetic energy (eKE) onto the same point on a position sensitive detector, regardless of their initial spatial position or ejection angle. These optics improve the eKE, spatial, and temporal resolution over classic electron detection techniques, allowing for vibrationally resolved spectra to be collected for larger molecules than other commonly used methods, such as photoelectron spectroscopy. This technique can achieve single wavenumber resolution, 100% photoelectron collection efficiency, and can record photoelectron angular distributions (PADs). PADs yield information about the electronic and vibronic structure of the molecule being studied.[90-94] Photoelectron velocity map imaging spectroscopy has been extensively described elsewhere[95-103], and thus only a brief overview of the technique will be discussed herein.

Gas-phase ions are mass-selected before being directed into the center of the VMI optics (see Figure 1.1). When they reach the interaction region within the VMI lens the molecules are intersected by a laser fixed at a frequency that lies above the detachment threshold of the ion, causing electron photodetachment. The photoelectrons detach with quantized eKE as described by equation 1.1,

$$eKE = h\upsilon - EA - E_{Internal} \quad (1.1)$$

where $h\upsilon$ is the photon energy of the photodetachment laser, EA is the electron affinity, $E_{Internal}$ represents the internal state energy of the neutral after photodetachment occurs, and eKE is the electron kinetic energy of the photoelectrons. The photoelectrons expand outwards after detachment, forming a cloud-like distribution in space. This cloud consists of Newton spheres[104] whose unique radii correspond to the eKEs (velocities) of the

photoelectrons. Each sphere is composed of photoelectrons with the same quantized eKE. The creation and detection of Newton spheres is detailed in Figure 1.1.

The concentric Newton spheres are accelerated towards and focused on the detector by the electrostatic lens created by the VMI optics. This lens allows for the mapping of all electrons with the same eKE onto the same point of the detector, regardless of their initial spatial position. The Newton spheres flatten onto the detector, generating a 2-dimensional image that is further analyzed. The detector generally consists of a set of microchannel plates paired with a phosphor screen and a charged couple device (CCD) camera.

Once an image is obtained, it is mathematically analyzed to produce a photoelectron spectrum in frequency space. The basis of most methods involves inverse-Abel transformation, which transforms the 2-dimensional image into a 3-dimensional projection by assuming cylindrical symmetry along the axis of polarization of the light used for photodetachment.[105,106] From the intensity pattern of the transformed image, information about the PAD, and thus the anisotropy of the electron velocity distributions, can be determined. A PAD can be approximated by

$$I(\theta)=\frac{\sigma}{4\pi}(1+\beta P_2(\cos\theta)) \tag{1.2}$$

where σ is the photodetachment cross-section, β is the anisotropic parameter ($-1 \leq \beta \leq 2$), $P_2(\cos\theta)$ is the second-order Legendre polynomial, and θ is the emission angle of the electron velocity vector with respect to the laser polarization axis.[90,107]

Photoelectron velocity map imaging spectroscopy is an ideal technique for studying beryllium-containing molecules and clusters because of its capability of providing information about their anisotropy and spectroscopic constants, particularly for larger clusters. Photoelectron velocity map imaging spectroscopy has many advantages over

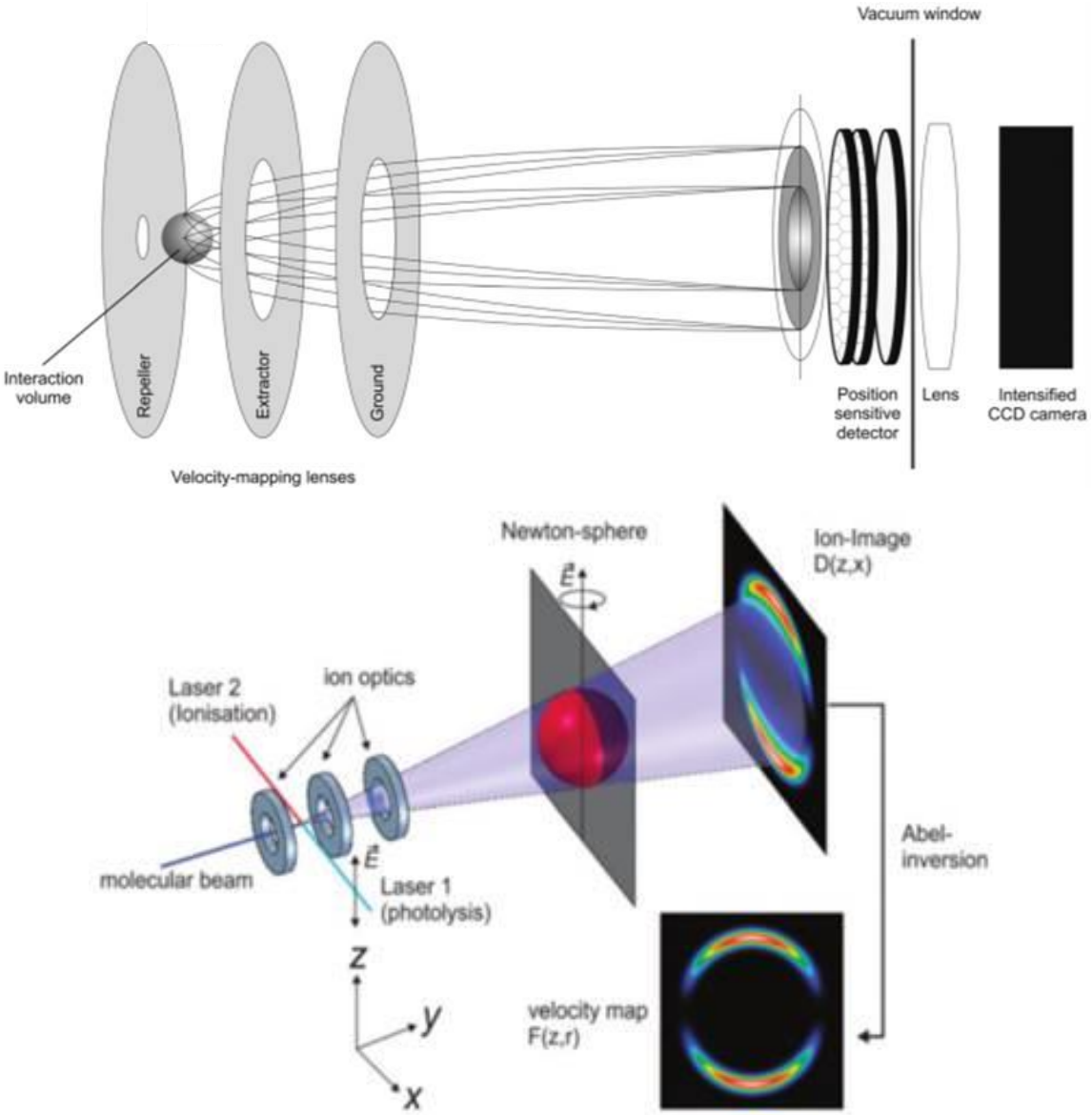

Figure 1.1. Schematics depicting the creation and detection of Newton spheres. Top: Photoelectrons with the same velocity vectors are mapped onto the same point on the detector. Bottom: 3-Dimensional Newton spheres expand concentrically before flattening onto the detector, creating a 2-dimensional image that can be analyzed via Abel-inversion.

photoelectron spectroscopy and ZEKE, two commonly employed gas phase spectroscopies. These advantages include a much higher resolution for both kinetic energy and angular distributions. While the energy resolution of photoelectron spectroscopy is on the order of 5-10 meV, photoelectron velocity map imaging spectroscopy can have a resolution as low as 0.1 cm^{-1}.[101] This value is comparable to that of ZEKE while being much simpler and faster to execute than ZEKE. Also, ZEKE is limited in that it can only observe s-wave electrons because of the very small photodetachment cross-section as dictated by the Wigner threshold law.[95] However, photoelectron velocity map imaging spectroscopy can detect electrons that detach with larger *l* quantum numbers such as p- and d-waves due to the larger above-threshold photodetachment cross-sections. For these reasons, photoelectron velocity map imaging spectroscopy was applied to the study of the BeO and BeS anions in this research as precursors to studying beryllium clusters.

1.3 Perfecting the Velocity Map Imaging Optics

In the initial setup of our photoelectron velocity map imaging spectrometer, the VMI plates were modeled after those used by León and Wang.[108] However, imperfections with the mounting flange welded onto the photodetachment chamber and several issues in perfectly aligning the VMI optics with the detector caused major setbacks to the progress of our research. Also, optimizing the voltages for several plates as required by the León and Wang design proved to be quite challenging. Therefore, the VMI lens was rebuilt using only three plates, such as that used by Neumark et al.[95,103] The new VMI lens setup is shown in Figure 1.2. All other aspects of the spectrometer described by Mascaritolo

remained the same, except for a flexible coupler that replaced the connector between the second and third chamber to allow for easier chamber alignment.

The new VMI optics consisted of a repeller, extractor, and a grounded plate. The plates were made of 304 stainless-steel and their outer diameter was 4.5 in. Each plate was mounted on four ¼ in diameter alumina tubes that had 8-32 aluminum threaded rods inside them. Each plate was separated using 5/8 in alumina spacers. The diameter of the center hole in the repeller plate, which was where the molecular beam passed through to enter the VMI lens, was 1/8 in. This hole was 1 in in diameter for the extractor and grounded plates. Figure 2 displays the schematic of the VMI optics setup.

Care was taken not to have any excess metal material extending into the field free drifting region directly after the VMI optics, because this could cause distortions in the electric field created by the VMI lens. Therefore, in order to ground the third VMI plate, the alumina tubes that served to electrically isolate the three plates were grinded down so that the third plate could make contact with the stainless-steel hex nuts held the plates in place. This setup allowed the third plate to be grounded while remaining electrically isolated from the other two VMI plates.

We also added an extra layer of mu-metal shielding around the VMI plates (not shown in Figure 1.2 for clarity), as we were having problems with stray magnetic fields interacting with the path of the photoelectrons right after detachment. This extra layer was wrapped around the mounting plate (teal plate in Figure 1.2) and secured via a stainless-steel bolt, covering the entire VMI setup. Two holes were cut in the mu-metal shielding to allow the photodetachment laser to travel perpendicularly through the VMI optics. It was this VMI setup that was used to study the BeO and BeS anions, as discussed in Chapters 2

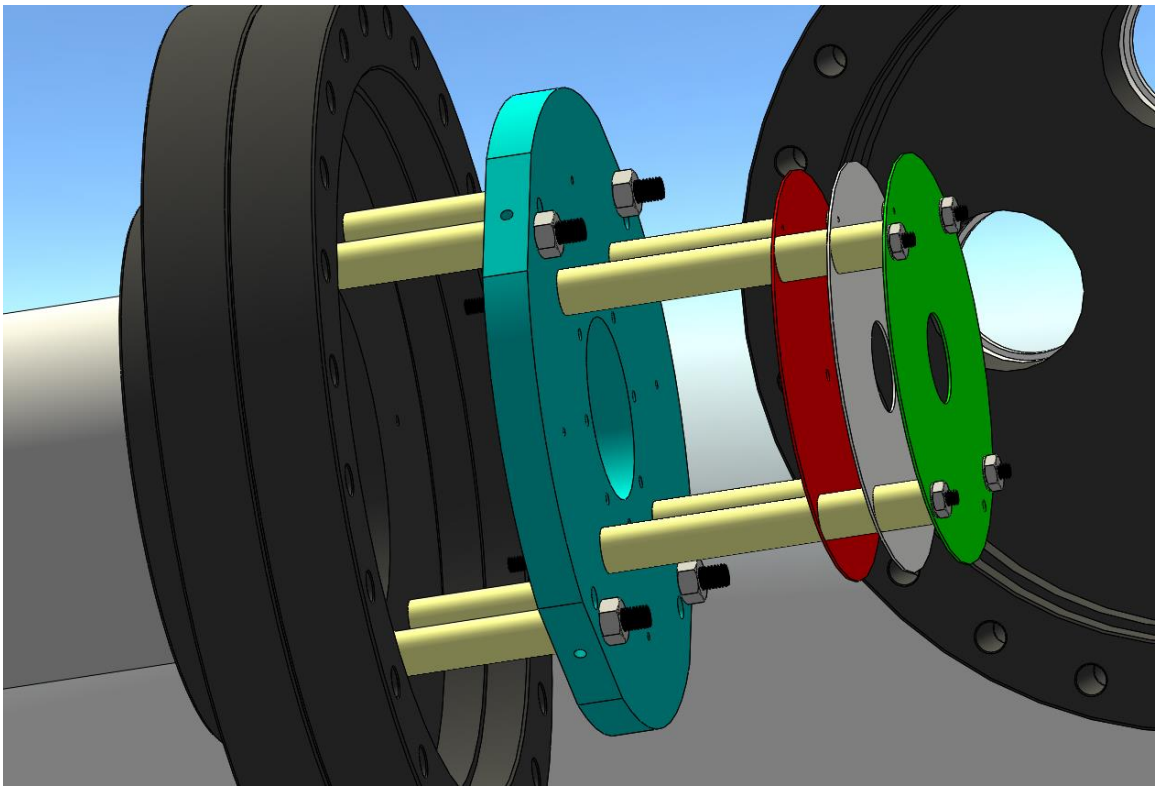

Figure 1.2. The velocity map imaging plates mounted onto the flange of the third chamber. Teal = Mounting plate. Red = Repeller. Gray = Extractor. Green = Ground. Perpendicular photodetachment occurs in the interaction region located in between the repeller and extractor plates.

and 3, respectively.

1.4 Organization of the Remaining Thesis

The next two chapters in this thesis describe the molecules that have been studied using the previously described photoelectron velocity map imaging spectrometer. Chapter 2 discusses the research performed on BeO^-, and Chapter 3 describes the data obtained regarding the BeS anion. Chapter 4 is the final chapter, which describes the importance and process of adding a cold ion trap into our velocity map imaging system after completing the study of BeS^-. A general overview of ion trapping and cooling, as well as using a quadrupole mass filter, will be included. This chapter also contains the design of the ion trap shielding and two new chambers. These chambers were created to accommodate for the installment of the cold ion trap and the new quadrupole mass filter, and they replaced the first (source) chamber in the original spectrometer setup described by Mascaritolo.[1] Following Chapter 4, the thesis is concluded and future work using the spectrometer with the cold ion trap will be discussed.

1.5 References for Chapter 1

1. K. J. Mascaritolo, "A journey towards the construction and operation of a photoelectron velocity map imaging spectrometer," Dissertation, Emory University, 2016.
2. S. Borocci, N. Bronzolino, and F. Grandinetti, Chem. Phys. Lett. **406,** 179 (2005).
3. M. D. Chen, X. B. Li, J. Yang, Q. E. Zhang, and C. T. Au, Intl. J. Mass Spec. **253,** 30 (2006).

4. S. S. Chen, X. H. Pan, W. Chen, H. H. Zhang, W. Dai, P. Ding, J. Y. Huang, B. Lu, and Z. Z. Ye, Appl. Phys. Lett. **105,** 122112 (2014).

5. Z. H. Cui, W. S. Yang, L. Zhao, Y. H. Ding, and G. Frenking, Angew. Chem. Intl. Ed. Engl. (2016).

6. M. El Khatib, G. L. Bendazzoli, S. Evangelisti, W. Helal, T. Leininger, L. Tenti, and C. Angeli, J. Phys. Chem. A **118,** 6664 (2014).

7. G. Frenking, S. Dapprich, K. F. Koehler, W. Koch, and J. R. Collins, Mol. Phys. **89,** 1245 (1996).

8. G. Frenking, W. Koch, J. Gauss, and D. Cremer, J. Am. Chem. Soc. **110,** 8007 (1988).

9. G. L. Gutsev, M. Nooijen, and R. J. Bartlett, Chem. Phys. Lett. **276,** 13 (1997).

10. M. C. Heaven, V. E. Bondybey, J. M. Merritt, and A. L. Kaledin, Chem. Phys. Lett. **506,** 1 (2011).

11. M. C. Heaven, J. M. Merritt, and V. E. Bondybey, Annu Rev Phys Chem **62,** 375 (2011).

12. D. Hwang and A. M. Mebel, Chem. Phys. Lett. **321,** 95 (2000).

13. K. J. Iversen, S. A. Couchman, D. J. D. Wilson, and J. L. Dutton, Coord. Chem. Rev. **297-298,** 40 (2015).

14. J. Jalilian and M. Safari, Phys. Lett. A **380,** 3546 (2016).

15. A. R. D. K. J. Mascaritolo, M. L. Green, A. M. Gardner, M. C. Heaven, J. Chem. Phys. **146** (2017).

16. J. M. Merritt, V. E. Bondybey, and M. C. Heaven, Science **324,** 1548 (2009).

17. H. Motegi, A. Kakizaki, T. Takayanagi, Y. Taketsugu, T. Taketsugu, and M. Shiga, Chem. Phys. **354,** 38 (2008).

18. W. Olovsson, L. Weinhardt, O. Fuchs, I. Tanaka, P. Puschnig, E. Umbach, C. Heske, and C. Draxl, J. Phys. Condens. Matt. **25,** 315501 (2013).

19. L. Ren, L. Cheng, Y. Feng, and X. Wang, J. Chem. Phys. **137,** 014309 (2012).

20. H. F. Schaefer, J. Chem. Phys. **55,** 176 (1971).

21. R. Shinde and M. Tayade, J. Phys. Chem. C **118,** 17200 (2014).

22. M. Šulka, D. Labanc, M. Kováč, M. Pitoňák, I. Černušák, and P. Neogrády, J. Phys. B-Atom. Mol. Opt. Phys. **45,** 085102 (2012).

23. Q. Wang and X. Wang, J. Phys. Chem. A **117,** 1508 (2013).

24. J. H. Yum, T. Akyol, M. Lei, D. A. Ferrer, T. W. Hudnall, M. Downer, C. W. Bielawski, G. Bersuker, J. C. Lee, and S. K. Banerjee, J. Cryst. Growth **334,** 126 (2011).

25. M. L. Cohen, M. Y. Chou, W. D. Knight, and w. A. d. Heer, J. Phys. Chem **91,** 3141 (1987).

26. M. K. Beyer, L. A. Kaledin, M. C. Heaven, and V. E. Bondybey, Chem. Phys. **262,** 15 (2000).

27. S. Srinivas and J. Jellinek, J. Chem. Phys. **121,** 7243 (2004).

28. A. M. Kolchin and R. W. Hall, J. Chem. Phys. **113,** 4083 (2000).

29. V. Cerowski, B. K. Rao, S. N. Khanna, P. Jena, S. Ishii, and e. al., J. Chem. Phys. **123** (2005).

30. R. J. Harrison and N. C. Handy, Chem. Phys. Lett. **123,** 321 (1986).

31. R. A. Whiteside, R. Krishnan, J. A. Pople, M. B. Krogh-Jespersen, P. v. Schleyer, and G. Wenke, J. Comput. Chem. **1,** 307 (1980).

32. P. V. Sudhakar and K. Lammertsma, Chem. Phys. **99,** 7929 (1993).

33. T. J. Lee, A. P. Rendell, and P. R. Taylor, J. Chem. Phys. **92,** 489 (1990).

34. J. S. Lee, J. Phys. Chem. A **109,** 11927 (2005).

35. J. S. Lee, Phys. Rev. A **68** (2003).

36. I. G. Kaplan, S. Roszak, and J. Leszczynski, J. Chem. Phys. **113,** 6245 (2000).

37. I. G. Kaplan, J. N. Murrell, S. Roszak, and J. Leszczynski, Mol. Phys. **100,** 843 (2002).

38. J. M. Junquera-Hernandez, J. Sanchez-Marin, G. L. Bendazzoli, and S. Evangelisti, J. Chem. Phys. **120,** 8405 (2004).

39. J. M. Merritt, V. E. Bondybey, and M. C. Heaven, Science **324** (2009).

40. J. Wang, G. Wang, and J. Zhao, J. Phys. Condens. Matt. **13** (2001).

41. J. Noga and T. Pluta, Chem. Phys. Lett. **264** (1997).

42. B. Pouilly, J. M. Robbe, J. Schamps, R. W. Field, and L. Young, J. Mol. Spec. **96** (1982).

43. J. Watts, M. Urban, and R. Bartlett, Theor. Chim. Acta. **90** (1995).

44. M. Yoshimine, J. Phys. Soc. Jap. **25** (1968).

45. T. E. Sorensen and W. B. England, Intl. J. Quant. Chem. **76** (2000).

46. P. K. Pearson, S. V. O'Neil, and H. F. Schaefer, J. Chem. Phys. **56,** 3938 (1972).

47. C. W. Bauschlicher and D. R. Yarkony, J. Chem. Phys. **72,** 1138 (1980).

48. Y. Yoshioka and K. D. Jordan, J. Chem. Phys. **73,** 5899 (1980).

49. P. Pyykko, G. H. F. Diercksen, F. Mullerplathe, and L. Laaksonen, Chem. Phys. Lett. **141,** 535 (1987).

50. J. Noga and T. Pluta, Chem. Phys. Lett. **264,** 101 (1997).

51. Y. Duan, L. Qin, G. Tang, and L. Shi, Euro. Phys. J. B **66,** 201 (2008).

52. B. P. Prascher, D. E. Woon, K. A. Peterson, T. H. Dunning, and A. K. Wilson, Theor. Chem. Acct. **128,** 69 (2010).

53. T. Larbi, F. Khadri, H. Ghalila, S. Lahmar, and M. Hochlaf, Chem. Phys. **373,** 193 (2010).

54. A. G. S. De Oliveira-Filho, T. V. Alves, V. W. Ribas, L. F. A. Ferrão, O. Roberto-Neto, F. B. C. Machado, and F. R. Ornellas, Intl. J. Quant. Chem. **111,** 1694 (2011).

55. J. W. Mullinax, A. Y. Sokolov, and H. F. Schaefer, J. Chem. Theory Comput. **11,** 2487 (2015).

56. L. B. D. Heciri, S. Drablia, H. Meradji, N.E. Derradji, H. Belkhir, B. Bouhafs, Comput. Mater. Sci. **38** (2007).

57. M. R. D. Rached, N. Benkhettou, R. Khenata, B. Soudini, Y. Al-Douri, H. and Baltache, Comput. Mater. Sci. **37** (2006).

58. N. A. N. Benosman, S. Méçabih, H. Aourag, Phys. B **304** (2001).

59. A. L. Ivanovskii, I. R. Shein, Y. N. Makurin, V. S. Kiiko, and M. A. Gorbunova, Inorg. Mat. **45,** 223 (2009).

60. S. J. Grabowski, J. Mol. Struct. **553,** 151 (2000).

61. F. Holleman, N. Wiberg, and E. Wiber, *Inorganic chemistry* (Academic Press, Cambridge, 2001).

62. C. Housecroft and A. G. Sharpe, *Inorganic chemistry*, 3rd ed. (Prentice Hall, New York, 2008).

63. M. P. Dressel, S. Nogai, R. J. F. Berger, and H. Z. Schmidbaur, Naturforsch (B) **58,** 173 (2003).

64. B. Neumuller, W. Petz, and K. Dehnicke, Z. Anorg. Allg. Chem. **634,** 662 (2008).

65. B. Neumuller, F. Weller, and K. Dehnicke, Z. Anorg. Allg. Chem. **629,** 2195 (2003).

66. B. Neumuller and K. Dehnicke, Z. Anorg. Allg. Chem. **629,** 2529 (2003).

67. B. Neumuller and K. Dehnicke, Z. Anorg. Allg. Chem. **630,** 347 (2004).

68. B. Neumuller and K. Dehnicke, Z. Anorg. Allg. Chem. **630,** 369 (2004).

69. B. Neumuller and K. Dehnicke, Z. Anorg. Allg. Chem. **630,** 799 (2004).

70. S. Metz, M. C. Holthausen, and G. Frenking, Z. Anorg. Allg. Chem. **132632,** 814 (2002).

71. M. Gutowski and P. Skursk, Chem. Phys. Lett. **303,** 65 (1999).

72. K. D. Jordan and J. F. Liebman, Chem. Phys. Lett. **62,** 143 (1979).

73. G. L. Gutsev, P. Jena, and R. J. Bartlett, I. J. Chem. Phys. **111,** 504 (1999).

74. G. L. Gustev, M. Nooijen, and R. J. Bartlett, Chem. Phys. Lett. **176** (1997).

75. I. Adamovicz and E. A. J. McCollough, Chem. Phys. Lett. **107** (1984).

76. Y. Yoshioka and K. D. Jordan, Chem. Phys. **56** (1981).

77. K. D. Jordan, J. Chem. Phys. **65,** 1214 (1976).

78. K. Lykke, R. Mead, and W. Lineberger, Phys. Rev. Lett. **52,** 2221 (1984).

79. K. D. Jordan and F. Wang, Ann. Rev. Phys. Chem. **54,** 367 (2003).

80. P. Barbaro, F. Cecconi, D. Dakternieks, S. Dominguez, A. Duthie, C. A. Ghilardi, S. Midollini, A. Orlandini, and A. Vacca, Inorg. Chem. **40,** 2725 (2001).

81. M. D. Conejo, R. Fernandez, E. Carmona, R. A. Andersen, E. Gutierrez-Puebla, and M. A. Monge, Chem. - Eur. J. **9,** 4462 (2003).

82. X. R. Chen, J. Grammer, J. D. Lawson, R. Cooke, E. Pate, and R. G. Yount, Biochemistry **41,** 2609 (2002).

83. H. Shibuya, K. Kondo, N. Kimura, and S. J. Maruta, Biochem. **132,** 573 (2002).

84. S. Danko, K. Yamasaki, T. Daiho, and H. Suzuki, J. Biol. Chem. **279,** 14991 (2004).

85. Z. E. Sauna, K. Nandigama, and S. V. Ambudkar, J. Biol. Chem. **281,** 26501 (2006).

86. T. Tiago, S. Simao, M. Aureliano, F. J. Martin-Romero, and C. Gutierrez-Merino, Biochemistry **45,** 3794 (2006).

87. J. Orban, D. Lorinczy, G. Hild, and M. Nyitrai, Biochemistry **47,** 4530 (2008).

88. F. Liu, A. Putnam, and E. Jankowsky, Proc. Natl. Acad. Sci. USA **105,** 20209 (2008).

89. A. T. J. B. Eppink and D. H. Parker, Rev. Sci. Instrum. **68,** 3477 (1997).

90. J. Cooper, J. Chem. Phys **48,** 942 (1968).

91. D. Hanstorp, C. Bengtsson, and D. J. Larson, Phys. Rev. A **40,** 670 (1989).

92. K. L. Reid, Annu Rev Phys Chem **54,** 397 (2003).

93. A. Sanov, Ann. Rev. Phys. Chem. **65,** 341 (2014).

94. X.-P. Xing, X.-B. Wang, and L.-S. Wang, J. Chem. Phys. **130,** 074301 (2009).

95. E. Garand, J. Zhou, and D. M. Neumark, in *Slow photoelectron velocity map imaging spectroscopy*, Ohio State University, 2007 (Ohio State University).

96. C. Hock, J. B. Kim, M. L. Weichman, T. I. Yacovitch, and D. M. Neumark, J. Chem. Phys. **137,** 244201 (2012).

97. J. B. Kim, C. Hock, T. I. Yacovitch, and D. M. Neumark, J. Phys. Chem. A **117,** 8126 (2013).

98. J. B. Kim, T. I. Yacovitch, C. Hock, and D. M. Neumark, Phys. Chem. Chem. Phys. **13,** 17378 (2011).

99. W. C. Lineberger, Annu. Rev. Phys. Chem. **64,** 21 (2013).

100. D. M. Neumark, J. Phys. Chem. A **112,** 13287 (2008).

101. A. Osterwalder, M. J. Nee, J. Zhou, and D. M. Neumark, J. Chem. Phys. **121,** 6317 (2004).

102. M. L. Weichman, J. B. Kim, and D. M. Neumark, J. Chem. Phys. **140** (2014).

103. J. Zhou, E. Garand, and D. M. Neumark, J. Chem. Phys. **127,** 114313 (2007).

104. B. Dick, Phys. Chem. Chem. Phys. **16,** 570 (2014).

105. E. W. Hansen and P. L. Law, J. Opt. Soc. America A **2,** 510 (1985).

106. S. Manzhos and H. P. Loock, Comput. Phys. Comm. **154,** 76 (2003).

107. C. N. Yang, Phys. Rev. **74,** 764 (1948).

108. I. Leon, Z. Yang, H. T. Liu, and L. S. Wang, Rev. Sci. Instrum. **85,** 083106 (2014).

Chapter 2

Photodetachment Spectroscopy of the Beryllium Oxide Anion, BeO^-

The $X\ ^2\Sigma^+ \rightarrow X\ ^1\Sigma^+$ anion to neutral ground state photodetachment of BeO^- has been studied by means of photoelectron velocity map imaging spectroscopy in a newly constructed apparatus. Vibrational intervals, rotational constants, and the electron detachment threshold of BeO^- were determined for the first time. The small moment of inertia of beryllium oxide allowed for the observation of partially resolved rotational contours. Analyses of these contours provided evidence of several detachment channels resulting from changes in molecular rotational angular momenta of $\Delta N = 0, \pm1, \pm2$, and ±3. The relative intensities of these detachment channels were found to be a function of the electron kinetic energy. Experimental results are compared to the predictions of high level *ab initio* calculations.

2.1 Introduction

The chemistry of beryllium is known to be significantly different from the behavior exhibited by the heavier group IIA elements.[1-13] In part, this is due to the high ionization energy (9.32 eV) and small radius of Be. As a consequence, the bonds formed by Be have appreciably more covalent character. Theoretical techniques have often been used to explore Be chemistry, conveniently circumventing the toxicity issues (see, for example [1]

and references therein). At first glance, Be seems to be well suited for investigation using non-relativistic quantum chemical methods. It is a light element with just four electrons. However, calculations for Be-compounds often prove to be difficult, with the Be_2 dimer being a celebrated example.[14-23] Problems arise because the bonds involving Be can be dominated by electron correlation, such that they include significant contributions from doubly excited electron configurations.

Diatomic beryllium oxide (BeO) is a prototypical species for studies of Be bonding. It has been the subject of both spectroscopic and theoretical investigations.[24-38] Based on theoretical calculations, Frenking and co-workers[6,39-41] have noted that BeO is an extraordinarily strong Lewis acid, with the ability to attract He with a bond energy of 1500 cm^{-1}. This prediction has been supported by subsequent theoretical studies.[42,43] Similarly, electronic structure calculations indicate that the electron affinity of BeO is relatively large (2.1 – 2.2 eV).[44,45] The electron binding energy is high enough for the BeO^- anion to support both valence and dipole-bound electronically excited states. The latter are stabilized by the 6.26 D permanent dipole moment of BeO.[44] To date, there have been no published experimental studies of BeO^-.

In the present work we have used anion photodetachment spectroscopy to determine the electron affinity of BeO, and molecular constants for the ground state of BeO^-. This effort was motivated by interest in testing the previous theoretical predictions for BeO^-, and to provide data for further testing and refinement of the quantum chemistry models used for anions. Looking beyond these immediate objectives, this will be the first step towards studies of larger Be_nO_m clusters by means of anion photodetachment techniques. Studies of such clusters can reveal the degree of covalency and some of the

unique electrostatic binding capabilities of small beryllium oxide species. For example, theoretical calculations predict that $(BeO)_n$ clusters can be used as a lightweight, reversible storage medium for H_2. [8,13,46] Hence, in addition to the fundamental science questions, work on the oxide clusters relates to potential practical applications of these materials.

2.2 Experimental Procedure and Spectrometer Description

The data presented here were recorded using photoelectron velocity map imaging spectroscopy. The details of the technique have been described extensively in other publications.[47-49] The imaging apparatus used in this study was modified from an existing setup described elsewhere.[50] Only the new additions to the current spectrometer are discussed in detail here.

Figure 2.1 shows a diagram of the apparatus used to study BeO^-. Anions were produced in a laser ablation source[51] using a beryllium rod target and the focused, frequency doubled output of a Nd:YAG laser (532nm, ~8mJ). This source was coupled to a pulse valve that delivered 70%/30% Ne/He carrier gas seeded with 2.5% N_2O at a backing pressure of 55 psia. The anions produced by the ablation process were supersonically expanded into a differentially pumped vacuum chamber, where a Wiley-McLaren time of flight mass spectrometer (WM-TOFMS)[52], in a perpendicular orientation with respect to the direction of the expansion, was housed. Fast rising, negative pulsed voltages were applied to the repeller and extractor of the WM-TOFMS by high voltage switches, accelerating the anions into a drift region to allow for mass separation before reaching the photodetachment region of the velocity map imaging optics. The resolution of the mass spectrometer was $m/\Delta m = 690$ at masses around 40 amu.

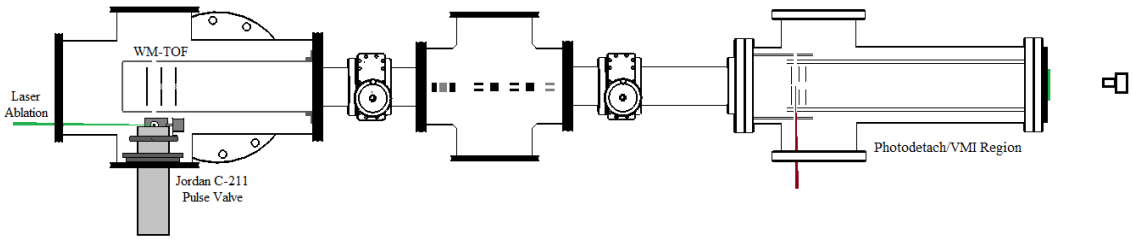

Figure 2.1. Schematic of the photoelectron velocity map imaging spectrometer. Figure drawn to scale. WM-TOF: Wiley-McLaren Time of Flight, VMI: Velocity map Imaging

Along the flight-path of the anions from the WM-TOFMS, an Einzel lens and four sets of deflector plates were used to focus and guide the anions into the velocity map imaging (VMI) optics. Additionally, a fifth set of deflector plates could be pulsed to act as a mass gate to only allow the anion of interest to enter the detachment region. One plate of each pair was grounded while the opposite plate was connected to a dual polarity voltage source.

Once inside the VMI optics, the mass selected anions were intercepted by the polarized, focused output of a Nd:YAG pumped dye laser or an excimer pump dye laser operating at a photon energy above the detachment threshold of the species of interest. Typical detachment laser pulse energies were in the range of 0.5 – 1.0 mJ, with a beam diameter of < 2 mm. The dye laser linewidths were approximately 0.3 cm^{-1} (FWHM). Wavelength calibrations of the lasers were established using the gas phase absorption spectrum of the B – X transition of room temperature I_2. The absolute energies of the I_2 lines were taken from the PGOPHER software package.[53]

The velocity map imaging electrodes were replicated from the original Eppink and Parker design[49] using 1/16 in thick 304 stainless steel. The photoelectrons produced within the VMI lens were accelerated down a 66 cm long drift region, shielded from external electric and magnetic fields by layers of mu-metal, to the detector (Photonis USA, Inc. 75 mm Chevron stacked microchannel plates (MCP) with a fiberoptic P47 phosphor screen). Images from the detector screen were recorded by a CCD camera (Physimetrics UI-2230SE-M-GL, 1024x768). The photodetached electrons were discriminated from all other charged particles by pulsing the voltage (gain) on the MCPs at the appropriate arrival time. Individual cycles of the experiment were recorded and summed over several hundred

thousand laser pulses to produce an image. The final image was saved using the imaging collection software developed by Li et al.[54]. Transformation of the image from velocity space to energy was done using the Maximum Entropy Velocity Legendre Reconstruction (MEVELER) technique[55]. The total emission of the screen from electron or anion impacts could also be monitored with a photomultiplier tube positioned off axis from the camera (not shown in Figure 1). This mode of detection produced a TOF-MS spectrum, and was extremely useful in the optimization of anion and photoelectron production. The repetition rate of the experiment was 10 Hz. All images were calibrated using the known transitions from detachment of the sulfur anion, S^-.[56-58]

2.3 Electronic Structure Calculations

The ground state electronic configurations of BeO and BeO^- are easily anticipated. BeO is a closed-shell ionic species with an experimentally verified $X^1\Sigma^+$ ground state. The unpaired electron of BeO^- resides in an orbital that is primarily of Be 2*s* character, giving rise to a $X^2\Sigma^+$ ground state. Electronic structure calculations were performed on both the anion and neutral beryllium oxide molecules. This was done to assist in the assignment of the spectra, and to evaluate the suitability of the chosen electronic structure methods for treatment of this prototypical small molecular anion. For both beryllium and oxygen, the aug-cc-pwCVXZ (X = T, Q, 5) basis sets were employed, denoted by awCVXZ herein. A second set of diffuse functions was added to these basis sets in order to better describe the diffuse nature of the BeO^- frontier orbitals. The exponents of the diffuse functions were determined from an even-tempered expansion of the two lowest exponent functions of the awCVXZ basis sets. The resulting basis sets are denoted d-awCVXZ in the following.

All calculations were performed with the MOLPRO suite of programs.[59] Potential energy curves (PECs) were calculated, pointwise, by means of the partially spin adapted coupled cluster method including single and double excitations and perturbative corrections for triple excitations (RCCSD(T)), and the complete active space self-consistent field followed by multireference configuration interaction (CASSCF+MRCI+Q) levels of theory. The PECs are shown in Figure 2.2. In the RCCSD(T) calculations, all electrons were included in the correlation treatment. The active space in the CASSCF calculations consisted of the 2*s* and 2*p* orbitals of both Be and O, while the "core" orbitals, which are linear combinations of the 1*s* atoms orbitals, were constrained to be doubly occupied. Their wavefunctions were optimized in the CASSCF procedure to aid convergence. For both the anion and neutral BeO species, all electrons were included in the correlation treatment of the subsequent MRCID calculation in an attempt to recover the core-valence correlation energy. The Davidson correction was applied in order to partially compensate for the size inconsistency of the MRCI calculations. Total RCCSD(T) and MR-CISD interaction energies were extrapolated to estimate the complete basis set limit using the two point formula of Halkier *et al*.[60] (referred to as d-aV(Q,5)Z). The bound ro-vibrational levels of the resulting PECs were calculated using the LEVEL 8.0 program.[61] The lowest vibrational energy levels were least squares fit to the standard Morse energy level expression, yielding effective values for ω_e and $\omega_e x_e$. Predictions for the electron affinity were made with the inclusion of the zero point vibrational energies.

Initially, restricted Hartree – Fock RCCSD(T) (RHF-RCCSD(T)) calculations were carried out for the expected $^2\Sigma^+$ ground state of BeO^-. Although the T_1 diagnostic, a commonly employed test of the degree of multi-reference character of the electronic

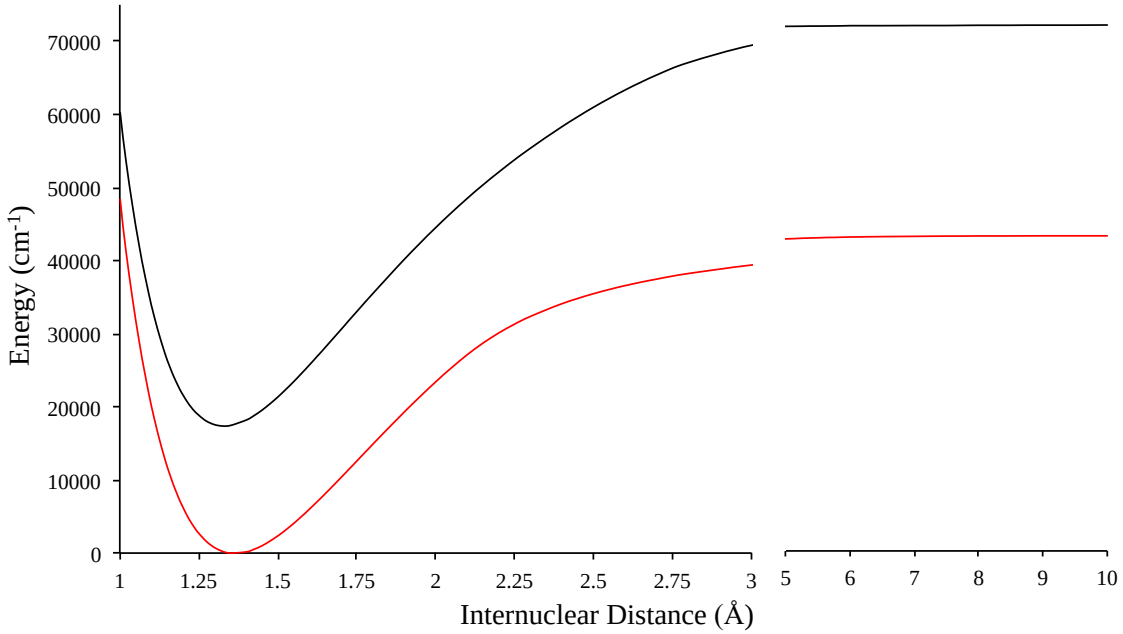

Figure 2.2. Potential energy curves of the ground states of BeO^- (red) and BeO (black). See text for details.

wavefunction, had values of ~0.022 at internuclear separations in the vicinity of the equilibrium bond length of the anion (1.3-1.5 Å), it increased to ~0.04 at an internuclear separation of 1.8 Å. Additionally, convergence of the RHF wavefunction became unstable at longer bond lengths. Values of the T_1 diagnostic lying above 0.044 suggest distinctly multi-reference character. The T_1 diagnostic examines amplitudes of single excitation in the RCCSD procedure, based on a given self-consistent field (SCF) wavefunction. Large values of the T_1 diagnostic may be obtained when the reference wavefunction is a poor description of the electronic state of interest, and therefore large amplitude single electron excitations are apparent in the more representative RCCSD wavefunction (note that CCSD calculations using a spin unrestricted reference wavefunction are not supported by MOLPRO). As an alternative, initial wavefunctions obtained from a B3LYP (Becke, three-parameter, Lee-Yang-Parr exchange-correlation functional) calculation were used in subsequent RCCSD and RCCSD(T) calculations. These calculations displayed well-behaved convergence at internuclear separations of 1-50 Å, with values for the T_1 diagnostic below 0.04 being obtained at internuclear separation between 1.0 – 5 Å. This method is referred to as B3LYP-RCCSD(T) later in the discussion section.

The results from calculations for both BeO and BeO^- are presented in Table 2.1. The predictions for BeO are in good agreement with previous theoretical calculations and reasonably close to the experimental data. The equilibrium bond length was within the experimental error range, while the harmonic vibrational frequency was slightly overestimated. Our calculations for BeO^- are also in agreement with earlier theoretical studies[44,45]. The additional electron, which primarily resides in the Be 2*s* orbital, causes the bond to lengthen and the vibrational frequency to decrease by approximately 100 cm^{-1}.

Table 2.1. Experimental and theoretical spectroscopic parameters for BeO^- and BeO. All values are in units of wavenumbers (cm^{-1}), expect R_e which is given in Angstroms.

BeO			
	Exp.[26]	B3LYP-CCSD(T)	MRCI
ω_e	1487.32	1493.5	1502.7
$\omega_e x_e$	11.83	11.2	11.6
R_e	1.331	1.330	1.329

BeO^-				
	Exp.	RHF-RCCSD(T)	B3LYP-RCCSD(T)	MRCI
eBE	17535 ± 15		17487	17236
ω_e	1386 ± 10	1397.4	1394.2	1397.6
$\omega_e x_e$	9.9 ± 2	9.9	9.7	10.9
$\Delta G_{1/2}$	1367 ± 7	1377.6	1374.8	1375.8
$\Delta G_{3/2}$	1348 ± 5	1357.8	1355.4	1354
$\Delta G_{5/2}$	1325 ±10	1338.0	1336.0	1332.2
$\Delta G_{7/2}$	1305 ± 5	1318.2	1316.6	1310.4
$\Delta G_{9/2}$	1287 ± 5	1298.4	1297.2	1288.6
$\Delta G_{11/2}$	1273 ± 5	1278.6	1277.8	1266.8
$\Delta G_{13/2}$	1250 ± 5	1258.8	1258.4	1245
$\Delta G_{15/2}$	1225 ± 5	1239	1239	1223.2
R_e				1.364
B_e				1.568
α_e				0.017
D_e				8.39×10^{-6}
β_e				6.13×10^{-7}

Lastly, the vertical electron detachment energy is predicted to be in the range of 17200 – 17500 cm^{-1} (2.13 - 2.17 eV).

2.4 Experimental Results and Discussion

Figure 2.3 shows photodetachment spectra for BeO^-, obtained by analyses of velocity map images. All of the stronger features in the images yielded near isotropic electron angular distributions. The horizontal scale for these spectra, labeled as transition energy, is the photon energy minus the electron kinetic energy. The traces correspond to images recorded using photon energies of 18110.48, 17733.93, 16744.75 cm^{-1}, and 16359.34 cm^{-1}, respectively. Note that the intensities of the four spectra were scaled for presentation purposes. Comparisons of intensities for spectra recorded using different detachment energies are not meaningful. However, the relative intensities of features within a single spectrum are valid.

Traces A and C combined show three groups of features. The analysis of trace A, which was recorded with the highest energy photons, is the most straightforward. Based on the molecular constants given in Table 2.1, the features in the 17400 – 18000 cm^{-1} range are consistent with the $\Delta\upsilon$ = 0; 0 – 0, 1 – 1, 2 – 2, 3 – 3 sequence bands. Similarly, the bands in the 16000-16700 cm^{-1} range (trace C) are the Δv = -1; 0 – 1, 1 – 2, 2 – 3, 3 – 4 transitions, while the bands in the 14600 – 15700 cm^{-1} range are the Δv = -2; 0 – 2, 1 – 3, …6 – 8 transitions. Clearly there was appreciable population of the excited vibrational states of the anion. Note that the Δv = -2 features of traces C and D show more extended vibrational sequence structure than the Δv = -1 and 0 features. Franck-Condon factor (FCF) calculations, based on the theoretical potential energy curves, account for this behavior.

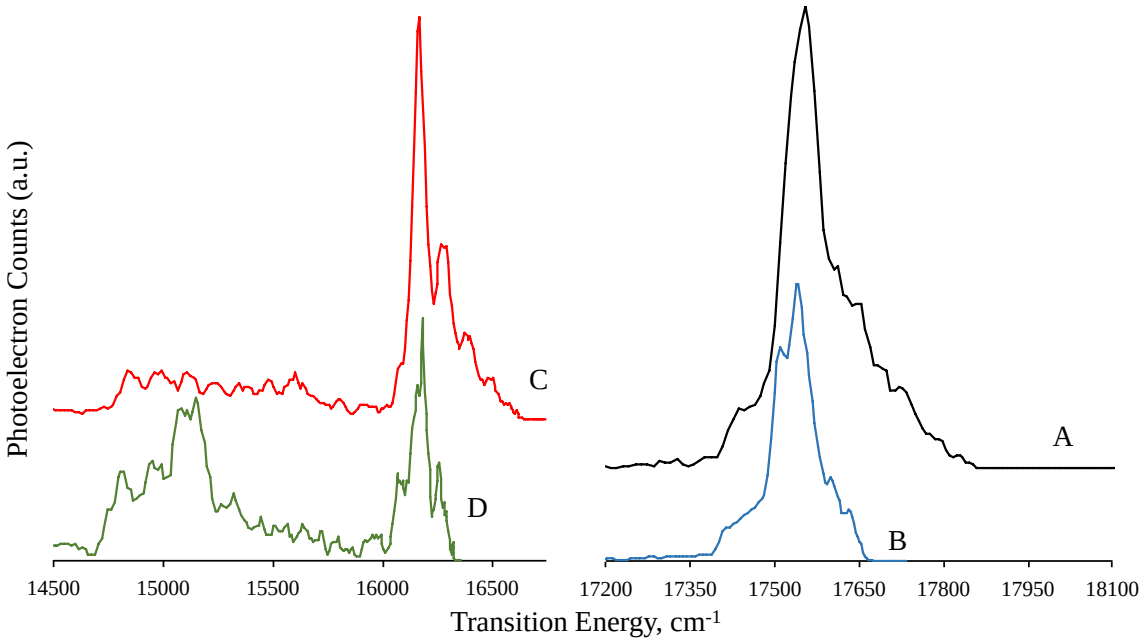

Figure 2.3. Photodetachment spectra of BeO^- at photon energies (A, black) 18110.5 cm^{-1}, (B, blue) 17733.9 cm^{-1}, (C, red) 16744.8 cm^{-1}, and (D, green) 16359.3 cm^{-1}. The transition energy is defined as hν – eKE.

The 0-0 band is predicted to have the highest FCF for the $\Delta v = 0$ group, while the FCF maximum for the $\Delta v = -2$ was for the 3-5 band. Another interesting detail of the $\Delta v = -2$ bands was the marked difference in the contours of traces C and D at energies near 15125 cm^{-1}. The reason for this anomaly will be considered following the analysis that yields the EA of BeO.

The intensity contours of the photodetachment bands were found to be significantly dependent on the excess energy imparted to the electron (with some random fluctuations caused by day-to-day variations in the laser ablation source). For example, traces A and B of Figure 2.3 were recorded using energies that differed by 376.6 cm^{-1}. As the photon energy was lower for trace B, the slightly higher resolution was expected. However, the shift in the peak positions was not anticipated. Modeling of the rotational contours provided an explanation for this effect. With higher energy photodetachment, the band contours were dominated by detachment events where there was no change in the rotational angular momentum (i.e., $\Delta N = 0$, where N is the Hund's case (b) quantum number for the angular momentum, exclusive of spin). When the photon energy was closer to the detachment threshold, transitions with ΔN = - 1, - 2, and - 3 became increasingly more important. Figure 2.4 shows an expanded view of trace B, along with a rotational structure simulation described by Equation 2.1.

$$I_v = P_{v''} \sum_T I(v) = \sum_{v',N',v'',N''} A_{\Delta N} P_{v'',N''} G[v - v_0(v', N', v'', N'')] \sigma(eKE) \qquad (2.1)$$

where $v_0(v', N', v'', N'')$ is the threshold energy required to detach an electron from BeO^- in ro-vibration state v'', N'' and produce the neutral molecule in state v', N'. This energy is defined by the expression

$$v_0(v', N', v'', N'') = EA + E(v', N') - E(v'', N'') \qquad (2.2)$$

where EA is the electron affinity of BeO and the ro-vibrational energies are given by

$$E(\mathrm{v}, N) = \omega_e \mathrm{v} - \omega_e x_e \mathrm{v}(\mathrm{v}+1) + B_\mathrm{v} N(N+1) - D_\mathrm{v}(N(N+1))^2 \quad (2.3)$$

Each transtion was assigned a Gaussian line shape

$$G[\nu - \upsilon_0] = \sqrt{\frac{2}{\pi}}\frac{1}{\Gamma}\exp\left[-2\left(\frac{\upsilon-\upsilon_0}{\Gamma}\right)^2\right] \quad (2.4)$$

with a linewidth of $\Delta\nu$ (FWHM) and $\Gamma = \Delta\nu/2\ln 2$. $P_{v'',N''}$ is the ro-vibrational Boltzmann population distribution function for anion ground state. $A_{\Delta N}$ is an intensity scaling constant for transitions with like changes in rotational angular momentum. Lastly, *σ(eKE)* is a Wigner threshold law factor[62] simplified here as $\sigma(eKE) = eKE^{l+1/2}$, where *eKE* is the kinetic energy of the ejected electron. σ was implemented in Eq. 1 to simulate the overall intensity profiles of the images. A value of $l = 2$ was found to best represent the intensity profiles based on experimentally reasonable values found for $A_{\Delta N}$ and $P_{v'',N''}$. We do not attribute physical meaning to *l* and consider it to be no more than a convenient model parameter. However, $l = 2$ does have the effect that there will be almost no signal from photodetachment processes that are very close to threshold. Consequently, transitions where the electron kinetic energy can be increased by transferring rotational energy from the molecule (negative ΔN processes) will become favored as the energy threshold for the $\Delta N = 0$ processes is approached.

The input data for the simulation consisted of the literature values for the molecular constants of BeO, and BeO^- rotational constants derived from our theoretical calculations (Table 2.1). The vibrational term energies of BeO^-, the electron binding energy, and the rotational temperature were treated as variable parameters. As indicated in Figure 2.4, the sharpest features of trace B corresponded to the P- and Q-branch band heads, with a lower

energy feature arising from the O-branch band head. The rotational temperature of this simulation was 750 K.

At present we do not have a model that accounts for the dependence of the final rotational state propensities on the kinetic energy of the departing electron. We speculate that slower moving electrons may permit a longer interaction time for rotational state mixing.

The contours of the Δv = -1 sequence bands, recorded using a detachment photon energy of 16744.75 cm^{-1}, were consistent with predominantly ΔN = 0 transitions, as were the Δv = -2 bands. However, the 0 – 1 band ΔN = -2 feature is observed near 16070 cm^{-1}. The intensity pattern for this Δv = -1 group was quite similar to that of the Δv = 0 sequence bands, as they appear in trace A. Note that the electron kinetic energies (energies above observed thresholds) probed in traces A and C were comparable. Likewise, when using photon energies close to threshold (traces B and D), the resulting images have similar rotational contours.

Simulations, like that shown in Figure 2.4, were carried out for all four traces shown in Figure 2.3. The most important fitting parameters were the anion vibrational term energies, the electron affinity of BeO, and the rotational temperature. These fits defined an electron affinity (detachment threshold) of 17535 ± 15 cm^{-1} (2.1741 ± 0.0019 eV) and the anion vibrational intervals listed in Table 2.1. Rotational temperatures between 600 and 750 K gave reasonable simulations. The rotational constants from the *ab initio* calculations (Table 2.1) were consistent with the observed spectrum, and could not be further refined due to the limited resolution of the experimental data. It is believed that the calculated anion rotational constants are close to the true values based on the good agreement between

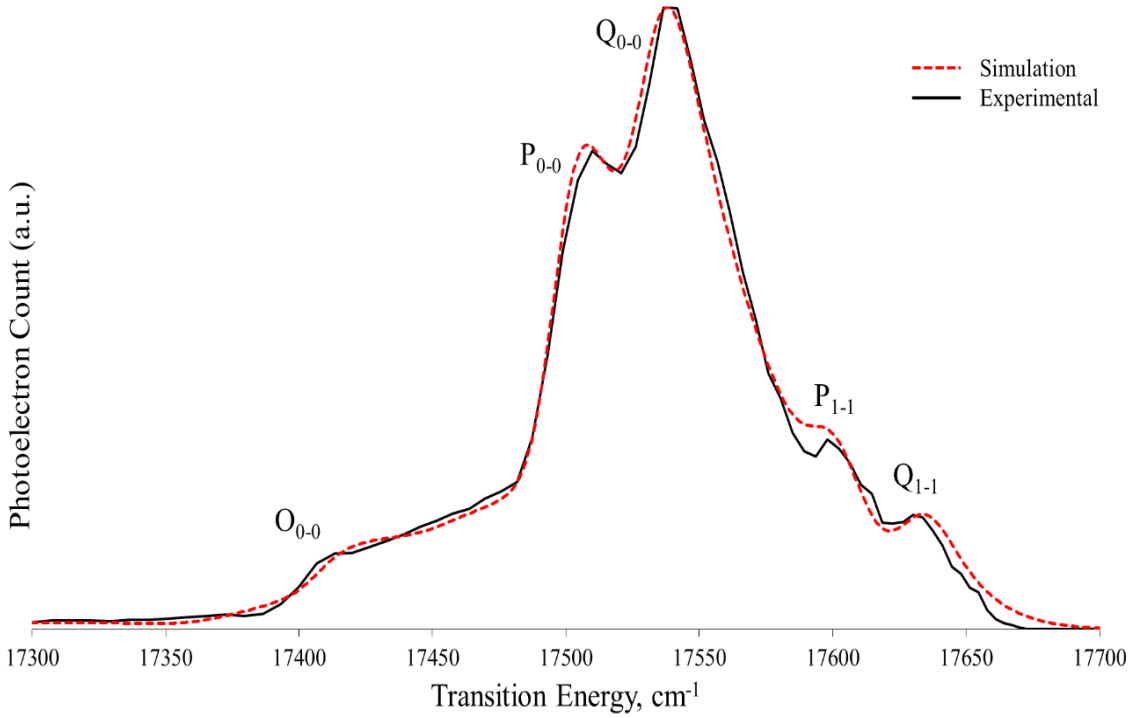

Fig. 2.4: Photodetachment spectrum (solid, black) and simulation (dashed, red) of the $\Delta\upsilon = 0$ region of BeO^- versus transition energy. Detachment photon energy was 17733.93 cm^{-1}. Transition Energy is defined as $h\nu$ – eKE.

theory and experiment in the $\Delta G_{v+1/2}$ values and the electron affinity. Previous theoretical predictions from Jordan *et al.*[45] (2.162 eV) and Gutsev *et al.*[44] (2.15 eV) are also in agreement with the measured electron affinity.

Lastly, we return to the intensity anomaly exhibited near 15125 cm^{-1} within the Δv = -2 group of trace D. The anomaly corresponds to the 2-4 band and it is most likely caused by the accidental excitation of the $BeO^-(v = 3)$ dipole bound state, which autodetaches to produce the $BeO(v = 2)$ product. Using the above values for the EA and vibrational constants of BeO^-, we find that 16359 cm^{-1} excitation from $BeO^-(v = 4)$ will terminate 180 ± 20 cm^{-1} below $BeO(v = 3)$. This energy interval is consistent with the theoretical estimate[44] of 199 cm^{-1} for the binding energy of the electron in the first dipole bound state of BeO^-. Similar intensity anomalies, caused by the excitation of dipole bound states, were reported by Dao and Mabbs[63] in their study of the photodetachment spectrum of AuF^-.

2.5 Conclusion

The $X\ ^2\Sigma^+ \rightarrow X\ ^1\Sigma^+$ electronic transition of BeO^- was studied by means of photoelectron velocity map imaging spectroscopy. The detachment threshold (electron affinity) and vibrational and rotational constants of BeO^- were determined for the first time. A*b initio* electronic structure calculations were in good agreement with the experimental results. The electron detachment characteristics were found to be dependent on the electron kinetic energy. For near threshold detachment, channels involving multiple quanta changes in rotational angular momenta had significant cross sections. These channels diminished as the detachment photon energy was increased, leaving $\Delta N = 0$ as the dominant channel.

2.6 Acknowledgements

We are most grateful to Prof. Arthur Suits (University of Missouri) for providing advice on the optimization of our imaging system, and for the software used to capture and analyze the images. We thank Joseph Czekner (Brown University) for his advice on troubleshooting our spectrometer and improving the quality of the images. We also thank the referee for bringing to our attention the possibility that excited states of BeO^- may be observed via intensity anomalies. This work was supported by the National Science Foundation under grants CHE-1265586 and CHE-1565912.

2.7 References for Chapter 2

1. S. A. Couchman, N. Holzmann, G. Frenking, D. J. D. Wilson, and J. L. Dutton, Dalton Trans. **42,** 11375 (2013).
2. K. J. Iversen, S. A. Couchman, D. J. D. Wilson, and J. L. Dutton, Coord. Chem. Rev. **297-298,** 40 (2015).
3. M. C. Heaven, J. M. Merritt, and V. E. Bondybey, Annu Rev Phys Chem **62,** 375 (2011).
4. M. C. Heaven, V. E. Bondybey, J. M. Merritt, and A. L. Kaledin, Chem. Phys. Lett. **506,** 1 (2011).
5. M. Srnec and R. Zahradnik, Chem. Phys. Lett. **407,** 283 (2005).
6. A. Veldkamp and G. Frenking, Chem. Phys. Lett. **226,** 11 (1994).
7. S. Borocci, N. Bronzolino, and F. Grandinetti, Chem. Phys. Lett. FIELD Full Journal Title:Chemical Physics Letters **406,** 179 (2005).
8. R. Shinde and M. Tayade, J. Phys. Chem. C **118,** 17200 (2014).

9. M. Alipour, Int. J. Quantum Chem. **114,** 255 (2014).

10. L. Ren, L. Cheng, Y. Feng, and X. Wang, J. Chem. Phys. **137,** 014309/1 (2012).

11. Y. Qu and Y. Zhang, Spectrochim. Acta, Part A **67A,** 350 (2007).

12. T. E. Field-Theodore, D. J. D. Wilson, and J. L. Dutton, Inorg. Chem. **54,** 8035 (2015).

13. J. Gebhardt, F. Vines, P. Bleiziffer, W. Hieringer, and A. Goerling, Phys. Chem. Chem. Phys. **16,** 5382 (2014).

14. V. V. Meshkov, A. V. Stolyarov, M. C. Heaven, C. Haugen, and R. J. LeRoy, J. Chem. Phys. **140,** 064315/1 (2014).

15. J. M. Merritt, V. E. Bondybey, and M. C. Heaven, Science (Washington, DC, U. S.) **324,** 1548 (2009).

16. J. W. Mullinax, A. Y. Sokolov, and H. F. Schaefer, J. Chem. Theory Comput. **11,** 2487 (2015).

17. M. Lesiuk, M. Przybytek, M. Musial, B. Jeziorski, and R. Moszynski, Phys. Rev. A At., Mol., Opt. Phys. **91,** 012510/1 (2015).

18. S. Chattopadhyay, R. K. Chaudhuri, and U. Sinha Mahapatra, J. Comput. Chem. **36,** 907 (2015).

19. S. Sharma, T. Yanai, G. H. Booth, C. J. Umrigar, and G. K.-L. Chan, J. Chem. Phys. **140,** 104112/1 (2014).

20. L. M. Mentel and E. J. Baerends, J. Chem. Theory Comput. **10,** 252 (2014).

21. M. El Khatib, G. L. Bendazzoli, S. Evangelisti, W. Helal, T. Leininger, L. Tenti, and C. Angeli, J. Phys. Chem. A **118,** 6664 (2014).

22. X. W. Sheng, X. Y. Kuang, P. Li, and K. T. Tang, Phys. Rev. A At., Mol., Opt. Phys. **88,** 022517/1 (2013).

23. M. J. Deible, M. Kessler, K. E. Gasperich, and K. D. Jordan, J. Chem. Phys. **143,** 084116/1 (2015).

24. K. P. Huber and G. Herzberg, *Molecular spectra and molecular structure, 4: Constants of diatomic molecules* (1979).

25. A. Lagerqvist and R. Westoo, Ark. Mat., Astron. Fys. **A31,** 14 pp (1945).

26. A. Lagerqvist, Nature (London, U. K.) **157,** 547 (1946).

27. A. Lagerqvist, Ark. Fys. **7,** 473 (1954).

28. C. A. Thompson and L. Andrews, J. Am. Chem. Soc. FIELD Full Journal Title:Journal of the American Chemical Society **116,** 423 (1994).

29. Verhaege.G and W. G. Richards, Journal of Chemical Physics **45,** 1828 (1966).

30. W. M. Huo, K. F. Freed, and Klemperer.W, Journal of Chemical Physics **46,** 3556 (1967).

31. H. F. Schaefer, Journal of Chemical Physics **55,** 176 (1971).

32. S. V. Oneil, P. K. Pearson, and H. F. Schaefer, Chemical Physics Letters **10,** 404 (1971).

33. I. Adamovic, M. Parac, M. Hanrath, and M. Peric, Journal of the Serbian Chemical Society **64,** 721 (1999).

34. C. W. Bauschlicher and D. R. Yarkony, Journal of Chemical Physics **72,** 1138 (1980).

35. G. H. F. Diercksen, A. J. Sadlej, and M. Urban, Chemical Physics **158,** 19 (1991).

36. J. Irisawa and S. Iwata, Theoretica Chimica Acta **81,** 223 (1992).

37. T. E. Sorensen and W. B. England, International Journal of Quantum Chemistry **76,** 259 (2000).

38. B. A. Thrush, Proceedings of the Chemical Society of London**,** 339 (1960).

39. W. Koch, J. R. Collins, and G. Frenking, Chem. Phys. Lett. FIELD Full Journal Title:Chemical Physics Letters **132,** 330 (1986).

40. G. Frenking, W. Koch, J. Gauss, and D. Cremer, J. Am. Chem. Soc. FIELD Full Journal Title:Journal of the American Chemical Society **110,** 8007 (1988).

41. G. Frenking, S. Dapprich, K. F. Koehler, W. Koch, and J. R. Collins, Mol. Phys. FIELD Full Journal Title:Molecular Physics **89,** 1245 (1996).

42. T. Takayanagi, H. Motegi, Y. Taketsugu, and T. Taketsugu, Chem. Phys. Lett. FIELD Full Journal Title:Chemical Physics Letters **454,** 1 (2008).

43. H. Motegi, A. Kakizaki, T. Takayanagi, Y. Taketsugu, T. Taketsugu, and M. Shiga, Chem. Phys. **354,** 38 (2008).

44. G. L. Gutsev, M. Nooijen, and R. J. Bartlett, Chem. Phys. Lett. **276,** 13 (1997).

45. K. D. Jordan and R. Seeger, Chem. Phys. Lett. **54,** 320 (1978).

46. D.-Y. Hwang and A. M. Mebel, Chem. Phys. Lett. FIELD Full Journal Title:Chemical Physics Letters **321,** 95 (2000).

47. D. M. Neumark, J. Phys. Chem. A **112,** 13287 (2008).

48. I. Leon, Z. Yang, H.-T. Liu, and L.-S. Wang, Rev. Sci. Instrum. **85,** 083106/1 (2014).

49. A. T. J. B. Eppink and D. H. Parker, Review of Scientific Instruments **68,** 3477 (1997).

50. K. J. Mascaritolo, A. M. Gardner, and M. C. Heaven, J. Chem. Phys. **142,** 114311 (2015).

51. M. A. Duncan, Rev. Sci. Instrum. **83,** 041101/1 (2012).

52. W. C. Wiley and I. H. McLaren, Review of Scientific Instruments **26,** 1150 (1955).

53. C. M. Western, (University of Bristol Research Data Repository, 2014).

54. W. Li, S. D. Chambreau, S. A. Lahankar, and A. G. Suits, Rev. Sci. Instrum. **76,** 063106/1 (2005).

55. B. Dick, Phys. Chem. Chem. Phys. **16,** 570 (2014).

56. C. Blondel, W. Chaibi, C. Delsart, and C. Drag, Journal of Physics B-Atomic Molecular and Optical Physics **39,** 1409 (2006).

57. H. Hotop and W. C. Lineberger, Journal of Physical and Chemical Reference Data **14,** 731 (1985).

58. W. C. Martin, R. Zalubas, and A. Musgrove, Journal of Physical and Chemical Reference Data **19,** 821 (1990).

59. H. J. Werner, P. J. Knowles, G. Knizia, F. R. Manby, and M. Schutz, Wiley Interdisciplinary Reviews-Computational Molecular Science **2,** 242 (2012).

60. A. Halkier, T. Helgaker, P. Jorgensen, W. Klopper, H. Koch, J. Olsen, and A. K. Wilson, Chem. Phys. Lett. **286,** 243 (1998).

61. R. J. LeRoy, (University of Waterloo Chemical Physics Research Report CP-663, 2007).

62. E. P. Wigner, Physical Review **73,** 1002 (1948).

63. D. B. Dao and R. Mabbs, Journal of Chemical Physics **141,** 7 (2014).

Chapter 3

Photoelectron Velocity Map Imaging Spectroscopy of the Beryllium Sulfide Anion, BeS^-

Slow electron velocity map imaging (SEVI) spectroscopy was used to examine the BeS^- anion to neutral ground state transition, $X\ ^2\Sigma^+ \rightarrow X\ ^1\Sigma^+$. Rotational constants, vibrational intervals, and the electron binding energy of BeS^- were determined. Partially resolved rotational contours were seen due to the relatively small moment of inertia of beryllium sulfide. Upon analysis of the rotational contours, it was seen that changes in the molecular rotational angular momenta, ΔN = -1, -2, -3 and -4, facilitated photodetachment at near-threshold photon energies.

SEVI spectra recorded using photon energies near the threshold for Δv = -1 processes exhibited features that were associated with a dipole – bound state (DBS) of BeS^-. Autodetachment spectroscopy was used to probe this state, and rotationally resolved data were obtained for the DBS $^2\Sigma^+$, $v' = 0$ – $X\ ^2\Sigma^+$, $v'' = 0$ transition. Analysis of this structure provided the rotational constants for BeS^- X, $v'' = 0$ and the electron binding energy of the DBS. Electronic structure calculations, performed at the RCCSD(T) and MRCI levels of theory, gave predictions that were in good agreement with the experimental observations.

3.1 Introduction

Diatomic beryllium compounds provide opportunities for investigations of the unusual bonding characteristics of this element.[1-7] We have recently examined the BeO^- anion[4] using the technique of slow electron velocity map imaging (SEVI) spectroscopy.[8,9] Neutral BeO is known to be a strong Lewis acid[10,11] and its electron affinity was found to be 2.1741 ± 0.0019 eV. The additional electron of BeO^- resides in an anti – bonding orbital that is primarily a mixture of Be 2*s* and O 2p_z. Population of this orbital resulted in a slight lengthening of the bond and a decrease in the vibrational frequency. Another point of interest for BeO^- was the observation of an electric dipole – bound electronically excited state. BeO has a relatively large electric dipole moment (6.26 D) that is sufficient to bind an electron via the charge – dipole interaction.[12] The binding energy for the dipole – bound state (DBS) was found to be 180 ± 20 cm^{-1}, validating an earlier theoretical estimate of 199 cm^{-1}.[13]

Comparisons between beryllium oxide and beryllium sulfide (BeS) are of interest as they yield insights regarding periodic trends. Beryllium sulfide is a potentially useful material for optoelectronic and microelectronic applications. The bulk material has a wide band gap (~4.26 eV), making it suitable for the production of blue – green laser diodes.[14,15] Theoretical studies predict that solid BeS may be used for the reversible storage of H_2.[16] Furthermore it is predicted that diatomic BeO[10,17] and BeS[18] can form remarkably robust physical bonds with rare gas atoms. Experimental evidence supporting the latter prediction has been provided by studies of matrix isolated BeO[19] and BeS[18].

There have been several spectroscopic and theoretical studies of BeS.[16,18,20-27] The $X\ ^1\Sigma^+$ ground state has been characterized by means of electronic spectroscopy.[25,28] Electronic structure calculations have been used to predict the properties of the ground and

lower energy excited states.[20-24] Of particular interest for the present study, the calculated electric dipole moment for BeS is about 5 D.[20,23] This dipole moment is large enough that the BeS^- anion is expected to support at least one DBS. To date, there have been no published reports of experimental or theoretical studies of BeS^-. In the present work, we have examined the anion by means of SEVI and autodetachment spectroscopies. These measurements provided the electron affinity of BeS and the vibration – rotation constants for the $X\ ^2\Sigma^+$ ground state of the anion. A DBS, located about 140 cm^{-1} below the electron detachment threshold, was characterized by means of both SEVI and autodetachment techniques. Theoretical calculations for BeS^- were carried out using coupled cluster and multi – reference configuration interaction methods.

3.2 Experimental Setup

A complete description of the instrumentation used for these experiments is provided in reference,[29] and a summary of details specific to BeS has been provided here. Beryllium sulfide anions were formed via pulsed laser ablation[30] of a Be rod in the presence of He (25 psia) seeded with CS_2 (room temperature vapor pressure). Ablation was accomplished using the second harmonic of a Nd:YAG laser (532 nm), operating with a pulse energy of ~8 mJ. The ablation products were supersonically expanded into a differentially pumped vacuum chamber that housed a Wiley-McLaren time-of-flight mass spectrometer (WM – TOFMS).[31] The axis of the mass spectrometer was perpendicular to the direction of the supersonic expansion. Within the mass spectrometer the anions were accelerated into a drift region where they were directed by an Einzel lens and four sets of deflector plates. A fifth set of deflector plates could be used as a mass gate for selection of

the anions of interest.

The anions were directed through the center of a velocity map imaging lens. This three – electrode component was modeled after the design of Eppink and Parker.[32] Photodetachment of BeS^- was induced by the focused beam from a tunable dye laser (both Nd/YAG and excimer pumped dye lasers were used in these measurements). The laser beam was propagated along an axis that was perpendicular to the direction of the anion beam. The photon energies were chosen to be above the detachment threshold of BeS^- with an energy of 0.5 – 1 mJ per pulse, and beam diameter <2 mm. The photodetachment lasers were frequency calibrated using the B – X absorption spectrum of room temperature I_2 vapor, with line positions provided by the PGOPHER software package.[33]

Following photodetachment, the VMI optics focused the electrons onto a set of imaging quality microchannel plates (MCPs) paired with a phosphor screen. A CCD camera recorded the images, which were averaged over several hundred thousand laser pulses using the imaging collection software designed by Li et al.[34] The images were transformed using the MEVELER program.[35] The MCPs were pulsed so that only the detached photoelectrons were detected. Mu – metal shielding surrounding the photodetachment and electron drift regions minimized image distortions due to external electric and magnetic fields. A photomultiplier tube (PMT) was positioned off-axis of the phosphor screen to monitor phosphor screen emission. This detection method allowed for the optimization of the anion and photoelectron signal. The BeS^- velocity map images were calibrated using the known detachment transitions of S^-.[36]

SEVI data were recorded using fixed frequency excitation. Owing to the presence of a DBS of BeS^-, we were also able to record an autodetachment spectrum. For this

measurement the phosphor screen was masked such that only the light from the center of the screen was observed. The total intensity of this signal was recorded as a function of the excitation laser frequency. Autodetachment spectra were also recorded using an annular mask that selectively detected electrons with energies in the range 850 ± 200 cm^{-1}. The rationale for this measurement is explained in the following sections.

3.3 Theoretical Calculations

BeS is a closed – shell ionic species with an experimentally verified X $^1\Sigma^+$ ground state. The unpaired electron of BeS^- resides in an orbital that is primarily of Be 2*s* – S 3p_z antibonding character, giving rise to a X $^2\Sigma^+$ ground state. Electronic structure calculations were performed on both the anion and neutral beryllium sulfide molecules. These calculations were done to assist in the assignment of the spectra, and to evaluate the suitability of the chosen electronic structure methods. For both beryllium and sulfur, the aug – cc – pwCVQZ basis sets were employed. In our studies[4] of BeO/BeO^- we found that it was advantageous to use density functional theory B3LYP wavefunctions as the reference set for the higher order calculations. Hence, the same approach was taken for BeS/BeS^-.

All calculations were performed using the MOLPRO suite of programs.[37] Potential energy curves (PECs) were calculated pointwise. One series of calculations used the partially spin adapted coupled cluster method including single and double excitations and perturbative corrections for triple excitations (RCCSD(T)). The second method employed was a complete active space self-consistent field calculation, followed by multireference configuration interaction (CASSCF+MRCI+Q, denoted as MRCID in the following text)

levels of theory. The Davidson correction[38] was applied in order to partially compensate for the size inconsistency of the MRCI calculations.

All electrons were included in the correlation treatment of the RCCSD(T) calculations. The active space in the CASSCF calculations consisted of the 2*s* and 2*p* orbitals of Be and the 3*s* and 3*p* orbitals of S. The Be 1*s* and S 1*s*, 2*s*, and 2*p* orbitals were constrained to be doubly occupied. Their wavefunctions were optimized in the CASSCF procedure to aid convergence. For both the anion and neutral BeS species, all electrons were included in the correlation treatment of the subsequent MRCI calculation, in an attempt to recover the core – valence correlation energy. The potential energy curves of the RCCSD(T) calculations are shown in Figure 3.1. Overall, the MRCID results were of comparable quality, with the exception that the error for the electron binding energy (eBE) was larger.

The bound ro – vibrational levels of the resulting PECs were calculated using the LEVEL 8.0 program.[39] The lowest vibrational energy levels were least squares fit to the standard Morse energy level expression, yielding effective values for ω_e and $\omega_e x_e$. The predicted molecular constants are listed in Table 3.1, which includes the experimentally determined constants for BeS. Our calculations are in respectable agreement with the latter, indicating that an appropriate level of theory has been applied. As was observed for BeO/BeO^-, the addition of an electron to BeS lengthens the bond and reduces the vibrational frequency. Predictions for the electron affinity were made with the inclusion of the zero point vibrational energies. Franck-Condon factors (FCF's) for the $BeS^- \rightarrow BeS + e^-$ detachment transitions were calculated by LEVEL[39] using the RCCSD(T) potential energy curves. The relevant subset of FCF's is presented in Table 3.2.

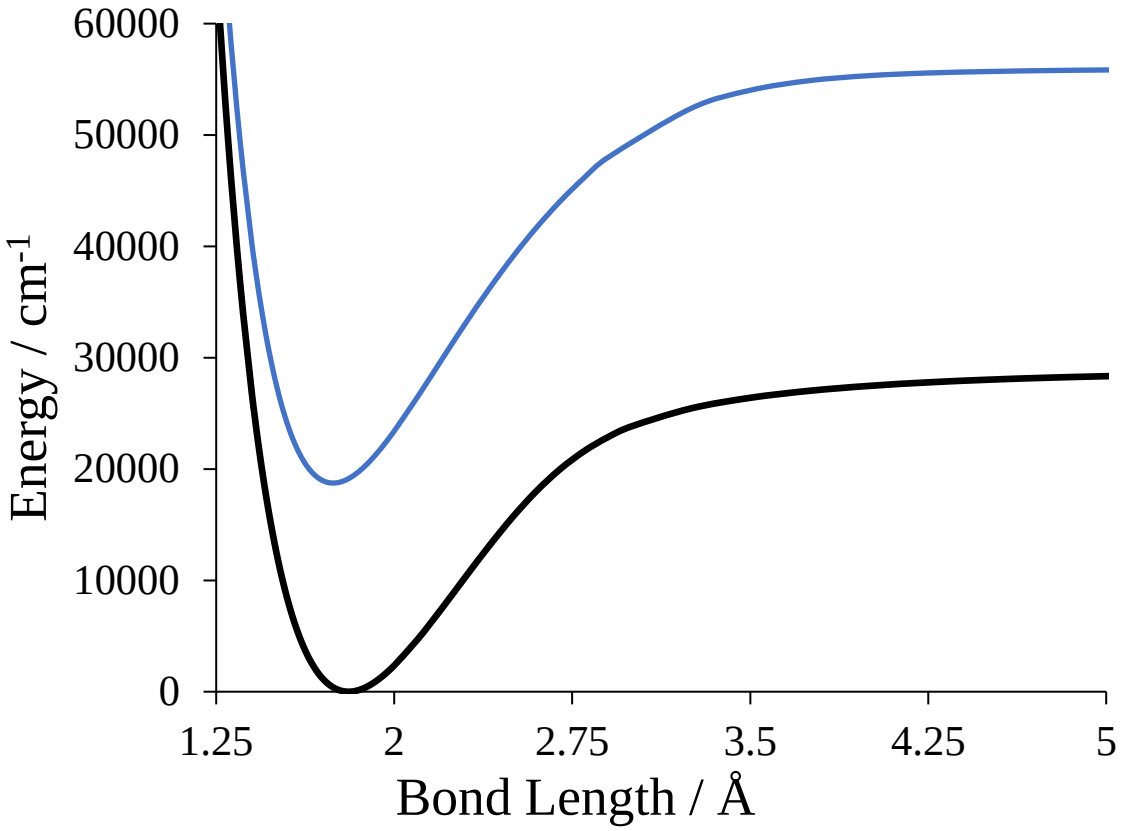

Figure 3.1. Potential energy curves for the BeS^- ground state (black) and BeS ground state (blue). Calculations performed with the CCSD(T) method and the aug – cc – pwVQZ basis set. See text for details.

Table 3.1. Theoretical and experimental spectroscopic parameters for BeS^- and BeS. Values are in units of wavenumbers (cm^{-1}), expect R_e which is in units of Ångstroms.

BeS			
	Exp.[28]	B3LYP-CCSD(T)	MRCI
ω_e	997.94	1000.4	994.5
$\omega_e x_e$	6.137	6.00	6.02
R_e	1.7415	1.7425	1.7465
B_e	0.79059	0.7897	0.7861
α_e	0.00664	0.0066	0.0066

BeS^-			
	Exp.	B3LYP-CCSD(T)	MRCI
eBE	18830 ± 17	18740.5	17863
ω_e	917.31 ± 1.33	906.7	901.6
$\omega_e x_e$	7.73 ± 0.25	5.83	5.30
$\Delta G_{1/2}$	894 ± 8	895.0	891.0
$\Delta G_{3/2}$	878 ± 15	883.4	880.4
$\Delta G_{5/2}$	864 ± 26	871.7	869.8
R_e	1.806± 0.004	1.8077	1.8093
B_e	0.735 ± 0.003	0.733	0.732
α_e	0.0056 ± 0.001	0.0061	0.0065
D_e	1.97×10^{-06}	1.95×10^{-6}	2.0×10^{-6}

Table 3.2: Franck-Condon factors for the BeS^- (X, v'') → BeS (X, v') + e^- photodetachment transition.

v'/v''	0	1	2	3	4	5
0	0.691	0.243	0.054	0.010	0.002	0.000
1	0.267	0.274	0.304	0.117	0.004	0.007
2	0.039	0.375	0.073	0.270	0.164	0.058
3	0.003	0.098	0.384	0.004	0.197	0.186
4	0.000	0.010	0.161	0.337	0.009	0.297

3.4 Results and Discussion

(a) SEVI spectroscopy

Overview SEVI spectra for BeS^-, recorded using detachment photon energies of 18950 and 19262 cm^{-1} are shown in Figure 3.2. The horizontal axis of this figure gives the transition energy, which is defined by the photon energy minus the electron kinetic energy (eKE). The vertical axis is the transformed image intensity, integrated over the angular distribution, and is proportional to electron counts. The images were almost isotopic, yielding anisotropy parameters that were statistically insignificant. Based on the vibrational constants of Table 3.1, the three main features of these spectra are readily assigned. From high to low energy they consist of Δv = 0, -1 and -2 photodetachment events. The resolution of SEVI spectroscopy improves with decreasing eKE. This effect is clearly apparent in Figure 3.2, where the structure of the Δv = 0 feature begins to resolve as the photon energy approaches the detachment threshold. Expanded spectra recorded with near-threshold detachment of the Δv = 0, -1 and -2 features are presented in Figure 3.3. Here it can be seen that there is a red shift of the main peak in trace A (lower energy detachment photon), relative to trace B. This same behavior was observed for the Δv = 0 features of the BeO^- SEVI spectra using comparable above threshold detachment energies.[4] In the latter study this effect was explained by considering the dependence of the photodetachment cross – section on the energy above threshold.

The Wigner threshold law predicts that the cross-section (σ) will be governed by the expression $\sigma \propto eKE^{(l+\frac{1}{2})}$, where l is the angular momentum of the detached electron.[9] When l is greater than 0 the cross – section drops to very low values just above threshold. However, the transfer of rotational energy can augment the energy available to the electron.

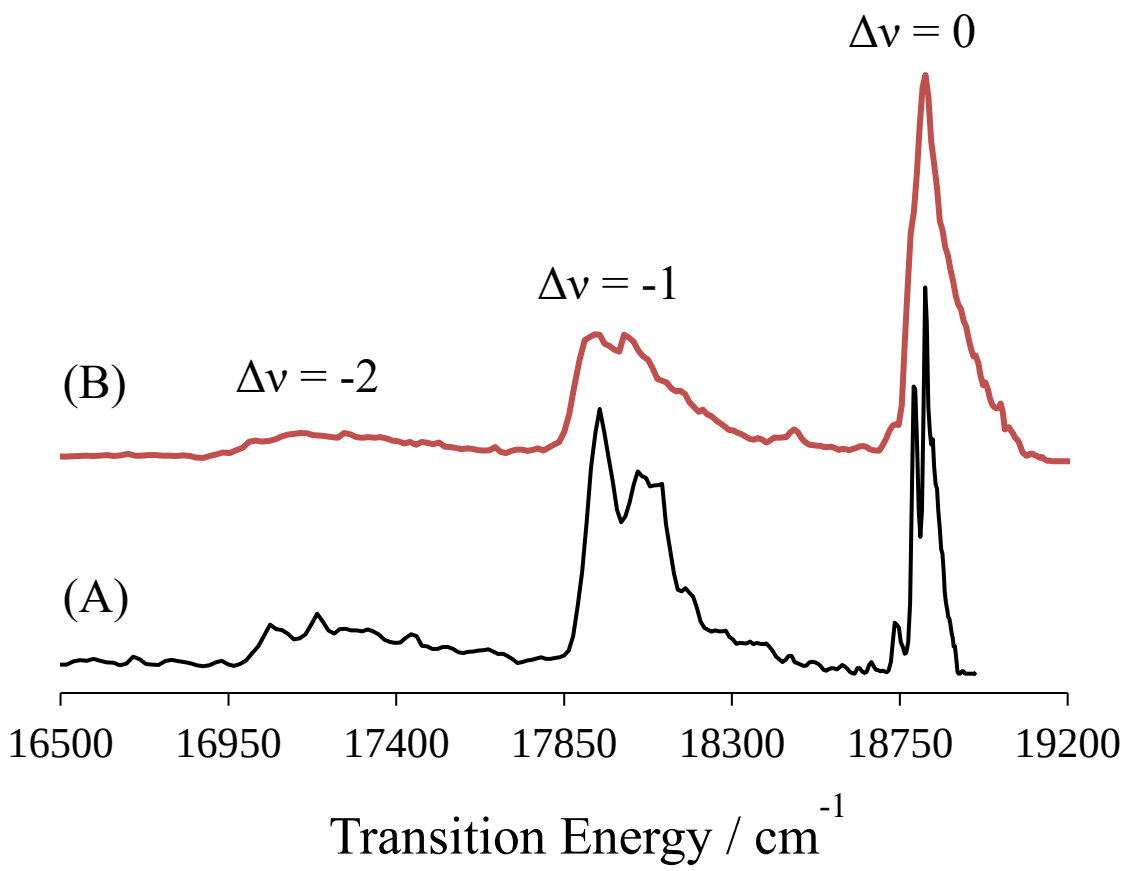

Figure 3.2. SEVI spectra for BeS- recorded using photon energies of 18950 cm^{-1} (trace (A)) and 19262 cm^{-1} (trace (B)). The transition energy is equal to hν – eKE.

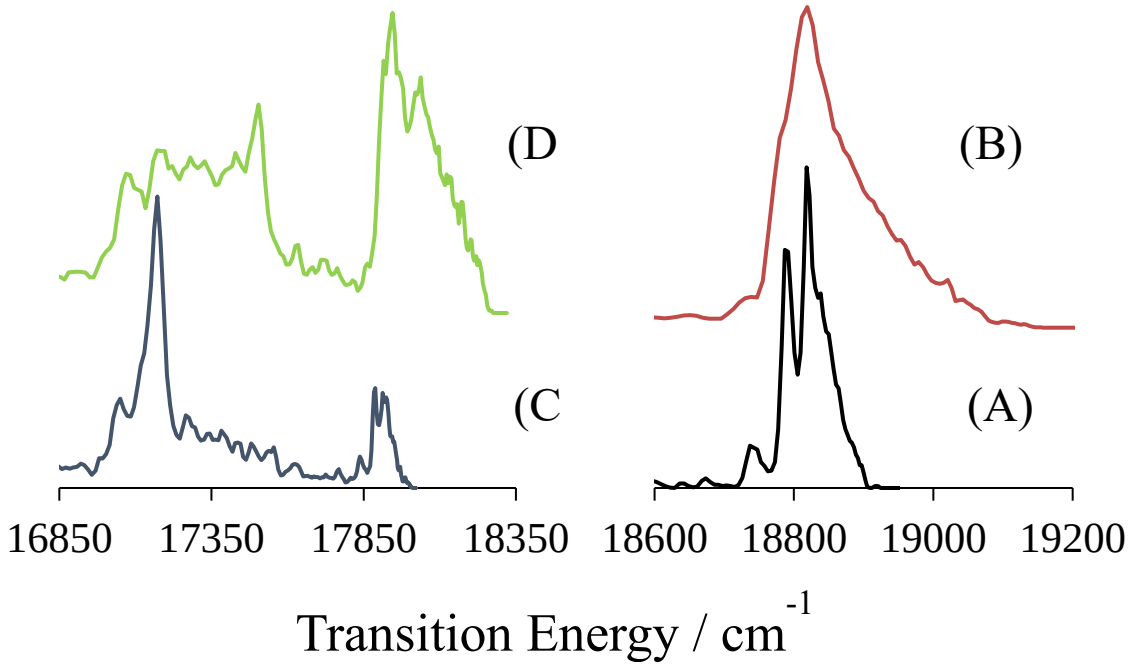

Figure 3.3. SEVI spectra of BeS^- at various photon energies. (A) Black, photon energy = 18949.9 cm^{-1} (B) Red, 19261.5 cm^{-1} (C) Blue, 18020.0 cm^{-1} (D) Green, 18320.1 cm^{-1}. (A) and (B) display $\Delta v = 0$ detachment channels. (C) and (D) display $\Delta v = -1$ and $\Delta v = -2$ detachment channels.

When the photon energy is well above threshold, $\Delta N = 0$ processes dominate (where N is the rotational angular momentum, exclusive of spin). As the photon energy approaches the threshold the $\Delta N < 0$ processes become increasingly more important. As the band heads of the $\Delta N < 0$ rotational branches are below the band origins, their increased contributions result in a red shift of the rotational band contours. A model of the rotational contours that includes this behavior was described in ref.[4] This model was applied to the data for BeS^- and the fit to the $\Delta v = 0$ contour is shown in Figure 3.4. The vibration – rotation constants used for BeS(X) were taken from the literature[28] (Table 3.1). The computed values for the $BeS^-(X)$ molecular constants (Table 3.1, RCCSD(T) results) were used as the starting guess for the simulations. These constants and the electron affinity were systematically refined to obtain the best agreement with the experimental data. Transitions from several vibration levels contributed to the contours, and the data were consistent with a high internal energy content for the anion. Simulations that assumed a Boltzmann distribution for the rotational level populations did not give optimal results. Improved fits were achieved when a two – temperature distribution was assumed, of the form

$$P(N) = (2N + 1)(a_1 Exp(-E(N)/k_B T_1) + a_2 Exp(-E(N)/k_B T_2)) \qquad (3.1)$$

where $E(N)$ is the rotational energy, k_B is the Boltzmann constant, T_1 and T_2 are temperatures and a_1 and a_2 are fractional coefficients. Population distributions of this kind are not uncommon in jet expansions, where cooling of the higher energy rotational states is kinetically limited by the rate of expansion.[40] The simulated contour is compared to the observed spectrum in Figure 3.4. The labels M, N, O, P, Q correspond to the band heads of the ΔN = -4, -3, -2, -1 and 0 rotational branches, respectively. The subscripts provide the upper and lower state vibrational assignments. For this simulation, the rotational

temperatures were set to T_1 = 150 and T_2 = 500 K. The value for l was set to 3. As in our study of BeO^-, we consider this to be simply a model parameter, not indicative of the electronic angular momentum.[4] Another trend that is evident in Figure 3.2 concerns the widths of the Δv = 0, -1 and -2 features. The bands become broader as $|\Delta v|$ increases. Inspection of Table 3.2 shows that this is caused by the distribution of the Franck-Condon factors. The BeS electron affinity and BeS^- molecular constants resulting from fitting to all of the contours (Δv = 0, -1 and -2) are listed in Table 3.1.

In Figure 3.3, traces C and D show SEVI spectra recorded using photon energies (18020 and 18320 cm^{-1}) that were close to the energy of thresholds of the Δv = -1 processes. Each trace has a prominent peak imposed on the Δv = -2 contour, centered at 17172 cm^{-1} in trace C and 17504 cm^{-1} in trace D. Similar peaks were observed for spectra recorded with photon energies within the 17612 – 18320 cm^{-1} range. The peak was systematically shifted from the photon energy by 850 ± 25 cm^{-1}. We assign this feature to a dipole bound state of BeS^- (DBS, v = 1) that lies 136 ± 25 cm^{-1} below the BeS (X, v = 1) + e^- detachment threshold. The almost constant shift between the peak center and the photon energy indicates that the vibrational autodetachment process BeS^- (DBS, v = 1) $\rightarrow$ BeS (X, v = 0) + e^- was dominated by ΔN = 0 events. This process is illustrated in the energy level diagram of Figure 3.5.

(b) Autodetachment spectroscopy

To check the assignment of the DBS features, the autodetachment spectrum was examined. This measurement was initially focused on the BeS^- (DBS, v = 0) level. Rotational constants for the DBSs of anions are very close to those of the neutral molecule. Using the constant B_0 = 0.7873 cm^{-1} for BeS (X, v = 0) and the observation that the DBS

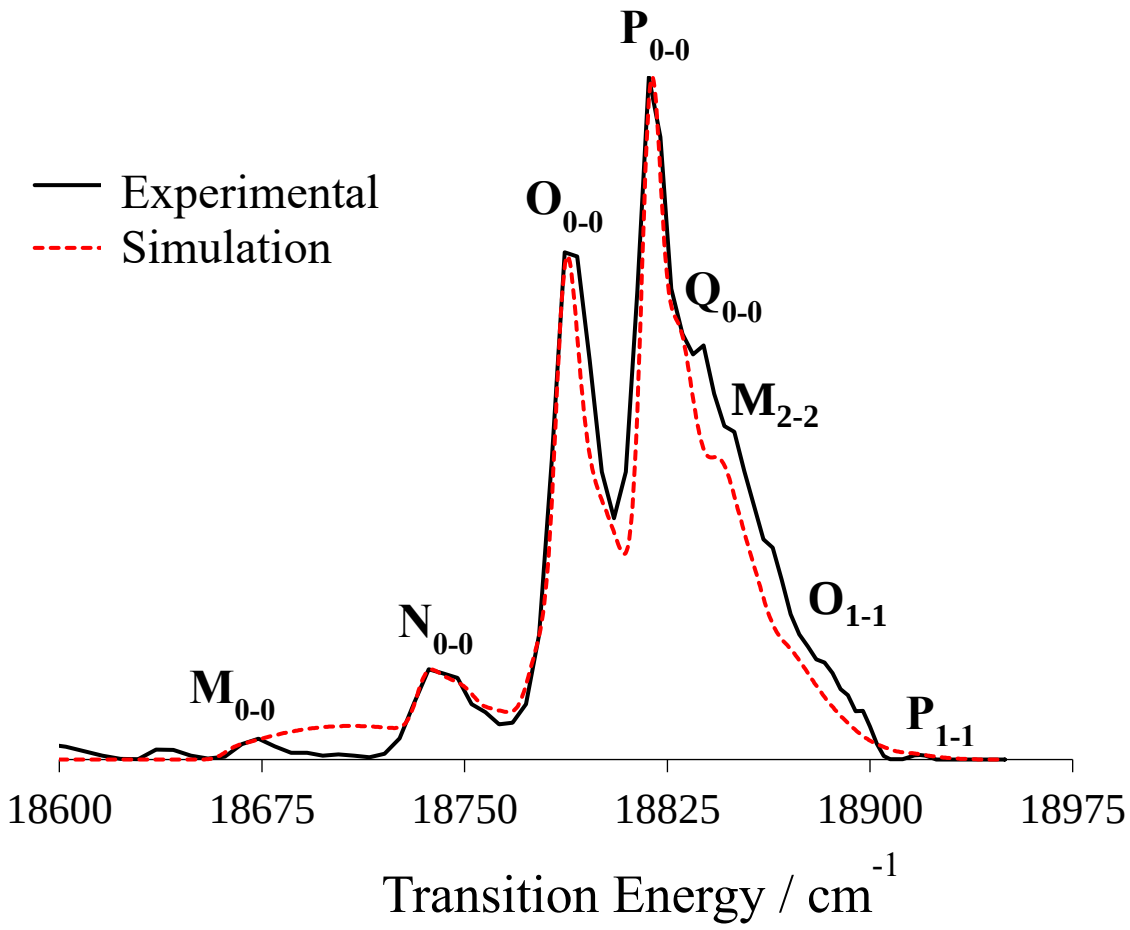

Figure 3.4. SEVI spectrum of the $v = 0$ region of BeS^- and simulation (broken red line). The photon energy was 18949.9 cm^{-1}.

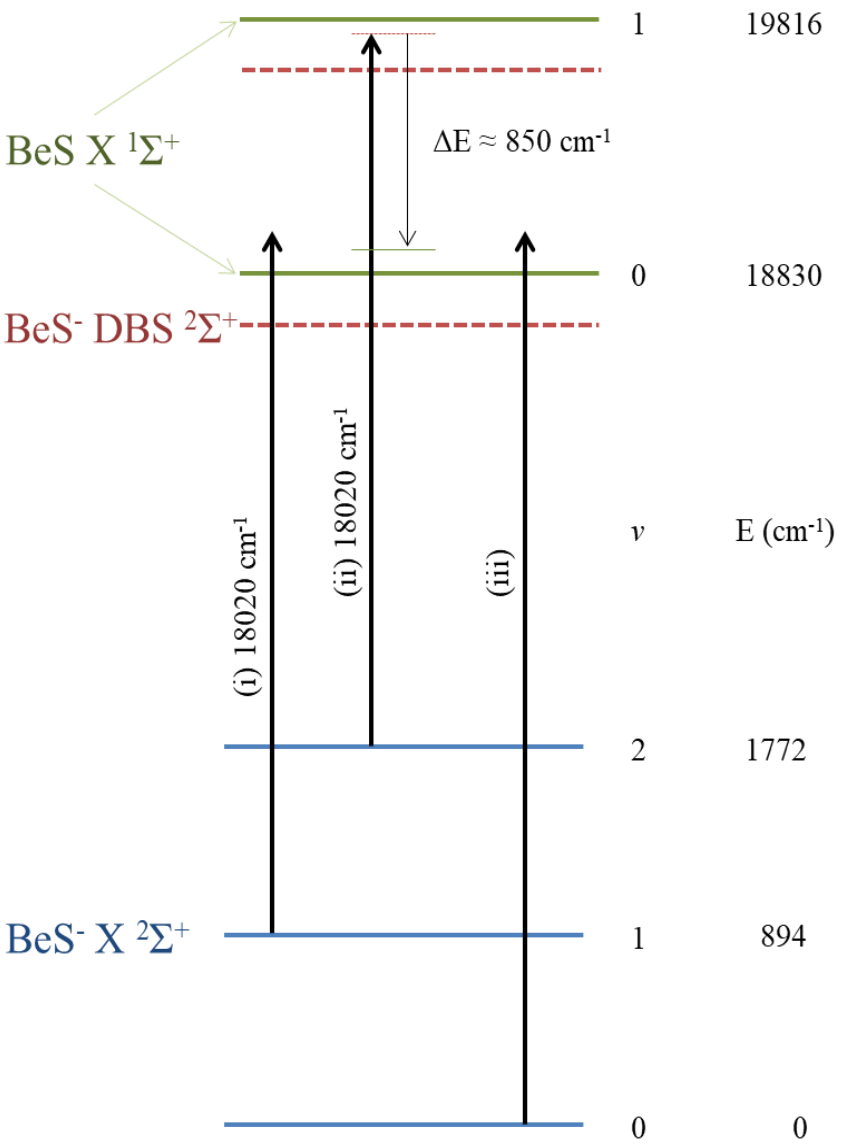

Figure 3.5: Energy level diagram showing BeS^- photodetachment processes. The vertical transitions labeled (i) and (ii) correspond to the features seen at 17910 and 17172 cm^{-1} in Figure 3 C. Transition (i) is direct photodetachment via the 0 – 1 band, while transition (ii) results in excitation of the BeS^- DBS $^2\Sigma^+$, $v = 1$ level. Vibrational autodetachment from this level, with $\Delta N = 0$, produces electrons with a kinetic energy of approximately 850 cm^{-1}. Transition (iii) represents excitation of rotational levels of BeS^- DBS $v = 0$ that have sufficient energy to undergo rotational autodetachment.

was about 140 cm^{-1} below the detachment threshold, it was estimated that levels with $N \geq 14$ would be subject to rotational autoionization. The resulting electrons would have low kinetic energies. To observe these events, the phosphor screen was masked so that only the signal from a central aperture, corresponding to electrons with kinetic energies in the range 0 - 100 cm^{-1}, was registered. This signal was monitored as a function of the excitation laser photon energy. The spectrum obtained is shown in Figure 3.6. The resolution was limited by the laser linewidth, indicating that rotational autodetachment processes were relatively slow. The rotational structure of this band was assigned using upper state combination differences, followed by a fit to the lower state rotational constants and band origin energy by means of the program POPHER.[33] The constants obtained from this fit are listed in Table 3.3. Note that the band shows only P- and R-branches, indicating a DBS $^2\Sigma^+ - X\ ^2\Sigma^+$ transition. Rotational line assignments are indicated for the 0 – 0 band. Lines of the 1 – 1 band are also present, but they have not been labeled to avoid congestion. The origin of the 0 – 0 band is 141 ± 17 cm^{-1} below the detachment threshold, where the uncertainty is defined by our measurement of the latter. This value is consistent with our interpretation of the DBS features of the SEVI spectra, that indicate that the BeS^- (DBS, $v = 1$) level is 145 ± 25 cm^{-1} below BeS (X, $v = 1$) + e^-. Finally, we examined the DBS – X 1 – 0 transition using vibrational autodetachment spectroscopy (BeS^- (DBS, $v = 1$) $\rightarrow$ BeS (X, $v = 0$) + e^-). The electrons produced by this process were expected to be emitted with kinetic energies near 850 cm^{-1}. Consequently, an annular mask was placed on the phosphor screen to limit the detection to electrons with energies within the range of 850 ± 200 cm^{-1}. The autodetachment spectrum resulting from this measurement is shown in Figure 3.7. The intensity contour of this band reflects the same rotational structure as that of Figure 3.6,

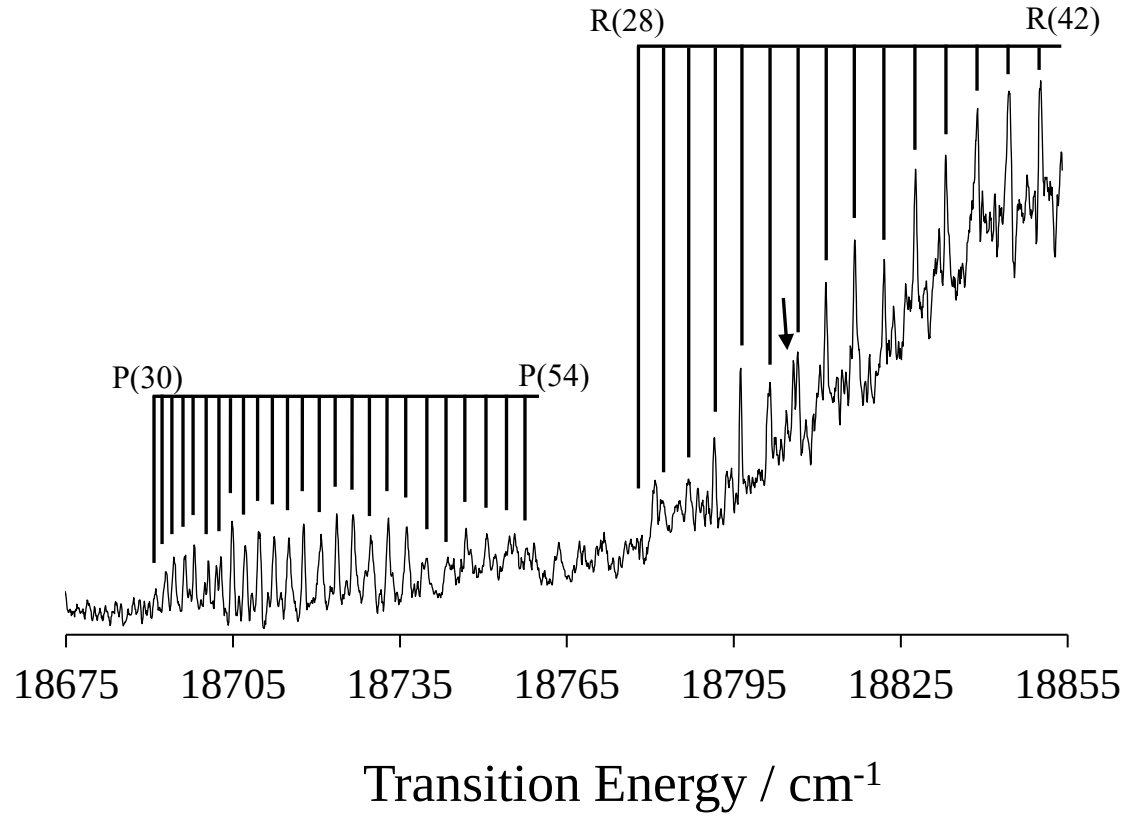

Figure 3.6. DBS $^2\Sigma^+$, $v' = 0$ – X $^2\Sigma^+$, $v'' = 0$ BeS^- autodetachment spectrum. Arrow denotes P(65).

Table 3.3: BeS^- molecular constants (cm^{-1}) derived from the DBS $^2\Sigma^+$, $v' = 0 \leftarrow$ X $^2\Sigma^+$, $v'' = 0$ transition.

State	T_0	B_0	D_0
X $^2\Sigma^+$	0.0	0.731(1)	1.5(4) x 10^{-6}
DBS $^2\Sigma^+$	18689.0(1)	0.7873 [a]	2.0 x 10^{-6} [a]

a. Fixed at the values for BeS X $^1\Sigma^+$, $v = 0$ taken from reference[28]

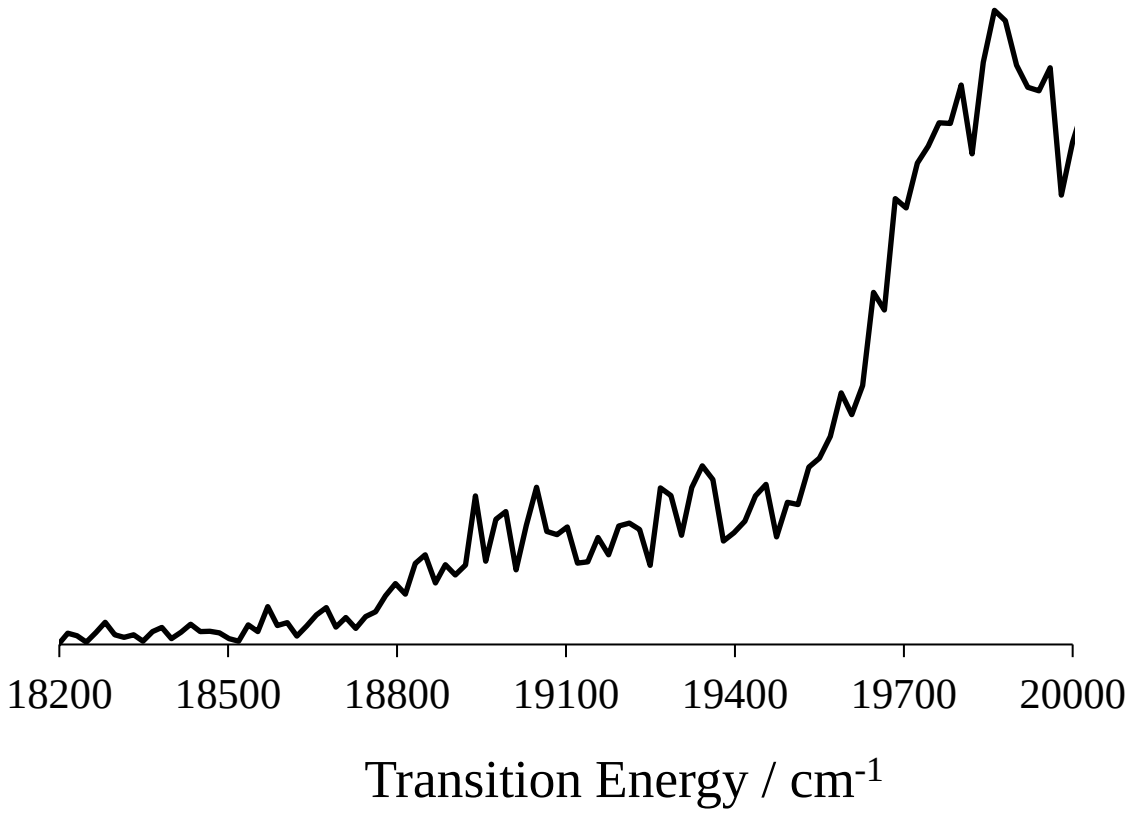

Figure 3.7. DBS $^2\Sigma^+$, $v' = 1$ – X $^2\Sigma^+$, $v'' = 0$ BeS^- autodetachment spectrum.

but the resolution was not high enough to reveal individual rotational lines.

3.5 Conclusions

The electron affinity of BeS (2.248(2) eV) has been determined for the first time. This value is higher than the EA of BeO (2.174(2) eV), which probably reflects the greater EA of S. SEVI and autodetachment spectroscopy techniques were used to characterize the vibration – rotation constants of BeS^- ($X\ ^2\Sigma^+$). It was found that the bond length of BeS^- was greater than that of BeS, while the vibrational frequency was diminished. These changes were consistent with the outermost electron of BeS^- residing in the Be 2*s* / S 3p_z anti-bonding orbital. High-level electronic structure calculations supported this interpretation, yielding predictions that were in good agreement with the EA of BeS and the molecular constants of BeS^-.

A dipole bound state of BeS^- was observed 141 ± 17 cm^{-1} below the electron detachment threshold. The electron binding energy for this state is comparable to those of the first DBS's of BeO^- (180(20) cm^{-1}) and AlO^- (52(6) cm^{-1}). In this series the binding energies correlate with the electric dipole moments of the neutral molecules.

3.6 Acknowledgements

This material is based upon work supported by the National Science Foundation under CHE - 1565912.

3.7 References for Chapter 3

1. S. A. Couchman, N. Holzmann, G. Frenking, D. J. D. Wilson, and J. L. Dutton, Dalton Trans. **42,** 11375 (2013).
2. K. J. Iversen, S. A. Couchman, D. J. D. Wilson, and J. L. Dutton, Coord. Chem. Rev. **297-298,** 40 (2015).
3. B. J. Barker, I. O. Antonov, J. M. Merritt, V. E. Bondybey, M. C. Heaven, and R. Dawes, J. Chem. Phys. **137,** 214313/1 (2012).
4. K. J. Mascaritolo, A. R. Dermer, M. L. Green, A. M. Gardner, and M. C. Heaven, J. Chem. Phys. **146,** 054301/1 (2017).
5. M. C. Heaven, J. M. Merritt, and V. E. Bondybey, Annu Rev Phys Chem **62,** 375 (2011).
6. M. C. Heaven, V. E. Bondybey, J. M. Merritt, and A. L. Kaledin, Chem. Phys. Lett. **506,** 1 (2011).
7. J. L. Dutton and G. Frenking, Angew. Chem., Int. Ed. **55,** 13380 (2016).
8. D. M. Neumark, Journal of Chemical Physics **125,** 132303/1 (2006).
9. D. M. Neumark, J. Phys. Chem. A **112,** 13287 (2008).
10. A. Veldkamp and G. Frenking, Chem. Phys. Lett. **226,** 11 (1994).
11. G. Frenking, S. Dapprich, K. F. Koehler, W. Koch, and J. R. Collins, Mol. Phys. FIELD Full Journal Title:Molecular Physics **89,** 1245 (1996).
12. K. D. Jordan, Acc. Chem. Res. **12,** 36 (1979).
13. G. L. Gutsev, M. Nooijen, and R. J. Bartlett, Chem. Phys. Lett. **276,** 13 (1997).
14. N. Benosman, N. Amrane, S. Mecabih, and H. Aourag, Physica B (Amsterdam, Neth.) **304,** 214 (2001).

15. D. Heciri, L. Beldi, S. Drablia, H. Meradji, N. E. Derradji, H. Belkhir, and B. Bouhafs, Comput. Mater. Sci. **38,** 609 (2007).

16. D.-Y. Hwang and A. M. Mebel, J. Am. Chem. Soc. **122,** 11406 (2000).

17. T. Takayanagi, H. Motegi, Y. Taketsugu, and T. Taketsugu, Chem. Phys. Lett. FIELD Full Journal Title:Chemical Physics Letters **454,** 1 (2008).

18. Q. Wang and X. Wang, J. Phys. Chem. A **117,** 1508 (2013).

19. C. A. Thompson and L. Andrews, J. Am. Chem. Soc. FIELD Full Journal Title:Journal of the American Chemical Society **116,** 423 (1994).

20. A. G. S. De Oliveira-Filho, T. V. Alves, V. W. Ribas, L. F. A. Ferrao, O. Roberto-Neto, F. B. C. Machado, and F. R. Ornellas, Int. J. Quantum Chem. **111,** 1694 (2011).

21. T. Larbi, F. Khadri, H. Ghalila, S. Lahmar, and M. Hochlaf, Chem. Phys. **373,** 193 (2010).

22. H. Liu, W. Xing, D.-h. Shi, and J.-f. Sun, Yuanzi Yu Fenzi Wuli Xuebao **29,** 216 (2012).

23. J. Noga and T. Pluta, Chem. Phys. Lett. **264,** 101 (1997).

24. H. Partridge, S. R. Langhoff, and C. W. Bauschlicher, Jr., J. Chem. Phys. **88,** 6431 (1988).

25. B. Pouilly, J. M. Robbe, J. Schamps, R. W. Field, and L. Young, J. Mol. Spectrosc. **96,** 1 (1982).

26. D. P. Rai, M. P. Ghimire, and R. K. Thapa, Semiconductors **48,** 1411 (2014).

27. M. Srnec and R. Zahradnik, Chem. Phys. Lett. **407,** 283 (2005).

28. C. J. Cheetham, W. J. M. Gissane, and R. F. Barrow, Trans. Faraday Soc. **61,** 1308 (1965).

29. A. R. D. K. J. Mascaritolo, M. L. Green, A. M. Gardner, M. C. Heaven, J. Chem. Phys. **146** (2017).

30. M. A. Duncan, Rev. Sci. Instrum. **83,** 19 (2012).

31. W. C. Wiley and I. H. McLaren, Rev. Sci. Instrum. **26,** 1150 (1955).

32. A. T. J. B. Eppink and D. H. Parker, Rev. Sci. Instrum. **68,** 3477 (1997).

33. C. M. Western**,** University of Bristol Research Data Repository (2014).

34. W. Li, S. D. Chambreau, S. A. Lahankar, and A. G. Suits, Rev. Sci. Instrum. **76,** 063106/1 (2005).

35. B. Dick, Phys. Chem. Chem. Phys. **16,** 570 (2014).

36. C. Blondel, W. Chaibi, C. Delsart, and C. Drag, Journal of Physics B-Atomic Molecular and Optical Physics **39,** 1409 (2006).

37. H. J. Werner, P. J. Knowles, G. Knizia, F. R. Manby, and M. Schutz, Wiley Interdisciplinary Reviews-Computational Molecular Science **2,** 242 (2012).

38. E. R. Davidson and D. W. Silver, Chem. Phys. Lett. **52,** 403 (1977).

39. R. J. LeRoy, (University of Waterloo Chemical Physics Research Report CP-663, 2007).

40. M. Heaven, T. A. Miller, and V. E. Bondybey, Chemical Physics Letters **84,** 1 (1981).

Chapter 4

Principles of Quadrupole Fields and Ion Trapping: Implementation of a Quadrupole Ion Trap into the Spectrometer for Molecular Cooling

Anions that were obtained from the laser ablation source were rotationally hot, making it difficult to obtain high-resolution rotational structure. This phenomenon was seen for both BeO^- and BeS^-. BeO_2^- and BeS_2^- were also seen in the spectrometer during those studies. However, any spectra obtained for these species were broad and congested. It was clear that the spectrometer needed a method for cooling the anions prior to supersonic measurements. Thus, it was decided to implement a quadrupole ion trap (QIT) for molecular cooling into our system. This system required two new chambers to replace the original source chamber, special shielding for components held at low temperatures, mounting of the QIT, and mounting of a quadrupole mass filter (QMF) for mass-selecting anions before entering the QIT. In this chapter, a review of the operating principles of the QMF and QIT is discussed, as well as the design of the necessary components to equip the photoelectron velocity map imaging spectrometer with the ability to rotationally cool ions.

4.1 Operating Principles of the Quadrupole Mass Filter

A QMF will be added to the spectrometer to mass-select and guide ions into the QIT. The QMF will also prevent overloading the QIT with unnecessary charged species.

Detailed reviews on QMFs have been published[1-3] and therefore only a summary of the operating principles will be described herein.

A perfect quadrupole field is created when a potential is applied to four symmetric, hyperbolically-shaped electrodes. Perfect fields can be difficult to achieve and are not always necessary. Consequently, electrodes with a circular cross-section are often used in QMFs to create fields that are very-near quadrupolar. A standard QMF consists of four parallel rod electrodes placed so that the cross-section of the rods is a perfect circle, as shown in Figure 4.1.[1] The rods that lie opposite of each other are connected and form a pair, and each pair is designated (+) or (-). The potential distribution applied to each pair of rods is a combination of DC voltage (time-independent) and AC voltage (radio-frequency (RF) waveform, time-dependent). Ionized particles move through a QMF based on the equation of motion used to describe the potential distribution inside the QMF. This equation describes the potential distribution (Φ) and is based on both the shape of the electrodes and the time-dependency of the applied voltage (Equation 4.1[1]), where U represents the magnitude of the DC voltage, V is the magnitude of the RF waveform, ω is the angular frequency ($2\pi f$) of the RF waveform, t is time, x and y are distances along the coordinate axes inside the quadrupole field, and r_o is the distance from the center axis (z axis) to the surface of any electrode.

$$\Phi = [U + VCos(\omega t)]\frac{x^2 - y^2}{2r_0^2} \tag{4.1}$$

A quadrupole field is ideally described by the solutions to the second-order Mathieu equations. For mathematical details on solving the equation of motion using the Mathieu relations and how these relate to the stability of the ions in the field, refer to references [1-3] and [11].

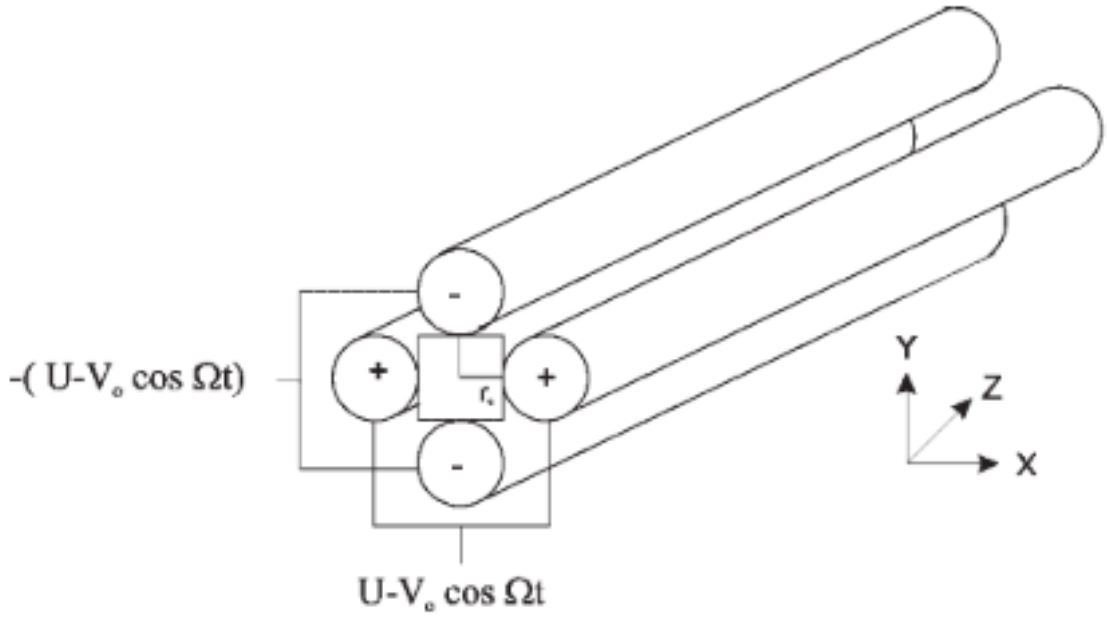

Figure 4.1. Shape, orientation, and connection of the four electrodes in a quadrupole mass filter.

When a positive potential is applied to the electrodes, cations are focused toward the center axis. Positively-charged ions are defocused away from this axis when the potential applied is negative. Due to the time-dependent nature and oscillations of the RF waveform (from positive to negative voltages), the ions follow a wavelike path through the quadrupole field. The voltages are sinusoidally operated. Whether an ion will be eliminated from the molecular beam by striking an electrode as it travels is based on the time it takes the ion to reach an electrode. This process is based on several factors, including the magnitude of the potential being applied, the frequency of the RF waveform, and the mass-to-charge ratio (*m/z*), position, and velocity of the ion.

The ability of the QMF to mass-select charged species comes from the combination of the time-independent, positive DC potential with the AC (RF) potential. Suppose a positive DC potential is applied to electrodes located on the $x - z$ plane, while the RF waveform is set to a high frequency. When a lightweight ion enters the quadrupole field, it will be greatly impacted by the rapidly changing RF potential. When the AC voltage is negative, the acceleration of a cation as it defocuses may be large enough that the lightweight ion will collide with an electrode, causing it to be discharged from the molecular beam. However, a heavy, positively-charged molecule will not be sufficiently affected by the rapidly varying RF potential. Instead, it will be focused onto the center axis via the positive DC voltage. The periods of time when the DC voltage is negative will have a negligible effect on the path of the molecule, and the ion will travel along the center axis and exit the QMF. It is the combination of the DC and AC potentials and the frequency of the RF waveform, along with the structure of the electrodes, that creates a field that is ideal for a specific critical *m/z* value. Ions with a lower *m/z* will collide with the electrodes, and

those above the critical value within a certain range will be transmitted through the device. In this way, a high-pass mass filter is created along the $x - z$ plane.

The electrodes in the $y - z$ plane always maintain a potential that is opposite in sign but equal in magnitude to those along the x axis, so that the AC potential applied to the x electrodes will remain 180^{o} out of phase with the RF waveform on the y axis. Also, the DC potential bias along the y axis will always be opposite of those that lie on the x axis. Since the heavier ions are influenced by the DC potential, the negative voltage on the electrodes in the $y - z$ plane will defocus positively-charged heavy molecules. This defocusing can eliminate them from the molecular beam if their acceleration towards the electrodes along the y axis is greater than pull towards the center axis from the positive voltage of the electrodes on the x axis. For the lighter ions, the relative magnitude between the DC and RF potentials affects its path through the QMF. When the positive alternating AC potential has a magnitude larger than that of the static negative field, the lighter cations are focused towards the center axis and avoid interaction with the surface of the electrodes. Thus, the trajectory of the lightweight ions in the instrument are dependent upon the interaction between the fields in the $x - z$ and $y - z$ planes. Lightweight ions have a trajectory such that they exit the QMF towards the detector, while heavier ions are ejected from the molecular beam. Therefore, a low-pass mass filter is created in the $y - z$ plane of the QMF.

The combination of the high-pass and low-pass mass filters create a bandpass mass filter inside the QMF. The ions must maintain a stable trajectory throughout the QMF to exit towards the detector. For this to occur, a species must be light enough that it is not eliminated by the low pass filter in $y - z$ place but heavy enough so it will not be eliminated by the high pass filter created in the $x - z$ plane. The mass resolution of the QMF is

determined by the width of the bandpass filter, which is set according to the ratio of the AC and DC potentials that are applied on the electrodes. The equation of motion is used to determine the magnitude and frequency of the potentials needed to allow an ion within a specific *m/z* range to be transmitted through the QMF. The diagrams shown in Figure 4.2[1] demonstrate how the combined effects of the low- and high-pass filters form a bandpass filter, thus providing the QMF with the ability to allow only specific *m/z* ratios to maintain a stable trajectory throughout the length of the instrument.

4.2 Operating Principles of the Quadrupole Ion Trap

The fundamental operating principles of the QIT (also called the Paul trap[4,5]) are similar to those of the QMF. The major differences are the structure of the electrodes, allowing for the trapping and storage of ions, and the application of the DC and AC potentials. As before, several reviews of QITs have been published[2-11] and therefore only a brief outline will be discussed here.

A non-linear QIT consists of three electrodes, as shown in Figure 4.3a[2]. The end-cap electrodes are identical and of hyperboloidal geometry, resembling inverted saucers. Each has a hole on the center axis for the transmission of ions. The center electrode is externally shaped as a ring and is designed to have an internal hyperboloidal surface. This electrode is symmetrically spaced between the two end-cap electrodes, and together the electrodes have cylindrical symmetry. A cut-out and diagram of the QIT is shown in Figure 4.3b and 4.3c.

The potential (Φ) distribution inside the QIT can be described by Equation 4.2, and

$$\Phi = \Phi_{ring} - \Phi_{end-capts} \tag{4.2}$$

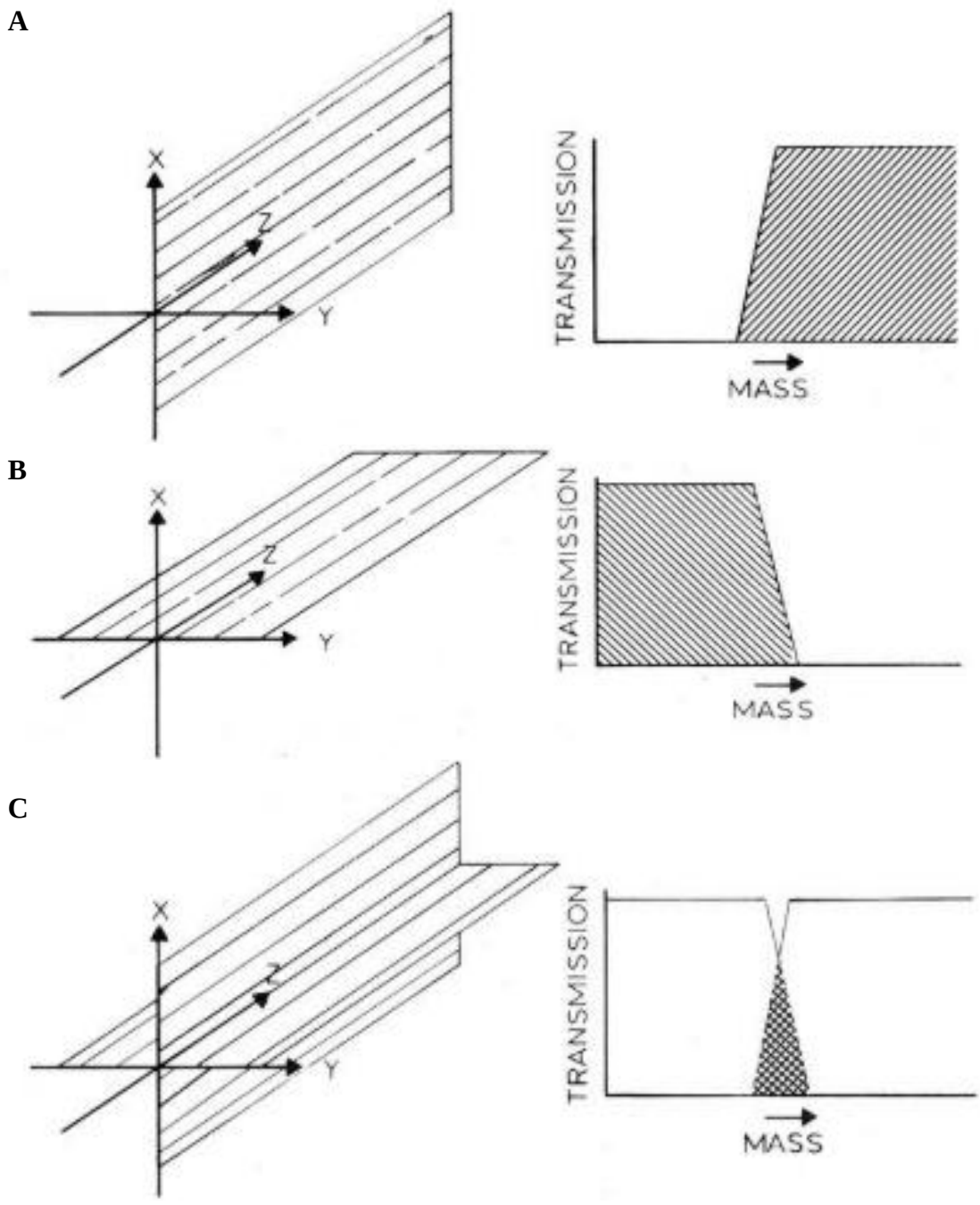

Figure 4.2. A) The *x* – *z* plane of the quadrupole mass filter behaves as a high pass mass filter. B) The *y* – *z* plane behaves as a low pass mass filter. C) Together, the overlapping fields create a bandpass filter, allowing a specific range of masses to be transmitted through the device.

A

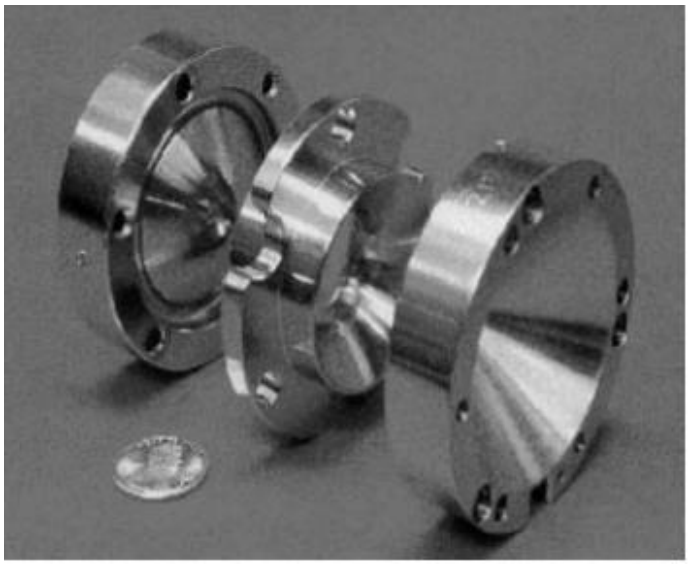

B

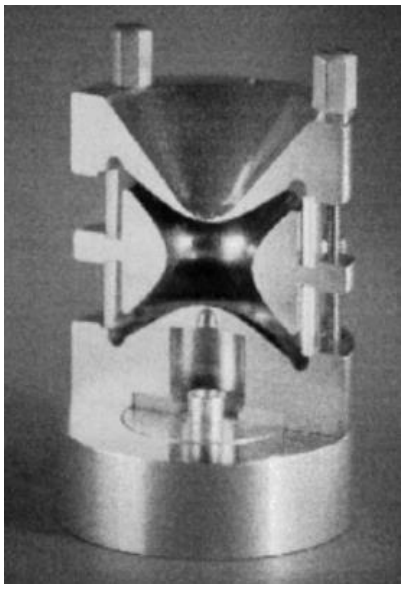

C

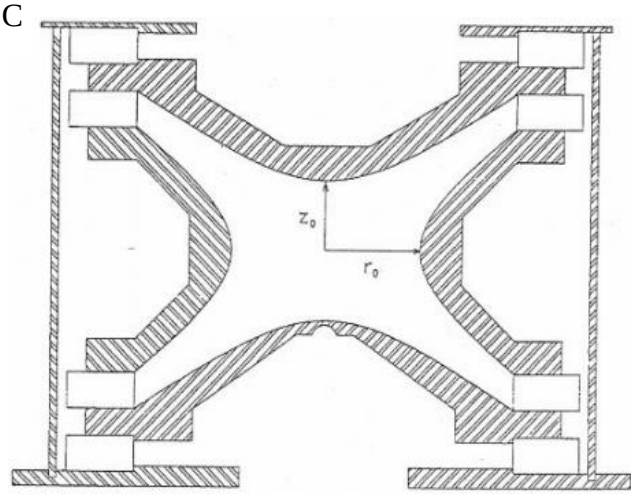

Figure 4.3. A quadrupole ion trap. A) Three metal electrodes, two end-caps and a center ring. B) Cross-section view of a quadrupole ion trap. Voltage is applied using wires wrapped around mounting screws on the outer surface of the electrodes (to be shown later). C) Diagram of the electrodes, where r_o represents the radius of the ring electrode along the horizontal plane and $2z_o$ is the distance between the two end-caps. Typically, r_o = 1 cm.

mathematical analysis of the above equation produces a more complex method of evaluating the potential inside of the QIT. This calculation is represented by Equation 4.3, where U, V, r_o, z_o, and ω represent the same quantities as before.

$$\Phi_{r,z} = \frac{(U+Vcos\omega t)(r^2-2z^2)}{(r_0^2-2z_0^2)} + \frac{2(U+Vcos\omega t)z_0^2}{(r_0^2-2z_0^2)} \quad (4.3)$$

From these mathematical descriptions, it has been shown for the electrode structure to create an ideal quadrupolar potential distribution, the relationship $r_o^2 \approx 2z_o^2$ is required. For a more detailed quantitative description of the equations of motion and stability of the QIT, please refer to references [2], [3], and [11].

The storage capabilities of the QIT trap function in much the same way as the QMF, as Equation 4.3 is a derivative of Equation 4.1. Mathematically, the motions of the ions within the QIT are described as having slow (secular) oscillations, where the fundamental frequencies ω_r and ω_z must be related such that $\omega_r = 2\omega_z$ to stabilize their trajectories inside the trap. It is the magnitude of the potential and the frequency of the RF waveform that gives the QIT its ability to trap ions of a specific *m/z* value. No DC voltage is required to store the charged species, as the sinusoidal operation of the AC voltage directs the ions along in a stable path. The potential well created by the oscillating AC voltage that is responsible for storing ions can be qualitatively described using the "saddle" analogy. Figure 4.4[11] provides an example of the saddle shape using equipotential lines. If a steel ball is placed on one side of the saddle, the ball will roll downwards and its position will be unstable. To prevent the ball from rolling off the saddle, the saddle is rotated. This rotation is maintained at a frequency that holds the ball in a dynamically stable position in the center of the saddle. The overall rotation pattern of the saddle is parabolic. When determining the frequency at which to rotate the saddle, the mass of the ball and the

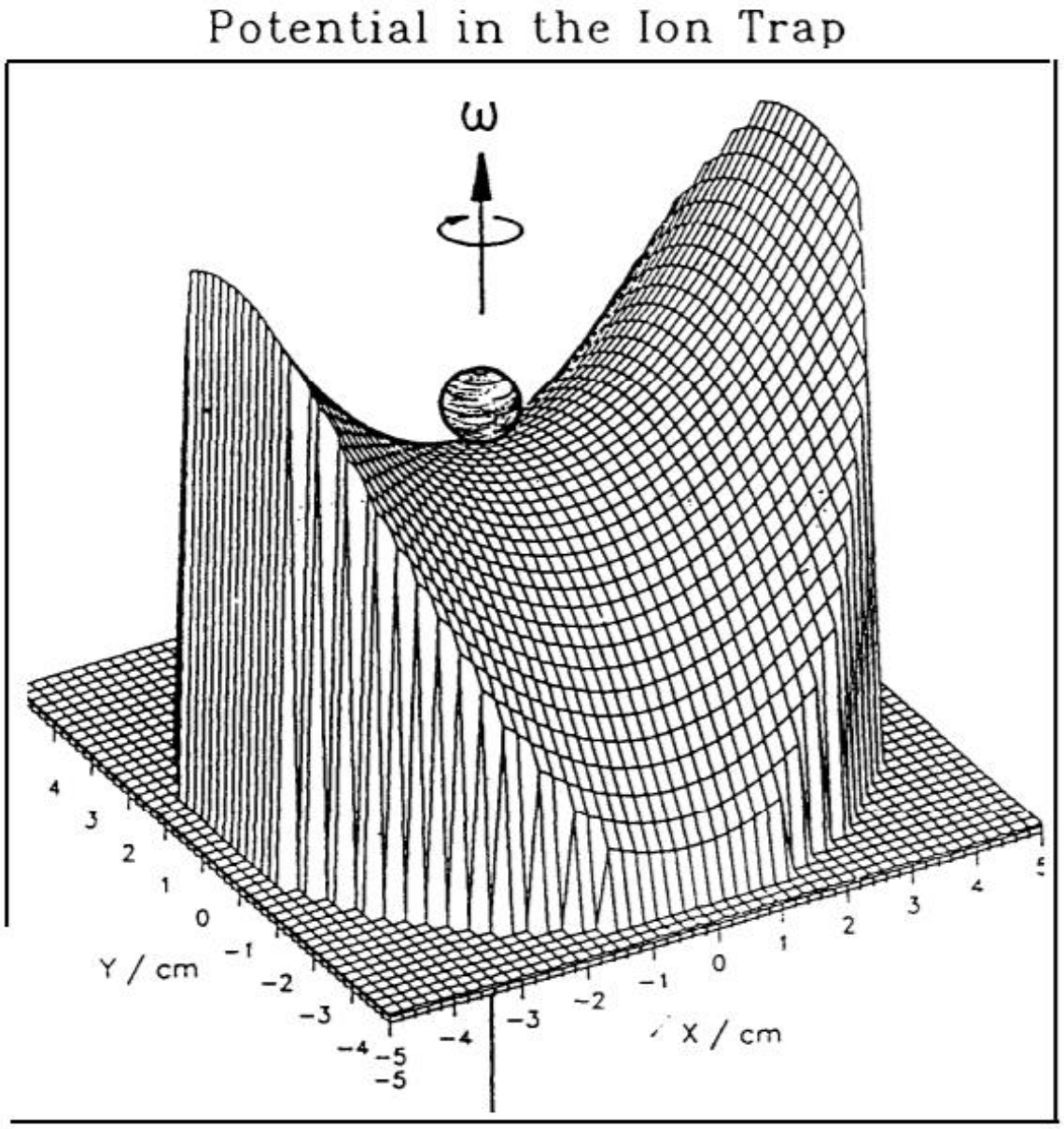

Figure 4.4. Equipotential lines depicting the “saddle”-like shape that is created by the potentials within the quadrupole ion trap.

magnitude of rotation must also be considered. Through this method, multiple balls of similar mass will be held in the center of the saddle.

In other words, the ions harmonically oscillate in the *r* (radial) and *z* (axial) directions and move as if they are trapped inside of an undulating pseudo potential well with quadratic coordinates. The well is formed by the RF waveform, and the depth of the well is directly related to the amplitude of the driving voltage and the frequency of the oscillating potentials in the *r* and *z* directions. The path of the ions inside the trap is that of a Lissajous curve composed of two different fundamental frequency components, one in the *r* and *z* directions, demonstrated in Figure 4.5.[3] In this way, the potential well prevents the ions from travelling farther than ~3 mm from the center of the ion trap.

Once trapped inside of the pseudopotential well, the ions can be stored for microseconds to a few seconds. To decrease the overall internal energy of the ions, a cold buffer gas may be introduced into the trap. For example, collisions with cold He buffer gas induces heat transfer from the trapped ions to the He, effectively cooling the ions. Ion kinetic energies may be reduced to as little as ~0.1 eV. Collisional cooling also increases the sensitivity and resolution of the QIT by decreasing ion kinetic energies and shifting their trajectories towards the center of the trap. The QIT may also be physically connected to a closed-cycle liquid helium refrigeration system through a heat-conducting material, cooling the trap itself to as low as a few Kelvin, depending on the refrigeration system.

When the ions have been sufficiently cooled they are ejected out of the QIT. Ejection occurs when a DC voltage is applied to the end-cap electrodes, effectively pushing/pulling them out of the potential well. Often, the voltage is applied as an uneven

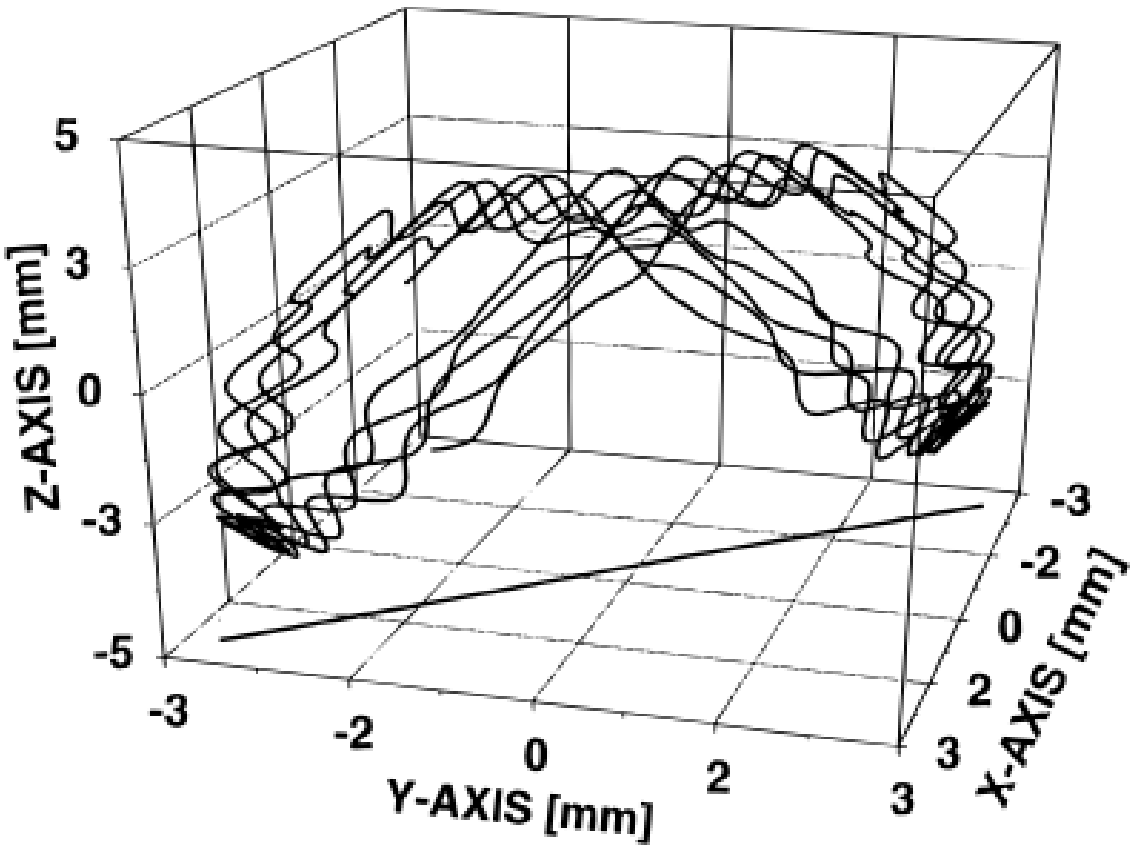

Figure 4.5. Lissajous curve trajectory of the ions trapped inside of a quadrupole ion trap.

gradient across the two end-caps in such a way that the ions are pushed towards the exit end-cap electrode. The magnitude of the gradient must be large enough that the ions can overcome the pseudopotential well created in the trap. The voltage gradient must also be applied for enough time to ensure all the ions exit the QIT. This extraction method is called mixed extraction because it applies a mix of voltages to both end-caps.[10] Other types of extraction methods include attractive extraction and repulsive extraction.[10] For attractive extraction of cations, the entrance end-cap is held at ground while a negative DC voltage is applied to the exit end-cap. This method pulls the ions out of the quadrupole field. The opposite is true for the repulsive extraction mode, where a positive voltage is applied to the entrance end-cap while the exit end-cap is held at ground, pushing the cations out of the field. It has been shown that the attractive and mixed modes of extraction are more efficient than the repulsive mode, and heavier masses are extracted more succinctly than lower masses when the applied voltages are low.[10]

4.3 Designing the Quadrupole Ion Trap System

The QIT, along with its power supply and high voltage pulsing unit, were purchased from Jordan TOF Products, Inc. (C-1251 Quadrupole Ion Trap with 4-hole pattern; D-1203 Ion Trap Power Supply, and D-1040 High-Voltage Pulser). Also purchased were ceramic sleeves that mount between each electrode, serving to contain the buffer gas inside of the QIT. The QIT requires roughly 125 μs for ion extraction and returning to the RF potential, and the duty cycle approaches 100% when the time for storing the ions is above 10 ms. A schematic of the QIT can be found in Figures 4.6 and 4.7.[12]

The shielding of the QIT was designed such that it could be mounted to the second

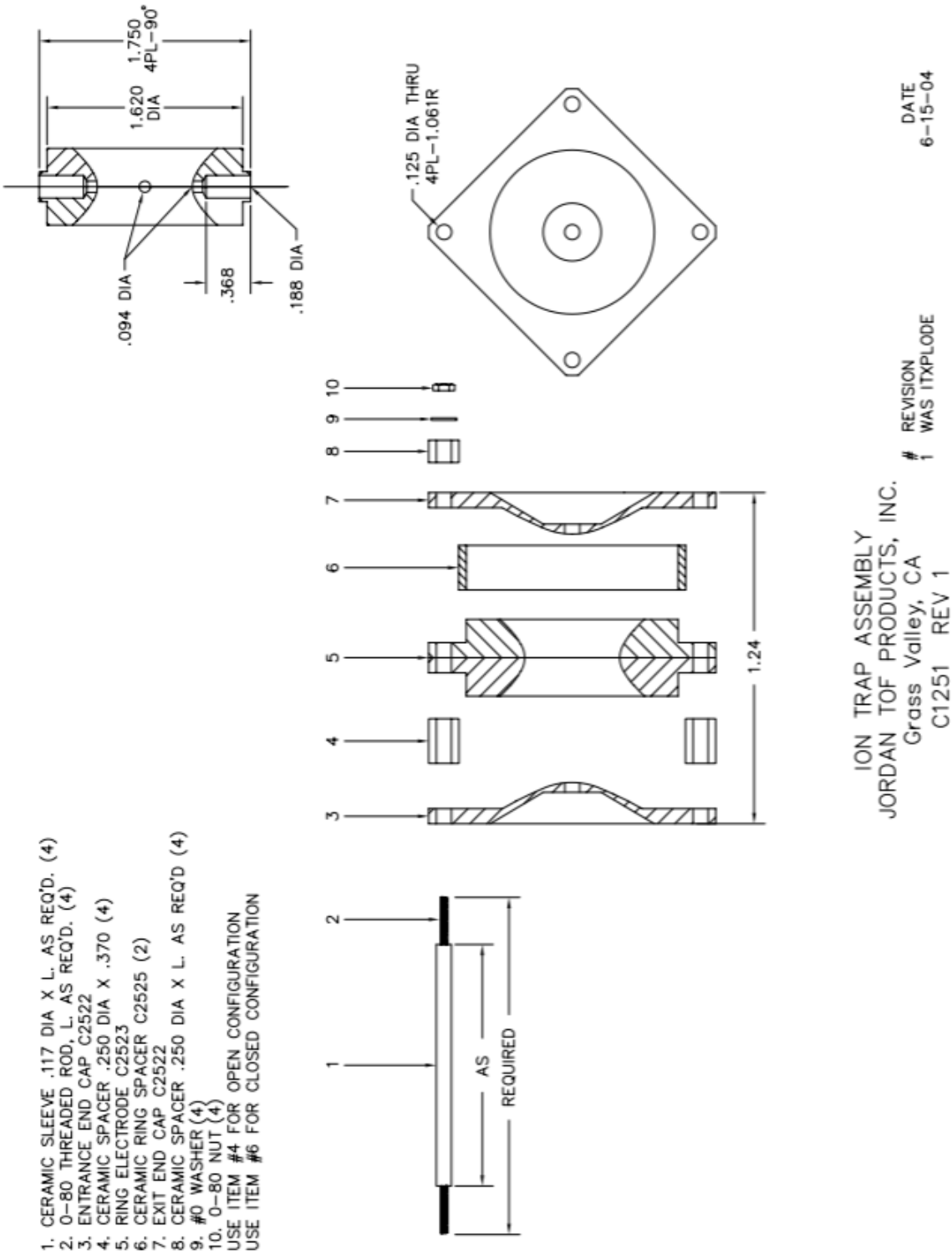

Figure 4.6. Schematic of the QIT purchased from Jordan TOF Products, Inc.

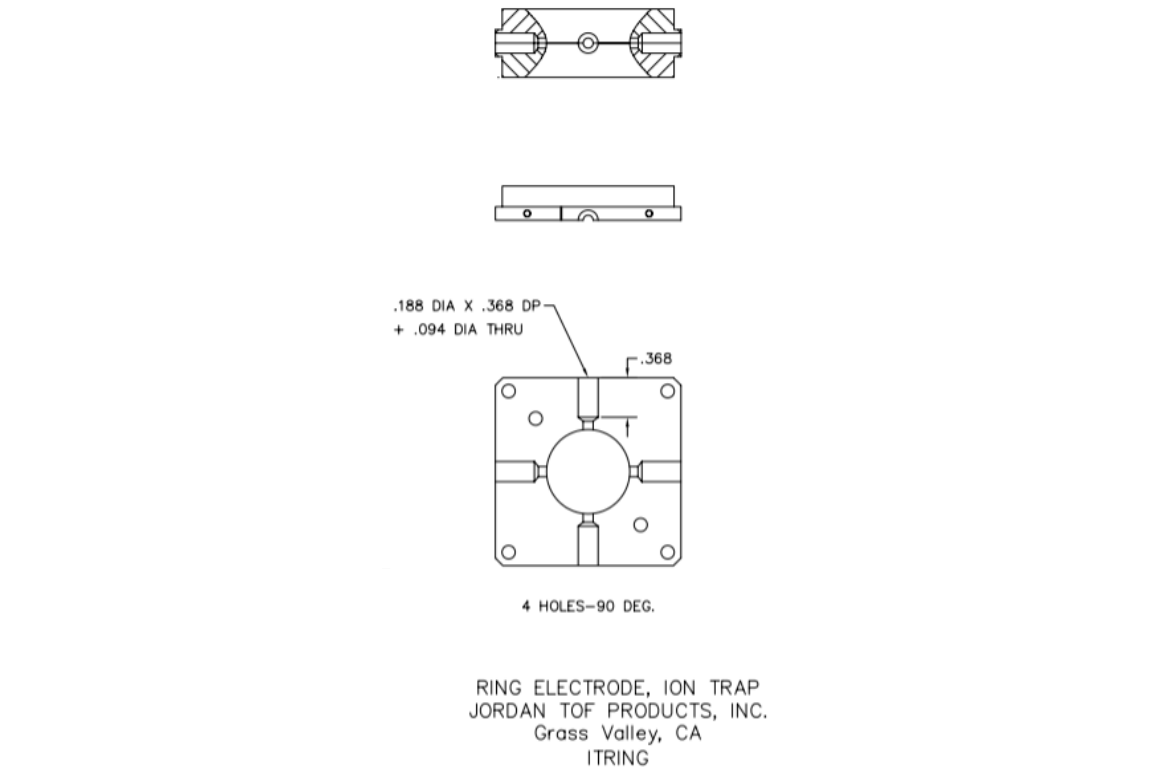

Figure 4.7 Schematic of the 4-hole pattern and picture of the components of the QIT purchased from Jordan TOF Products, Inc.

stage of a cryogenic refrigerator cold head (Model 22C cold head with Model SC (Air) Compressor, CTI-Cryogenics), thereby both mounting the QIT inside the chamber and cooling the trap. The second stage of the cold head can achieve cooling down to a few Kelvin, but has less cooling power than the first stage which can only cool down to ~70 K. The trap shielding was designed in two parts, an inner and outer shielding. The inner shielding attached the trap directly to the second stage of the cold head and was made with 99.9% purity copper, as copper is an efficient thermal conductor. Placed between the QIT and the inner shielding piece was a 1 mm sapphire plate. This plate served to electrically isolate the QIT from the copper shielding while still providing good thermal conductivity. Copper wafers 1 mm in thickness were also designed to sit between the inner shielding and the cold head for adjusting how far the QIT extended into the chamber for alignment purposes. Figure 4.8 illustrates the details regarding the design of the inner shielding and QIT.

The outer shielding was made of gold-plated copper and attached to the first stage of the cold head, displayed in Figure 4.9. The gold-plated copper decreased the likelihood of RF heating inside the QIT. The outer shielding acted as a thermal radiation shield and maintained the low temperatures surrounding the QIT. Essentially, the outer shielding became the surroundings for the QIT and reduced the power required to cool the QIT, while also reducing the radiative RF heating. The outer shielding allowed the cooling power of the second stage to be used solely to cool the QIT and the buffer gas inside it to ~10 K from an already-low temperature of ~70 K. This shielding was also designed in two pieces. The top piece housed electrical connections to feed the wires through the adapter to the trap, precooling them and reducing the overall thermal load on the trap. The wires were

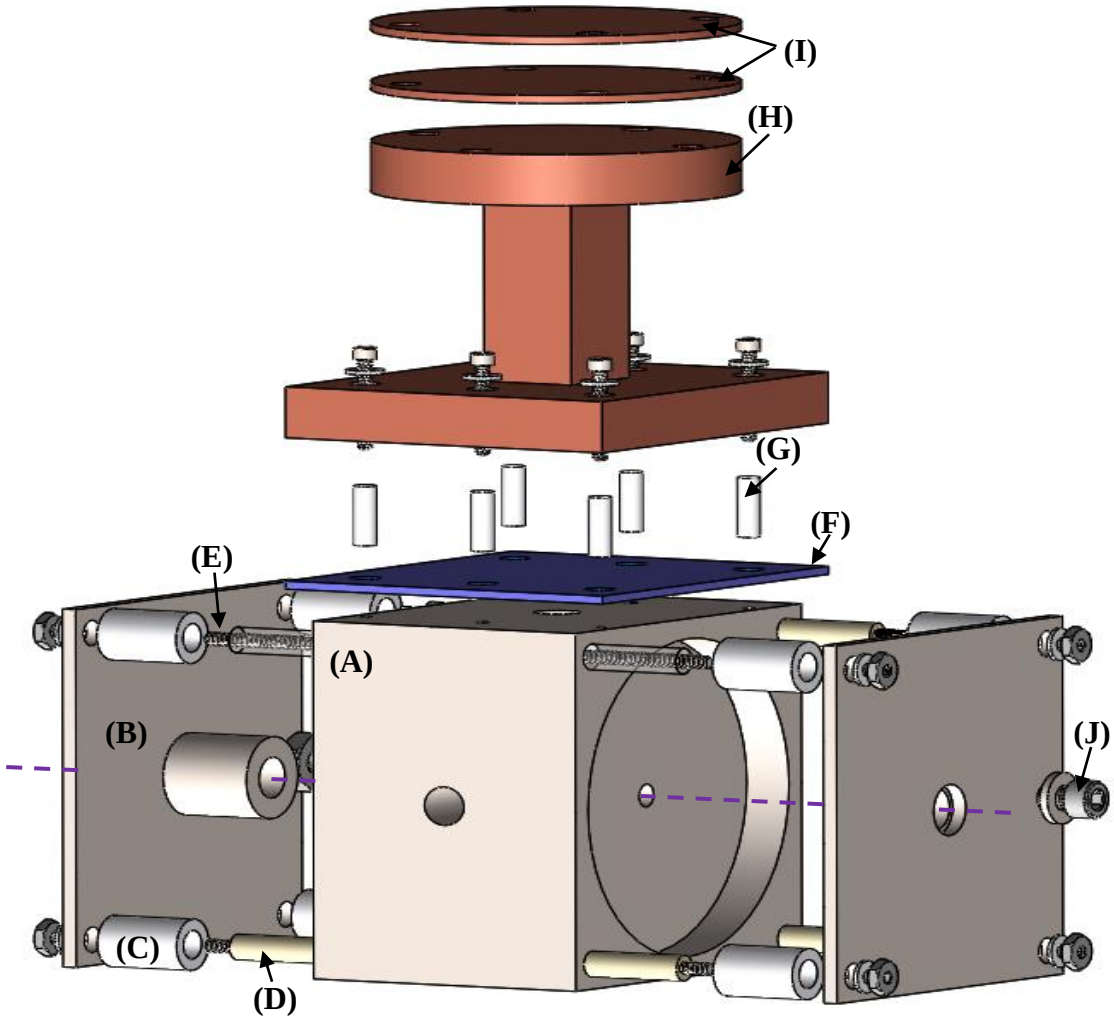

Figure 4.8. Drawn to scale. The purple dashed line represents the path of the molecular beam. (A) Representation of the QIT. (B) Entrance/Exit tube lens for focusing ions. (C) Electrically insulating spacer between the tube lens and QIT. (D) Alumina tube. (E) 0-80 threaded rod (alumina tube translucent to show rod went through the entire QIT and lens set up). (F) 1 mm thick sapphire plate. (G) Alumina insulator tube, electrically insulated the 0-80 bolts (with no. 0 alumina washers) that attached the inner shielding to the QIT. The electrical connection to the QIT was made by wrapping the wire around these bolts and screwing them into the QIT. (H) 99.9 % pure copper inner shielding. (I) 1 mm thick copper wafers. (J) 4-40 bolt and hole for applying voltage to the tube lens.

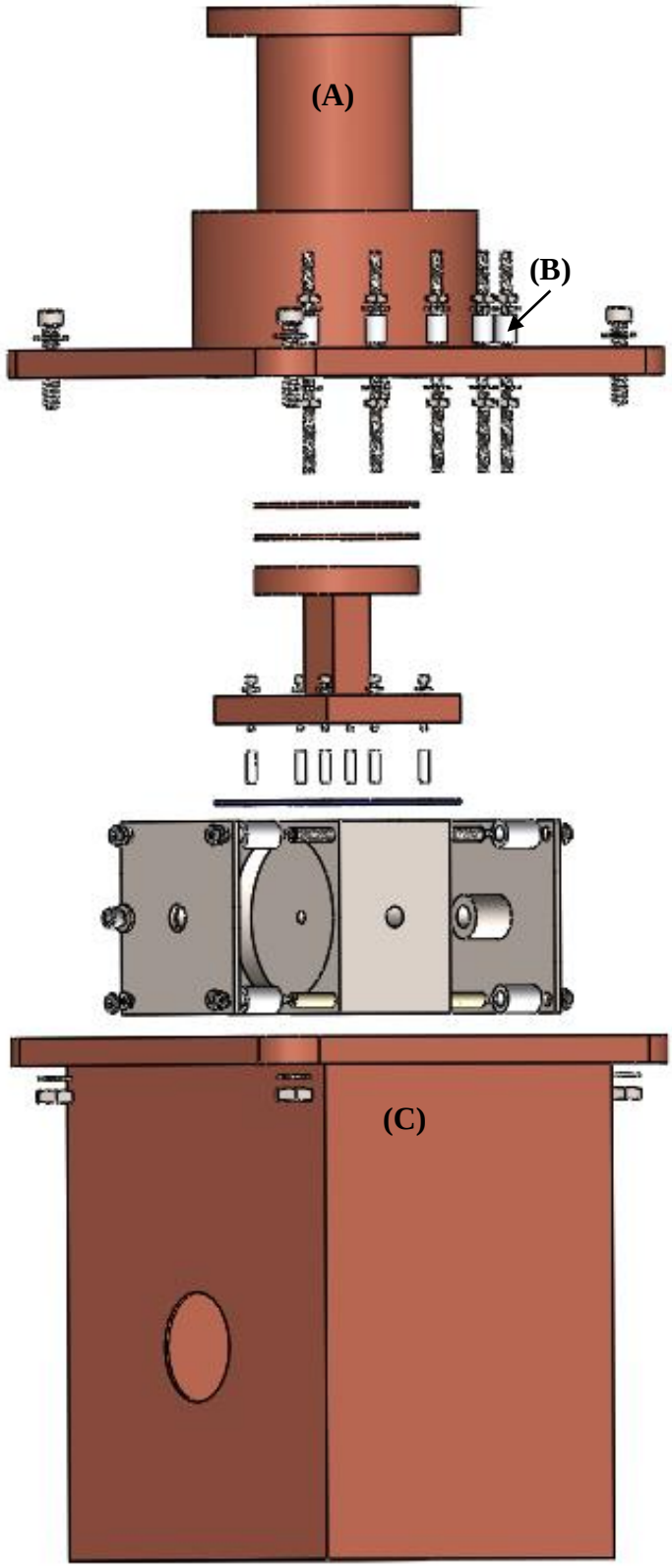

Figure 4.9. Inner and outer QIT shielding and mounting assembly. Drawn to scale. The shielding was made with gold-plated copper. (A) Top piece, mounted the isolated electrical connectors and was connected to the bottom shielding using 6-32 bolts. (B) Alumina tube, electrically isolated the threaded rod from the top piece of the outer shielding. The rods were fastened with alumina washers and stainless-steel hex nuts. (C) Bottom piece of the outer shielding, served as a radiative shield and as the environment surrounding the trap.

connected to vacuum feedthroughs for exiting the chamber; this portion of each wire was at room temperature. The top portion also included a hole through which to pass the stainless-steel tubing that delivered the buffer gas to the QIT. A cryogenic temperature sensor (DT-670, LakeShore Cryotronics) was placed between the top portion of the outer shielding and one of the 6-32 hex nut that mounted the piece to the first stage of the cold head. The temperature of the shielding was controlled using a temperature controller (Model 325, LakeShore Cryotronics). The bottom piece of the outer shielding was designed to be a shell around the trap, and was the part that created the cool environment around the QIT. Figure 4.10 displays an exploded view of the QIT and all of its shielding mounted to the arm of the cold head, along with the tubing for the buffer gas. This tubing was designed to feed into the chamber using a ¼ in Yor-Lok adapter. A short piece of 1/4 in stainless-steel tubing was welded to the vacuum side of the adapter. At the end of this tubing, a 1/4 to 1/16 in Yor-Lok adapter was connected, where 1/16 in tubing was added and wrapped around the top piece of the outer shielding to cool the buffer gas before it entered the QIT. Another adapter mated the 1/16 in tubing to the 0.059 in stainless-steel tubing that was fed through the hole in one of the ceramic spacers of the QIT (0.06 in diameter). Figure 4.11 presents the collapsed view of Figure 4.10.

A QMF was required to mass select and guide the ions into the QIT. The QMF and its power supply were originally purchased from Extrel Corporation (QMF Model 7-324-9, 19 mm rod diameter and Extranuclear 150-QC Series Quadrupole Power Supply) but were recently refurbished by Ardara Technologies L.P. The QMF was mounted inside of an 8 in double-sided ConFlat radial flange (Model FLAN_MNTG_80CF_RAD_04) and equipped with entrance and exit lenses, a conductance-limiting plate, and an upstream

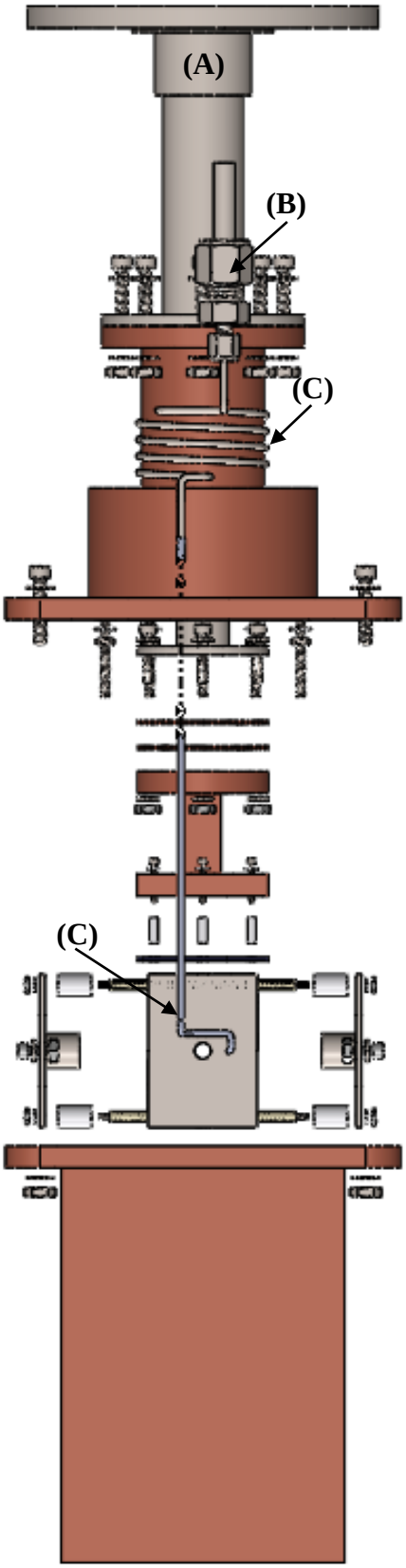

Figure 4.10. Exploded view of entire QIT and shielding assembly mounted to the arm of the cold head. Drawn to scale. The temperature censor was wedged between the top portion of the outer shielding and one of the 6-32 hex nuts that assisted in mounting the top piece to the first stage of the cold head. (A) Cold head arm. (B) Yor-Lok adapter. (C) Buffer gas tubing.

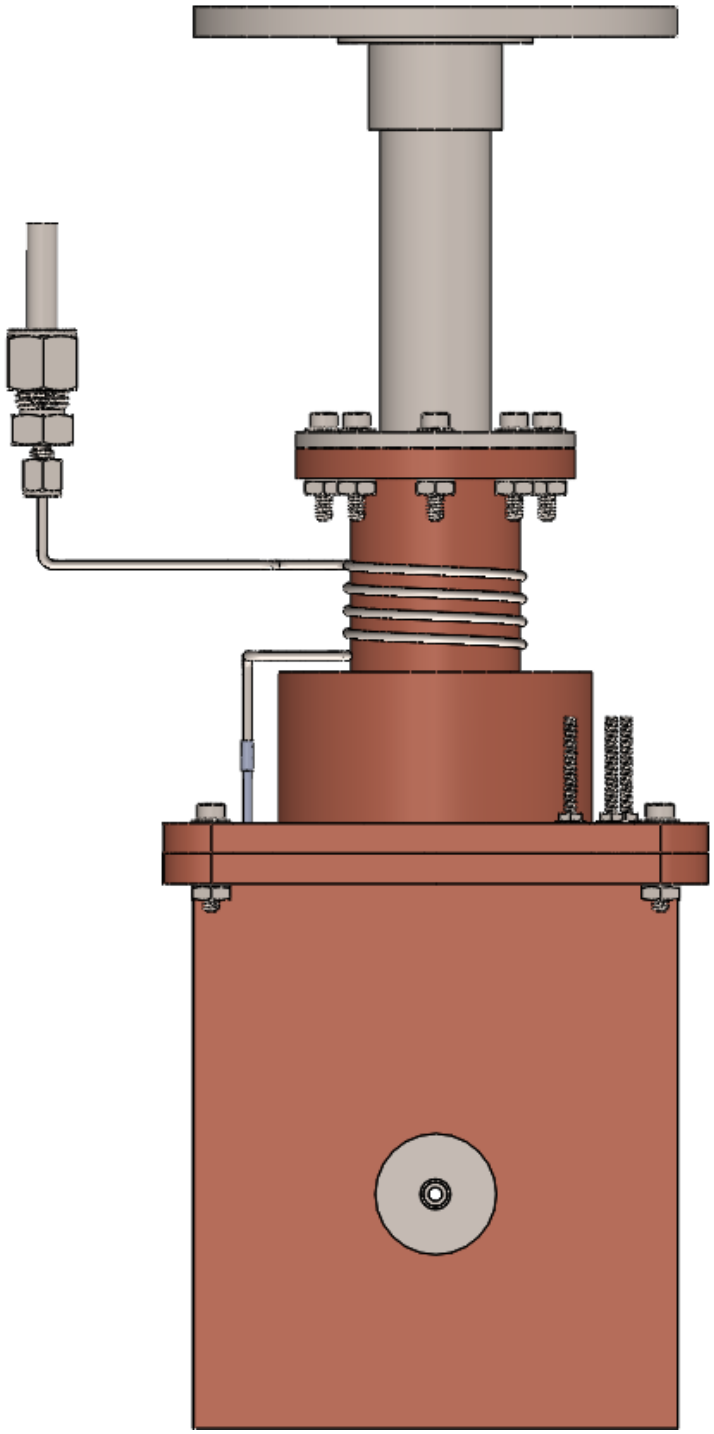

Figure 4.11. Normal view of the QIT and shielding assembly attached to the cold head arm, drawn to scale. Buffer gas tubing included.

conductance-limited, vented downstream housing by Ardara Technologies L.P. This company also improved and repaired portions of the Extrel Corporation 150-QC Power Supply to make it compatible with the ports on the radial flange. These ports were designed for connecting the necessary wires to the lenses and QMF. Images of the mounted QMF can be seen in Figure 4.12.

Two new chambers were designed to replace the previous source chamber and hold the ablation source, QMF, QIT, and the mass spectrometer because the previous setup was not conducive for adding the QMF and QIT. The mass spectrometer mounting system was redesigned for the new chambers and is shown in Figure 4.13. The remaining two chambers used for BeO^- and BeS^- were unchanged. Figure 4.14 illustrates the design of the new source chamber. It was designed such that the volume of the chamber was large enough to prevent the diffusion pump, backed by a roughing pump, from being overloaded by the pulse valve. It was also shaped so that the distance from the ablation source to the QMF was be very short. The ablation source remained unchanged from the previous design, except for that it was placed on the opposite side of the chamber so that it was aligned collinearly with the skimmer on the QMF. The front of the chamber was sealed using a Plexiglas flange that contained a window through which the ablation laser passed. A flange port was placed on the top of the source chamber, aligned with the ablation source, so that laser-induced fluorescence spectroscopy could be easily performed in this chamber. A second flange port was placed next to the ablation source flange to include a port for the ion gauge and to add versatility to the chamber for future experiments.

The double-sided ConFlat radial flange that mounted the QMF was placed between the source chamber and QIT chamber. A nipple (union) was used to mate the source chamber

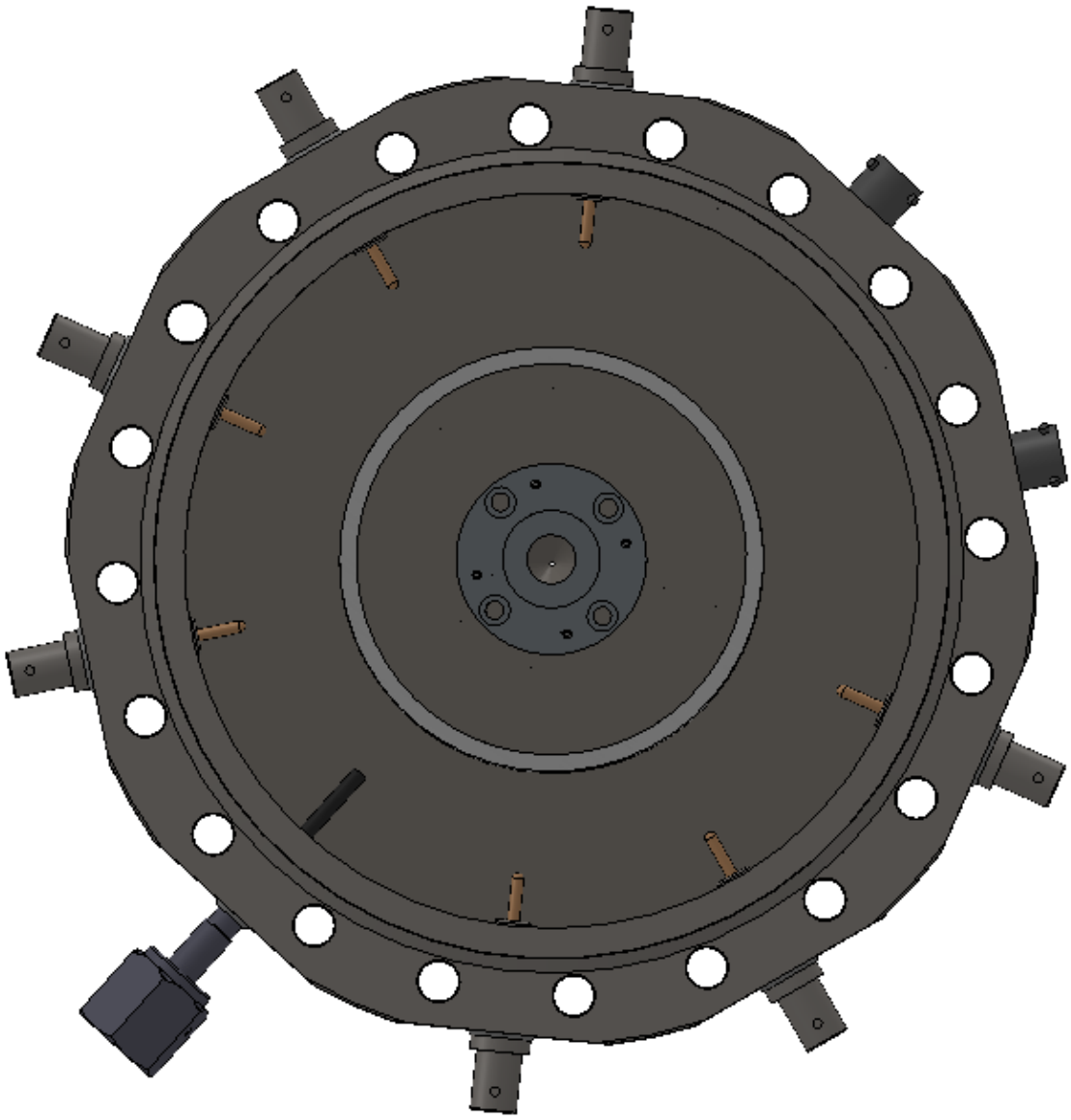

Figure 4.12a. Top view of the radial flange for mounting the QMF, drawn to scale. The ports located along the outer ring of the flange were for the QMF and lens connections. The center ring was the exit lens of the QMF.

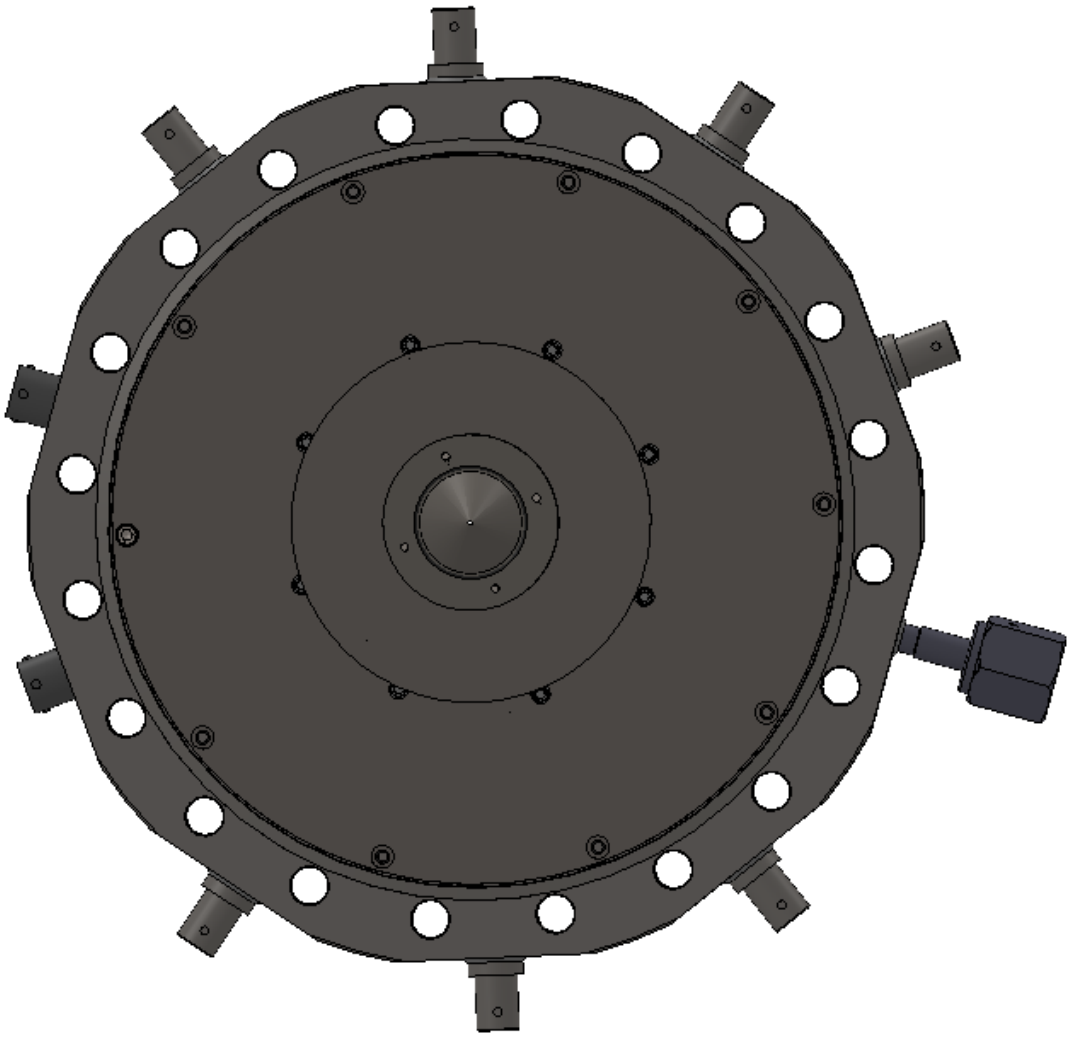

Figure 4.12b. Back side of the QMF radial flange, drawn to scale. The skimmer reduced the number of ions generated by the source that can enter the QMF. Behind the skimmer was the entrance lens to the QMF.

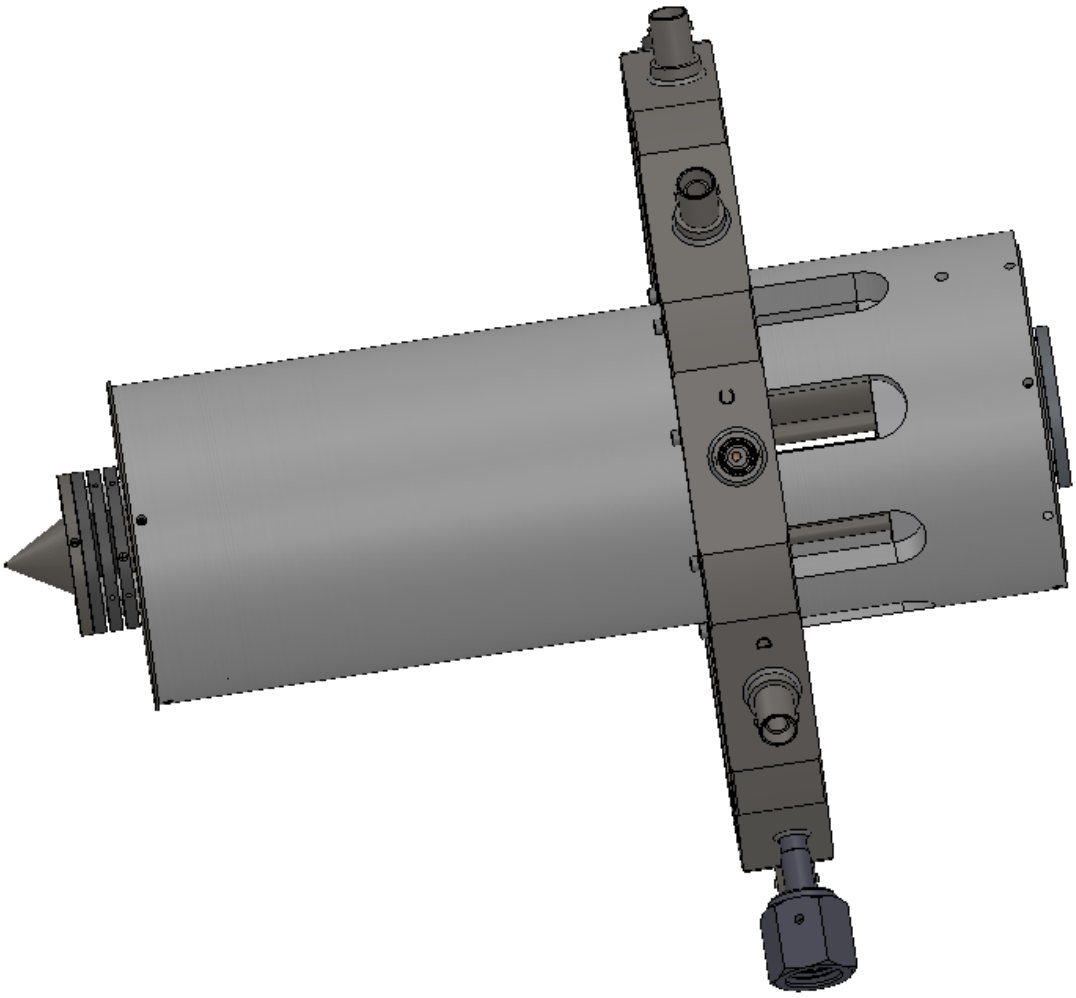

Figure 4.12c. Side view of the QMF and radial flange, including the QMF housing. Drawn to scale. Skimmer and entrance and exit lenses can be seen.

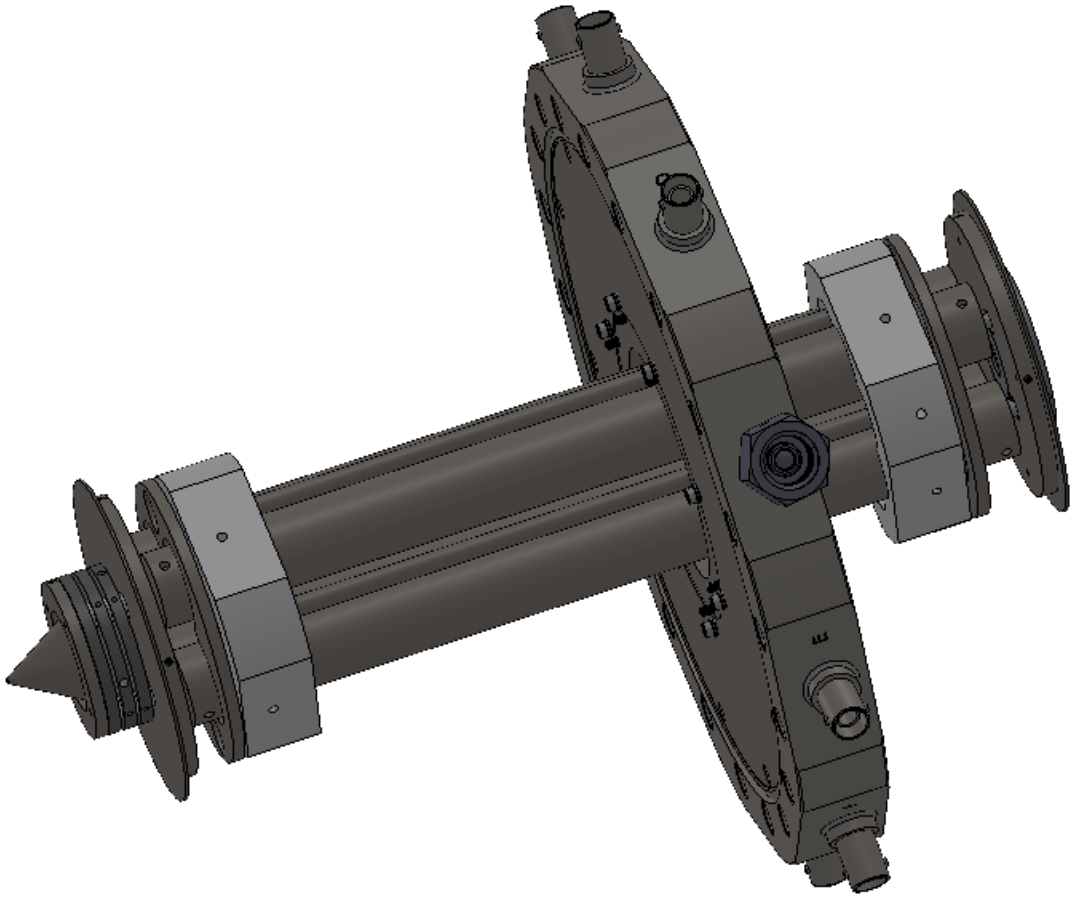

Figure 4.12d. Side view of the QMF and radial flange, excluding the QMF housing. Drawn to scale. The four, mounted cylindrical rods of the QMF are shown.

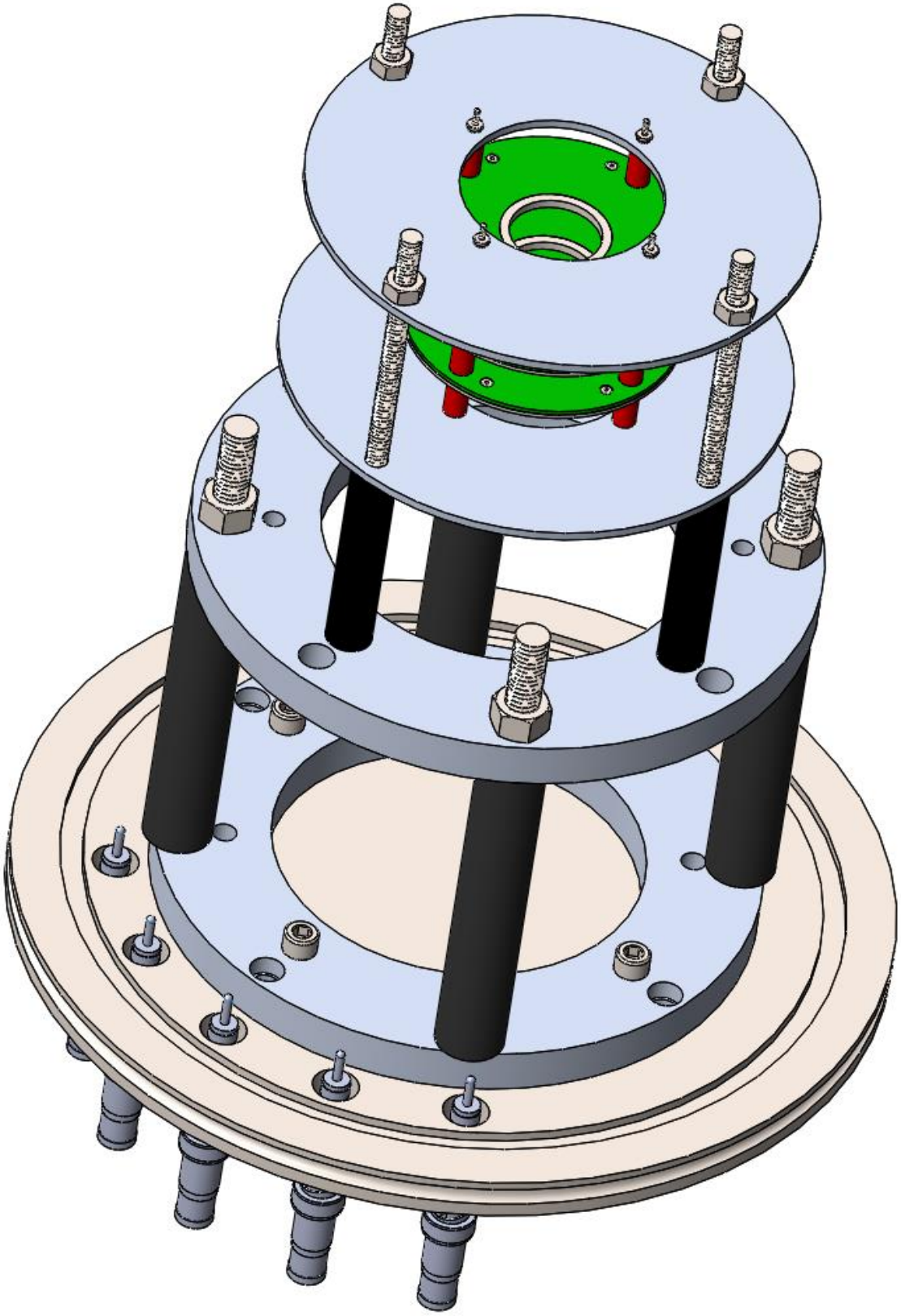

Figure 4.13a. View of the entire mounting assembly and mass spectrometer, drawn to scale.

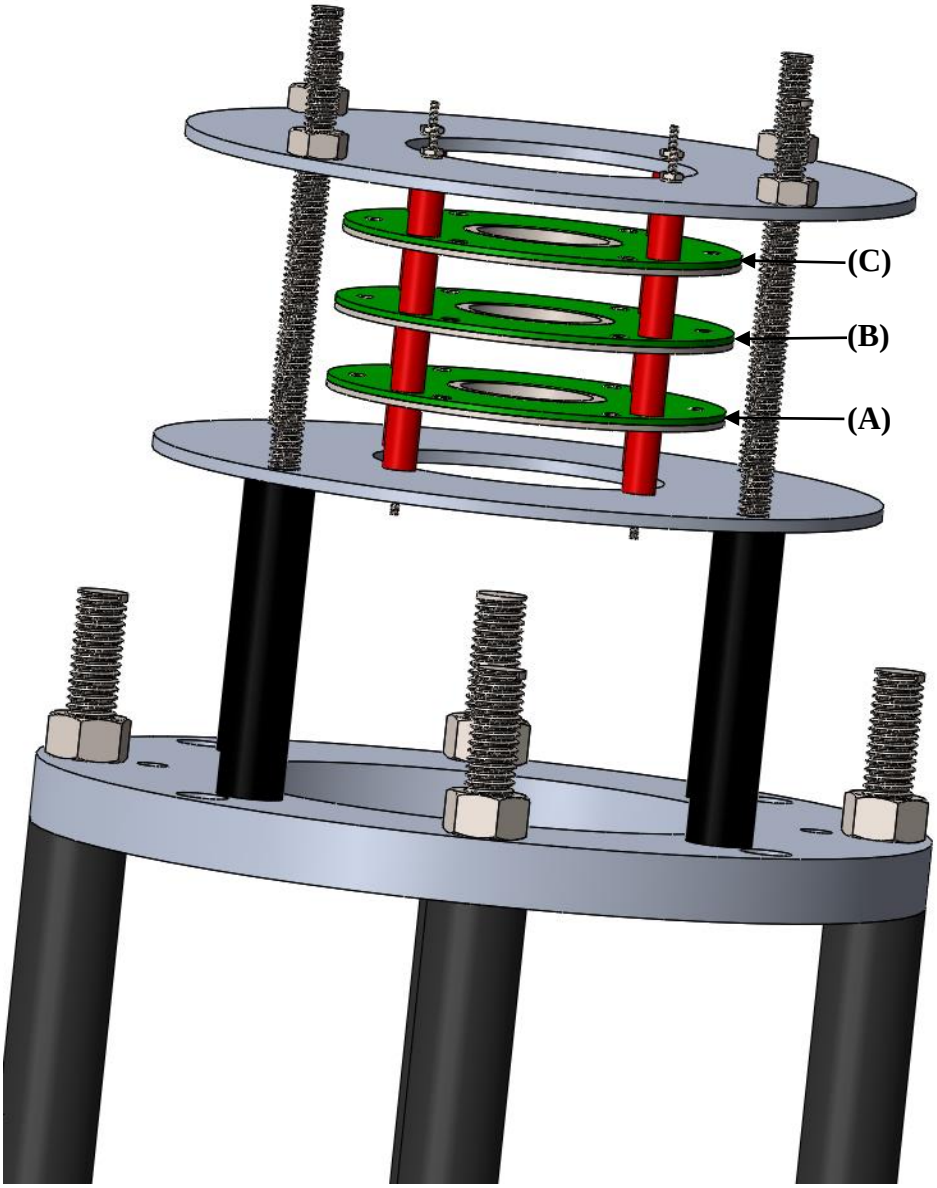

Figure 4.13b. Side view of the mounted mass spectrometer. Drawn to scale. Each mass spectrometer plate stack was separated from each other by ceramic spacers and mounted using alumina tubes over 0-80 threaded rods for electrical insulation. Each stack consisted of a top plate and a bottom plate. Between the two plates a fine gold mesh was placed, covering the opening in each plate to create uniform electric fields inside the mass spectrometer. (A) Repeller plate stack. (B) Extractor plate stack. (C) Grounded plate stack.

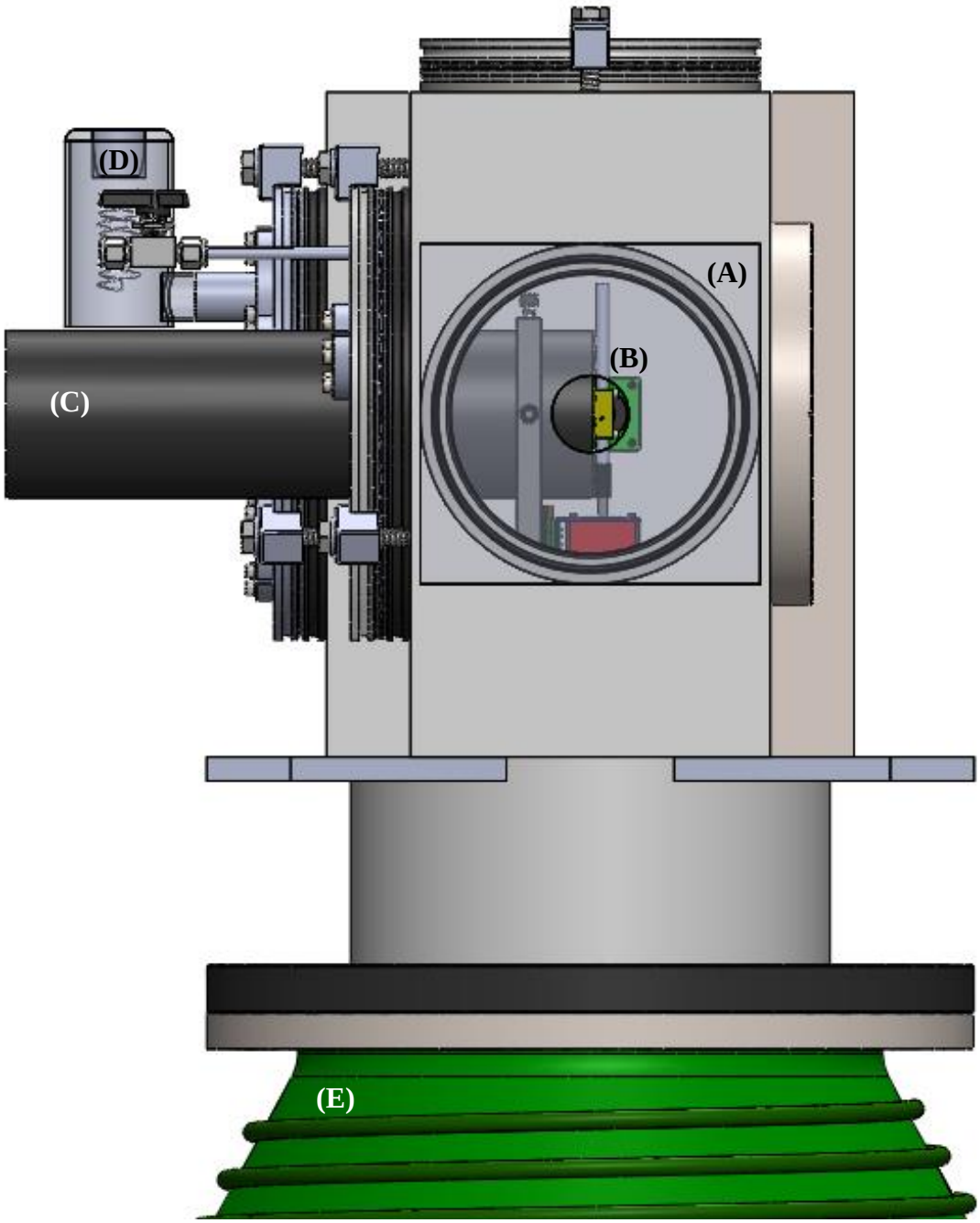

Figure 4.14a. Front view of the source chamber designed for use with the QIT and QMF, designed to scale. (A) Plexiglas flange. (B) Ablation Source. (C) Pulse Valve (Jordan TOF Products, Inc.). (D) Ion gauge. (E) Diffusion pump.

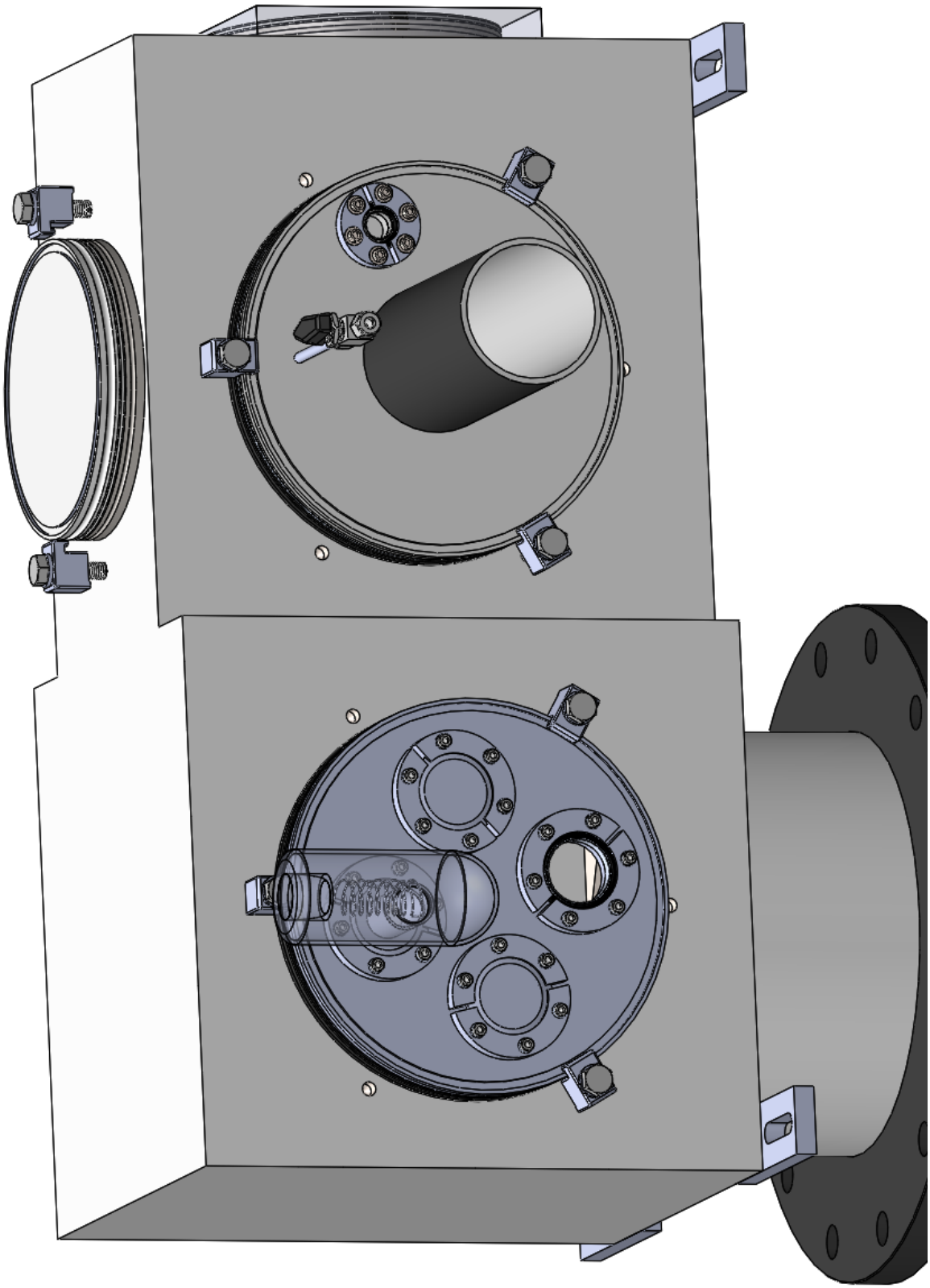

Figure 4.14b. Pulse valve and ion gauge side of the new source chamber, drawn to scale.

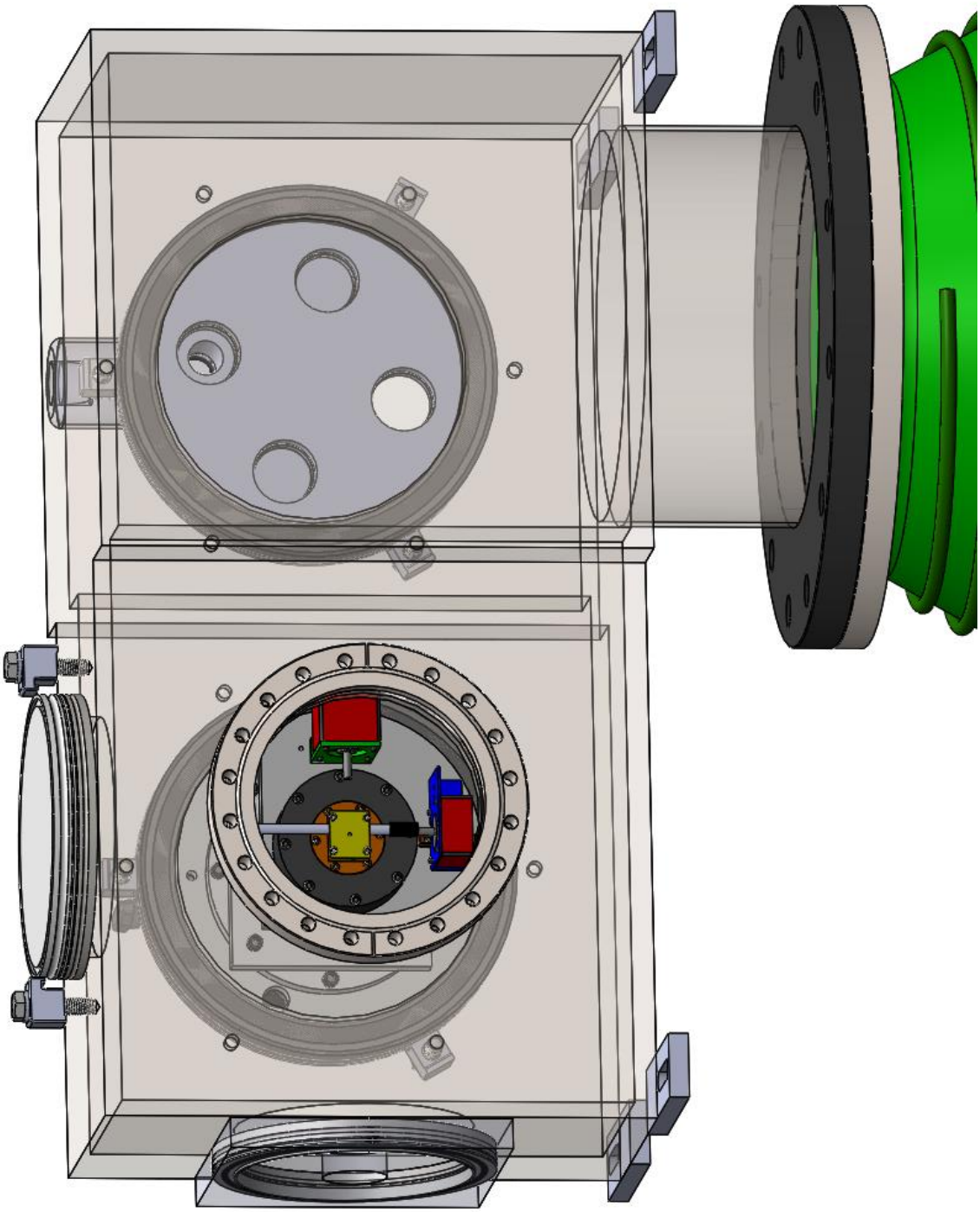

Figure 4.14c. Side view of the source chamber, drawn to scale. Chamber is translucent so that the inside of the chamber may be seen. The ablation source was mounted on the pulse valve.

to the QMF flange. The QMF mounted such that it was centered inside of the nipple, with the exit lens located near the opening of the outer shielding of the QIT (mounted inside the new QIT chamber). This placement ensured that the ions exiting the QMF would travel into the QIT.

The QIT chamber was designed so that the trap could be placed near both the exit of the QMF and the entrance of the perpendicularly aligned WM-TOF mass spectrometer and is depicted in Figure 4.15. The mass spectrometer was placed so that the center of the molecular beam traveled directly between the repeller and extractor plate.

Collinear to the molecular beam, a flange port was placed on the QIT chamber so that a viewing port or a set of MCPs could be mounted there. The MCPs served to detect if the molecular beam was successfully traveling through the center of the mass spectrometer. On the same side, another flange port was added downstream of the molecular beam so that ion optics could be mounted there if needed. The flange for the QIT was placed on the top of the chamber, allowing the mounted QIT to be lowered into the chamber and aligned. The flange, depicted in Figure 4.16, also included two ports for electrical feedthroughs, the port for the Yor-Lok adapter, and a small viewing port. This port was positioned so it would be directly above the center of the mass spectrometer because it allowed for resonance-enhanced multi-photon ionization to be performed in the QIT chamber. Directly below the center of the mass spectrometer, on the bottom side of the chamber, was an identical port to allow for the exit of the multi-photon ionization laser. Also on the bottom of the chamber was the flange port for mounting the turbomolecular pump, which brought the chamber down to a vacuum of 10^{-7} torr, an ideal operating pressure for the QIT. Parallel with the mass spectrometer was another flange port which

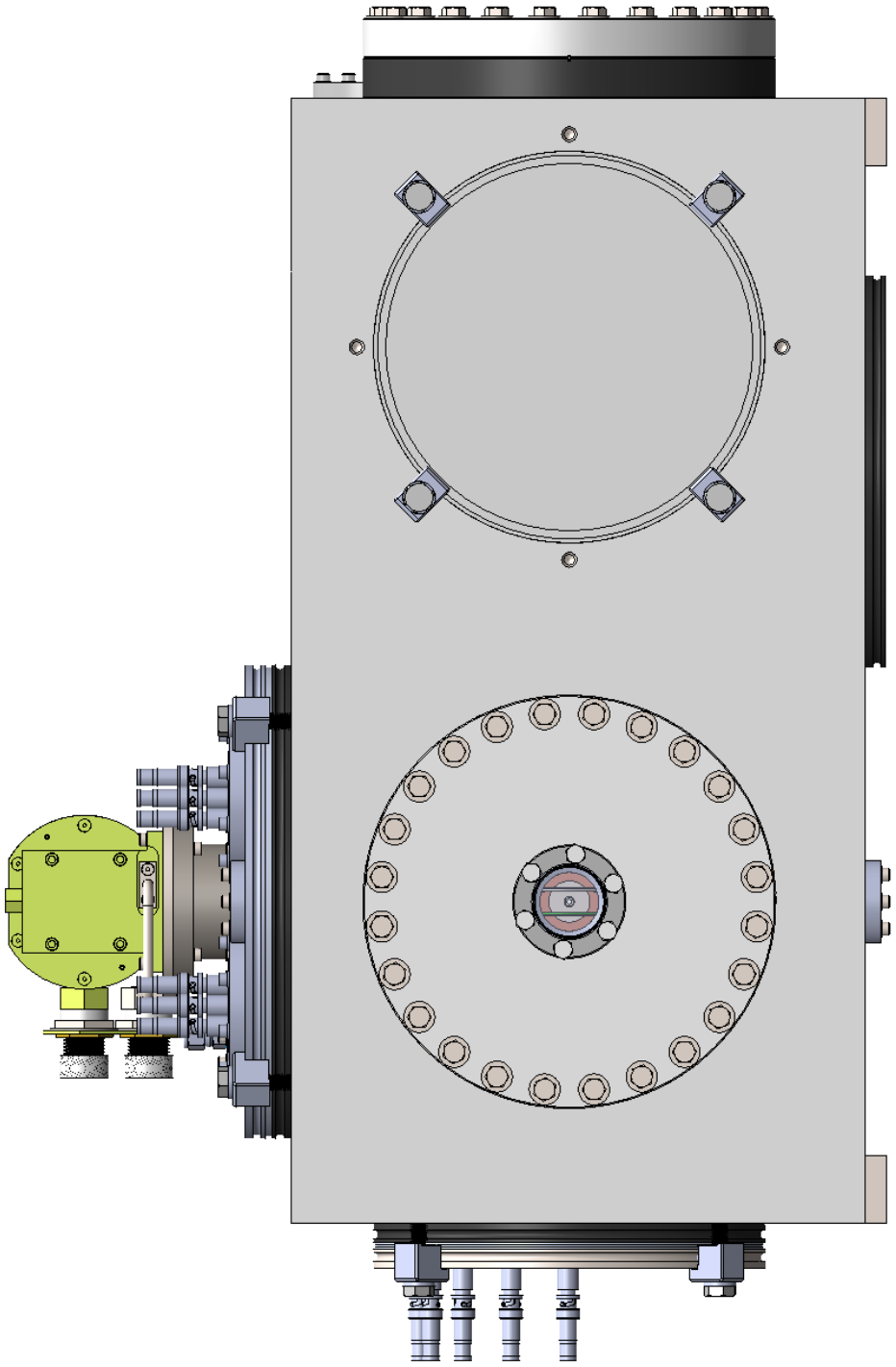

Figure 4.15a. Side view of the QIT chamber, showing the alignment of the QIT with the mass spectrometer. Drawn to scale. The electrical feedthroughs on the flange that mounted the mass spectrometer connected the mass spectrometer to the power supplies. The green apparatus was the cold head, mounted onto the QIT flange via a stainless-steel adapter.

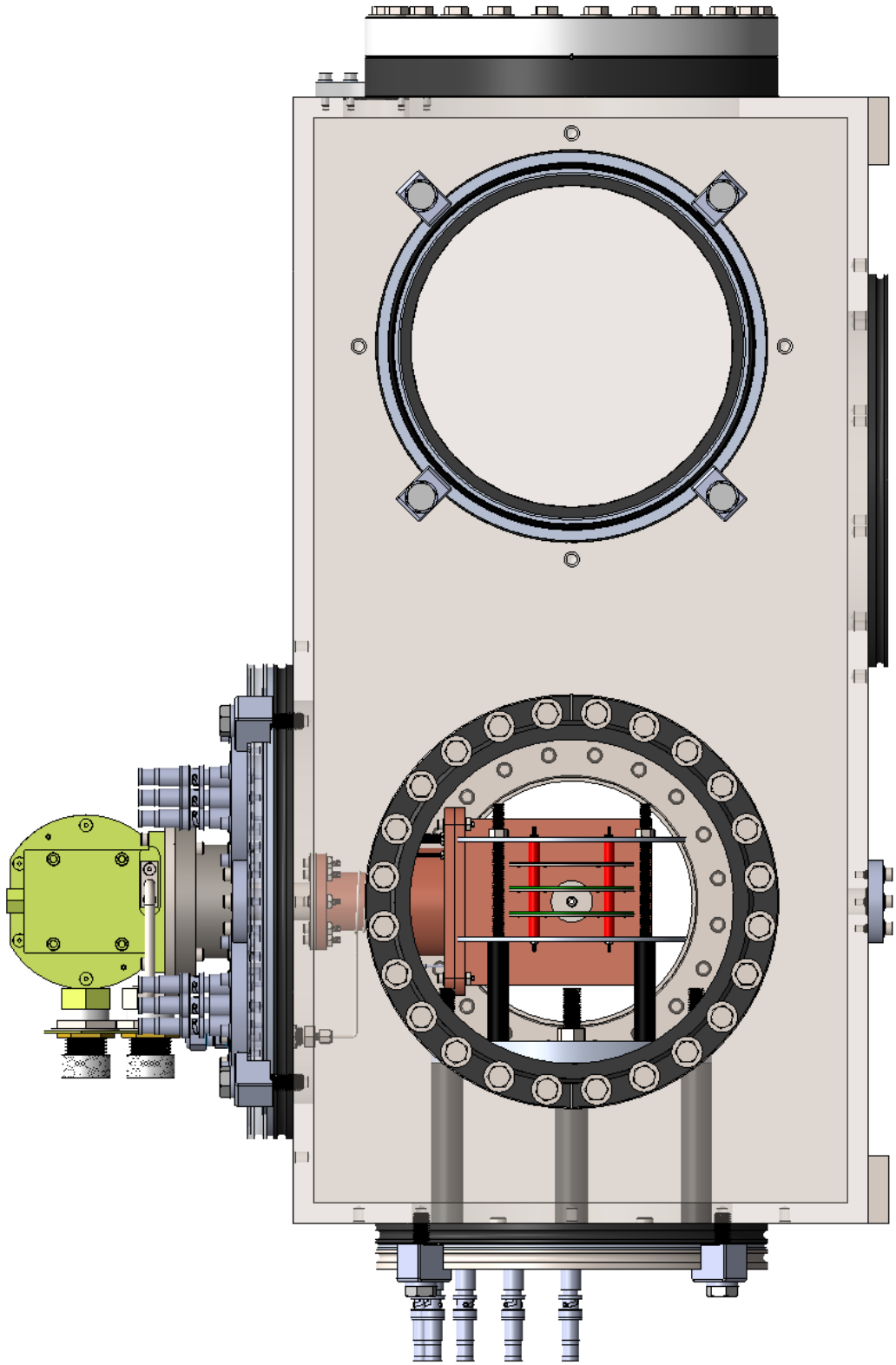

Figure 4.15b. Same perspective as 4.15a but with the viewing port flange removed and a translucent chamber. Drawn to scale.

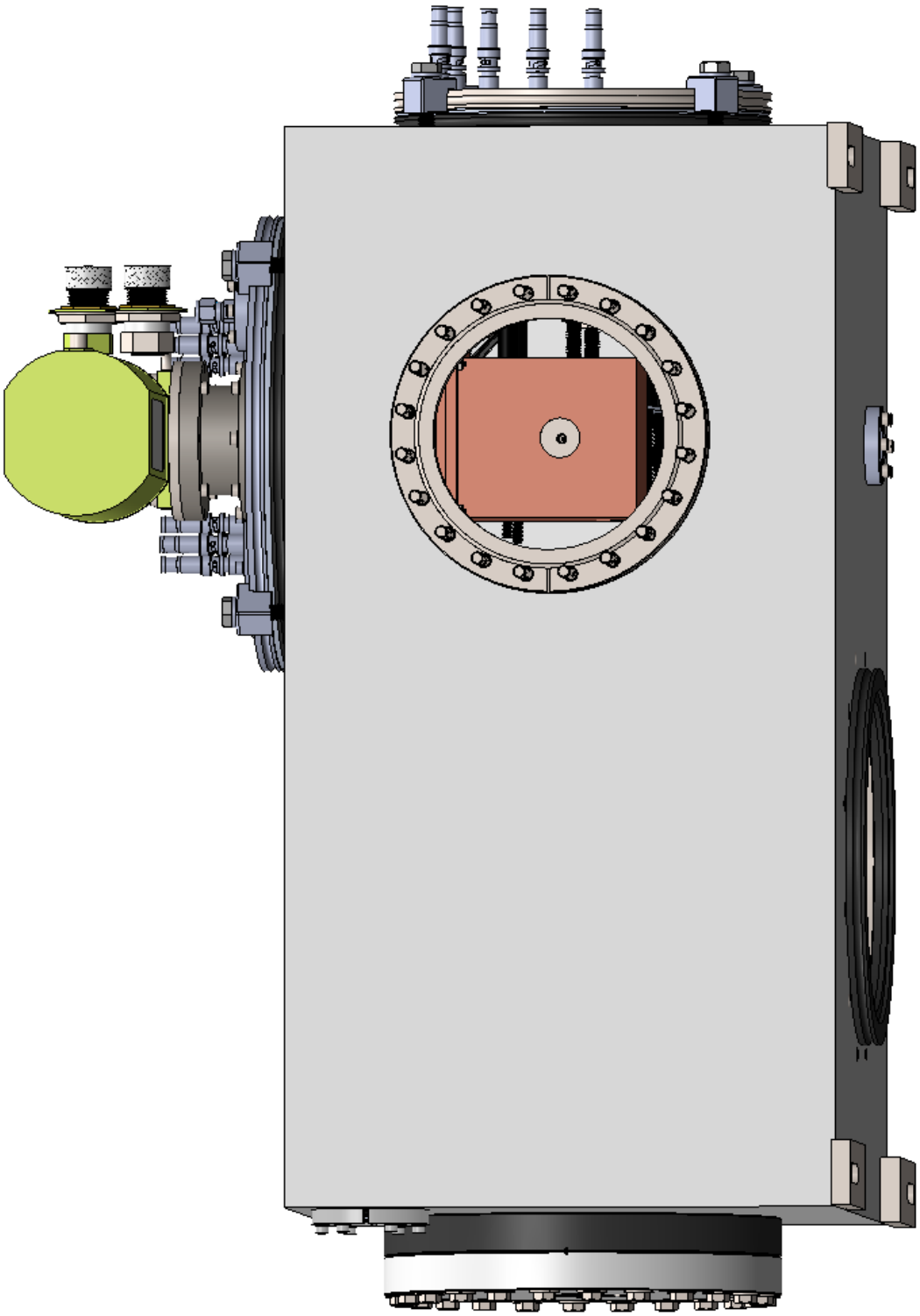

Figure 4.15c. Side view of the chamber, showing the port where the QMF was mounted. Drawn to scale.

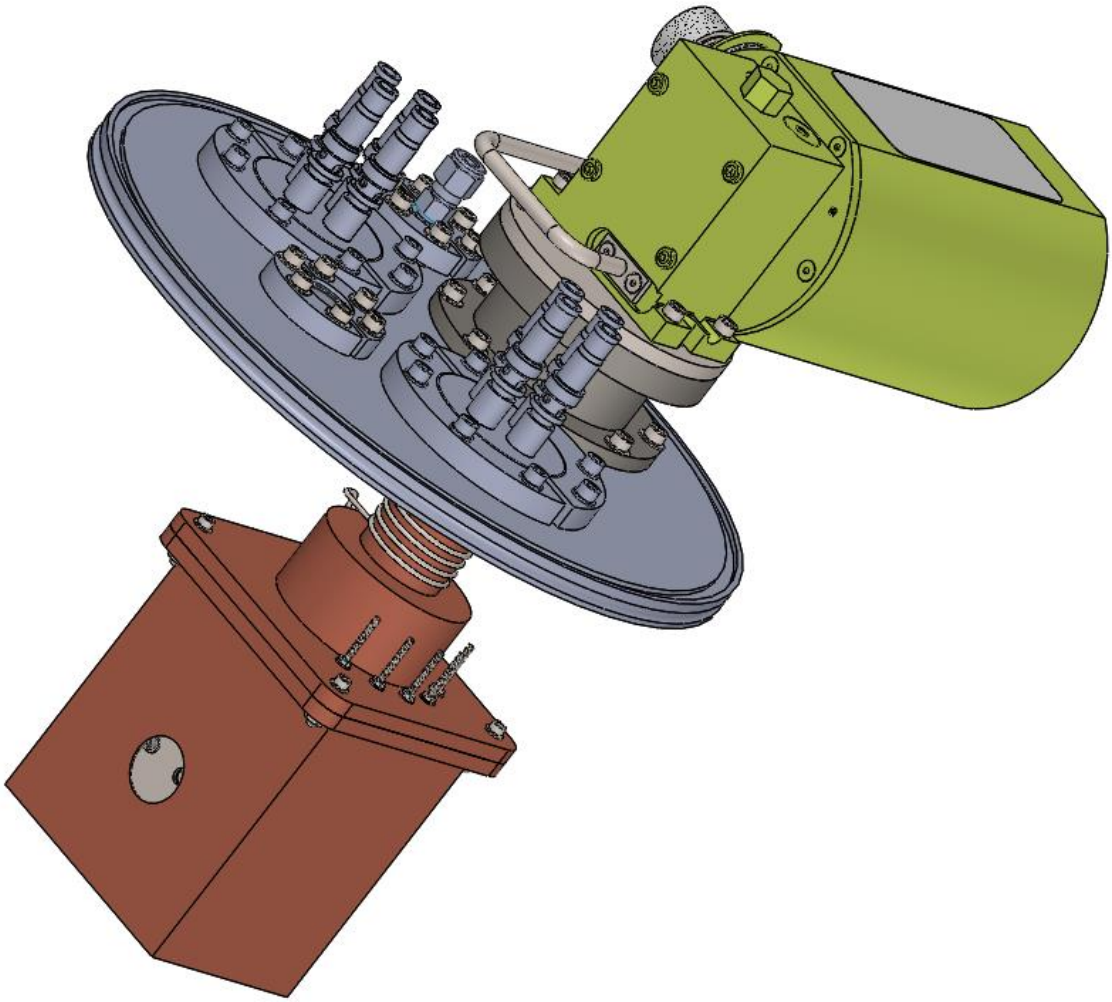

Figure 4.16a. QIT flange, drawn to scale.

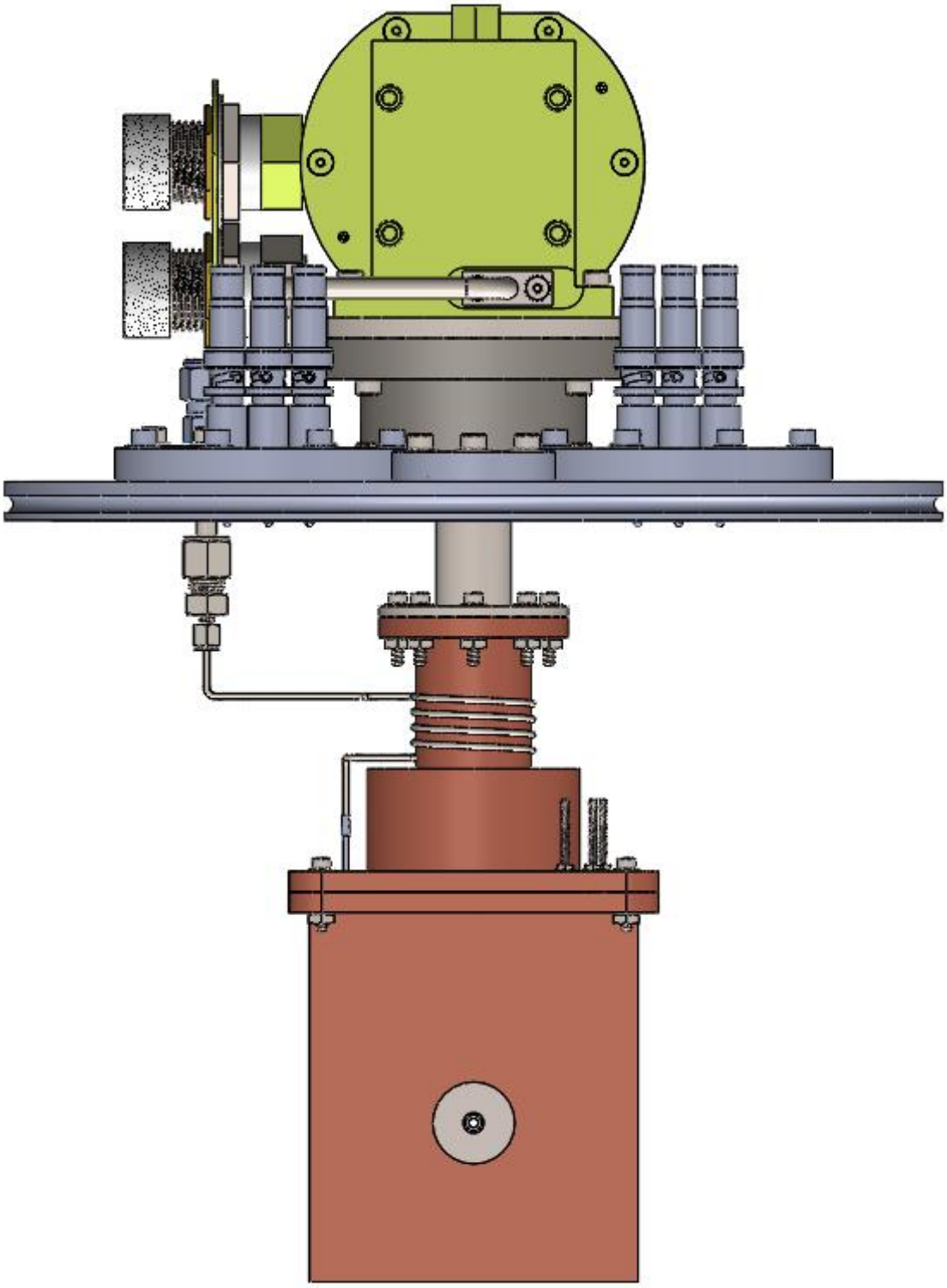

Figure 4.16b. Front view of the QIT flange. Drawn to scale.

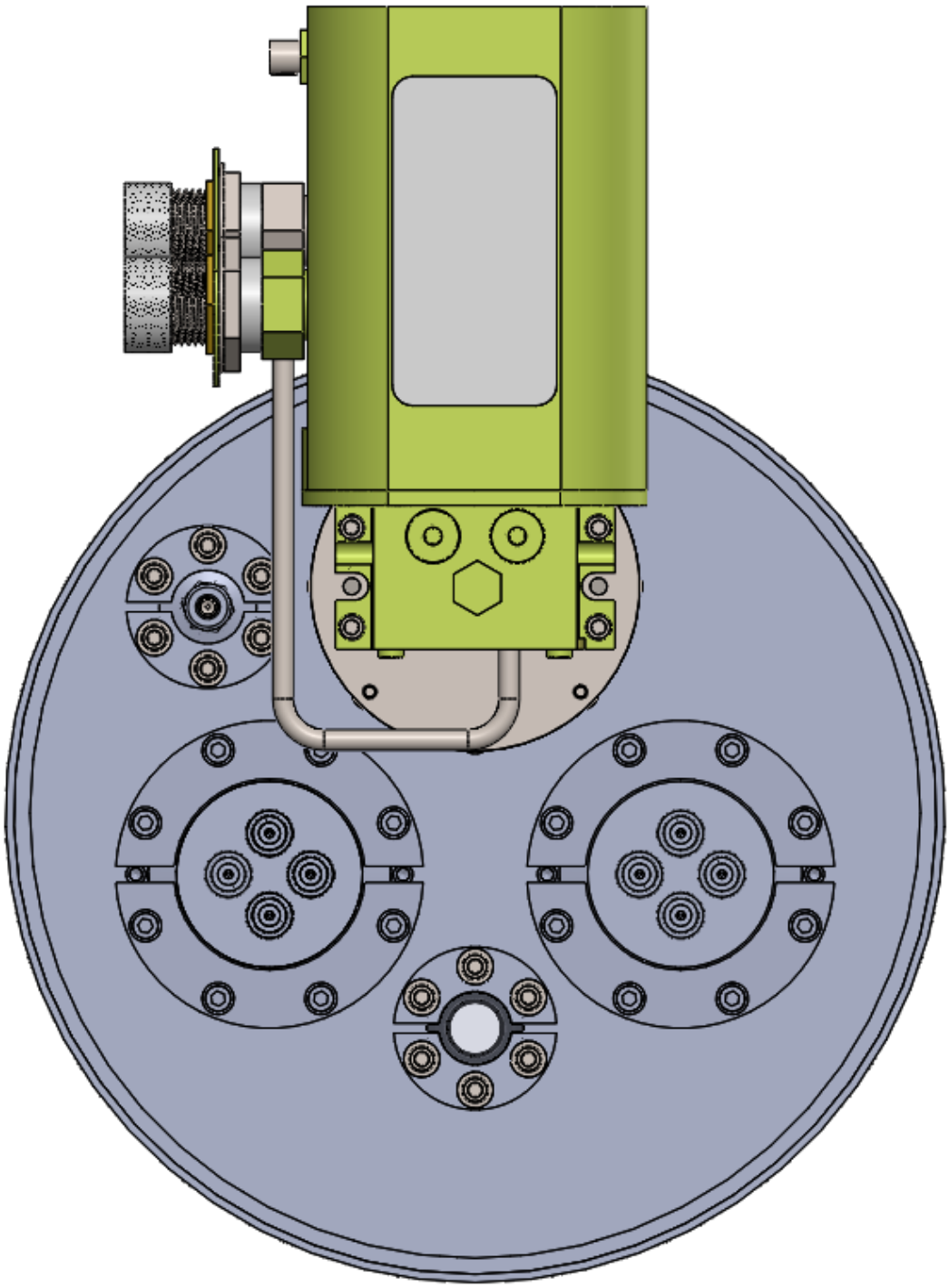

Figure 4.16. Top view of the QIT flange, drawn to scale.

connected the QIT chamber to the gate valve and following chamber. Additionally, a port was placed next to this exit flange port for the placement of an ion gauge. Both the source and QIT chambers were designed with mounting “feet,” allowing for easier mounting and alignment on the Unistrut structure built to hold the spectrometer. Figure 4.17 portrays the two chambers connected and mounted on the Unistrut, and Figure 4.18 shows the entire photoelectron velocity map imaging spectrometer fitted with a QIT.

For more details regarding the design of the chambers, QIT, or QMF, the reader can refer to the documents found in the Emory University web drive of Dr. Michael Heaven (Directory: R:\HeavenLab\SoildWorks Part, Assemblies, and Software\SEVI and Pre-SEVI Stuff). Instructions for building the shielding around the QIT can be found on the web drive as well (Directory: R:\HeavenLab\Amanda Dermer\Instructions for Ion Trap Assembly). These documents include all layouts and dimensions that may be necessary for constructing and maintain the new chambers, QMF, and QIT assemblies.

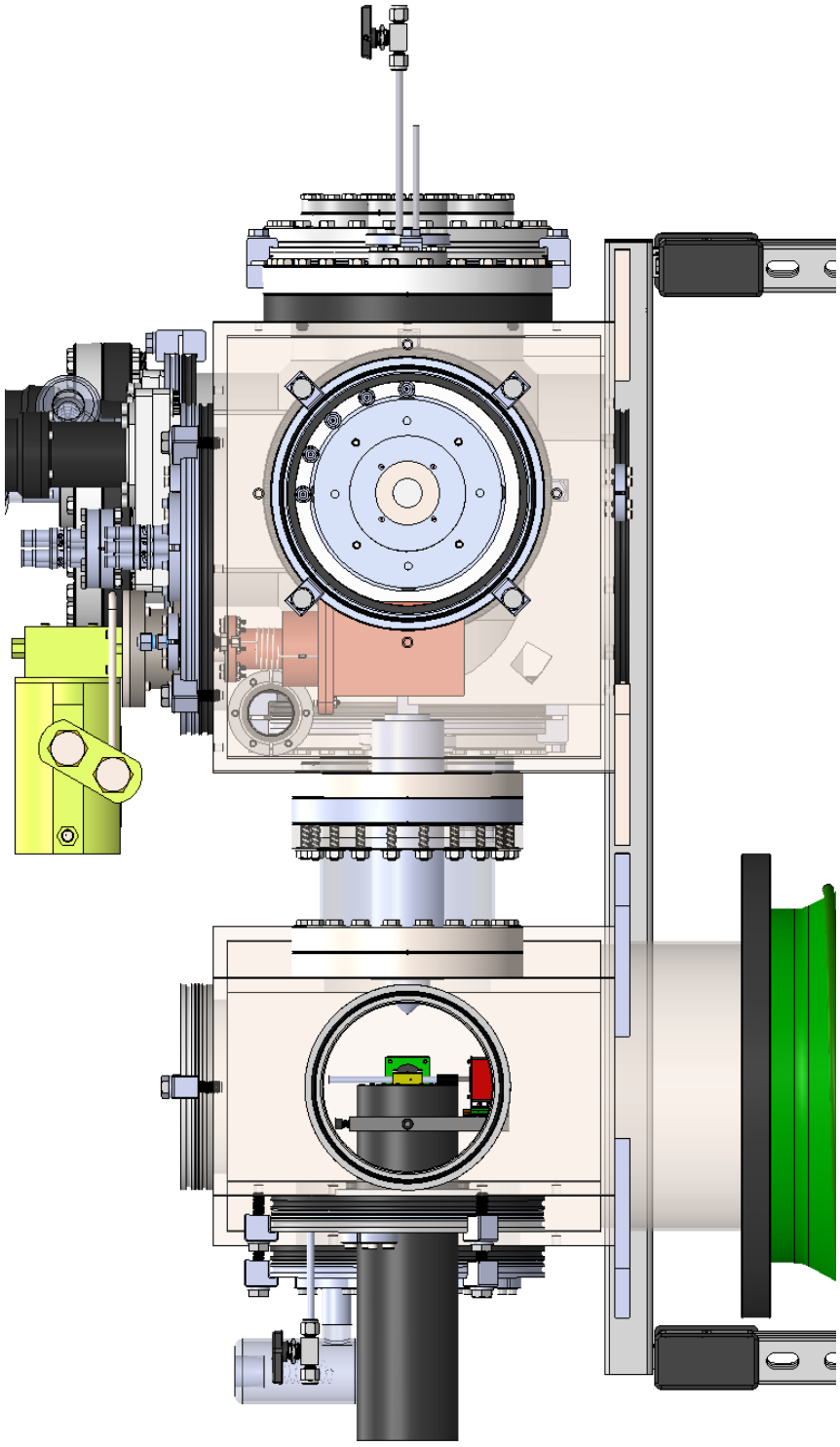

Figure 4. 17. Source chamber and QIT connected via a nipple and the QMF radial flange. Chambers and nipple are translucent. Drawn to scale.

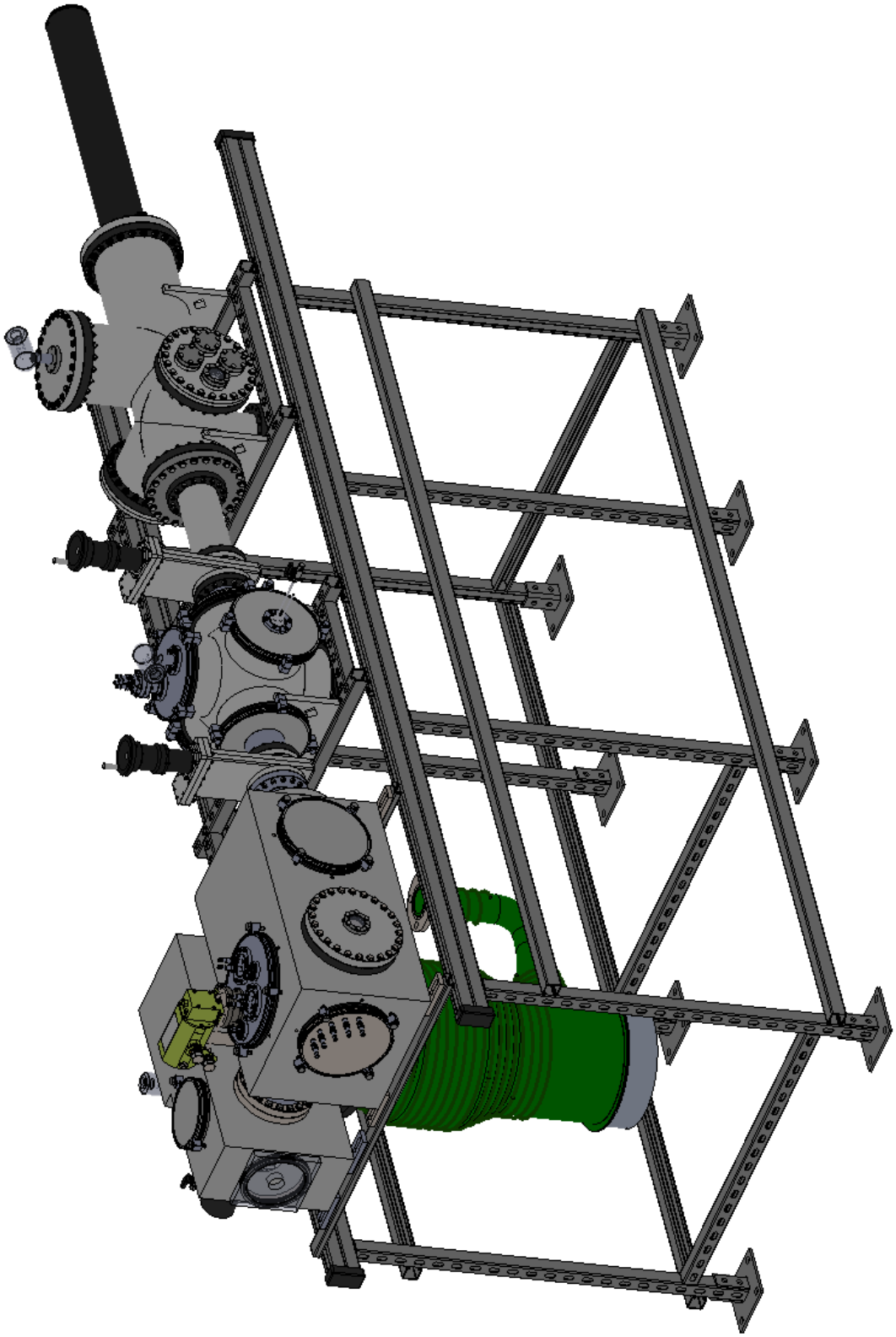

Figure 4.18a. Entire photoelectron velocity map imaging spectrometer with the QIT, mass spectrometer side. Drawn to scale.

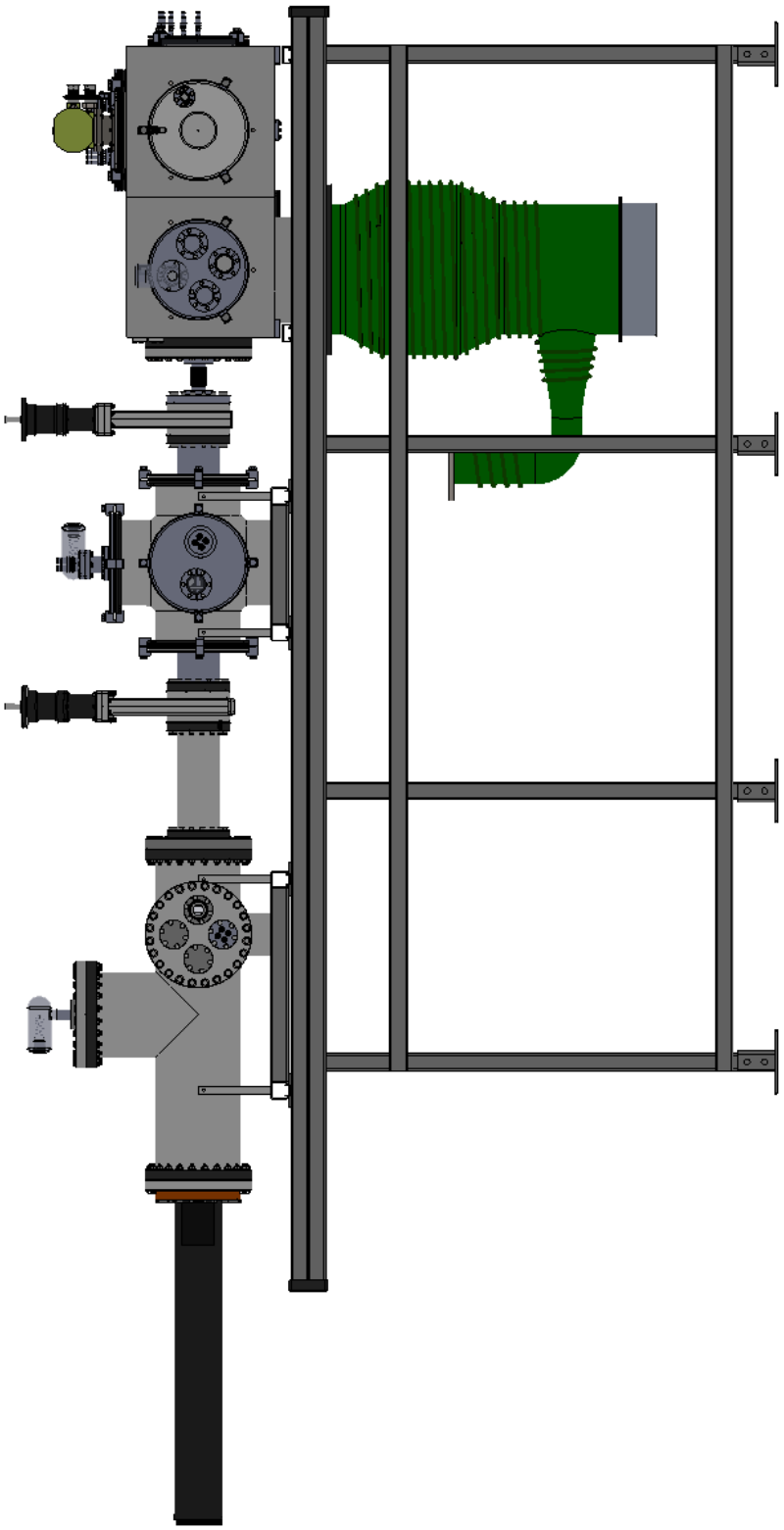

Figure 4.18b. Entire spectrometer, pulse valve side. Drawn to scale.

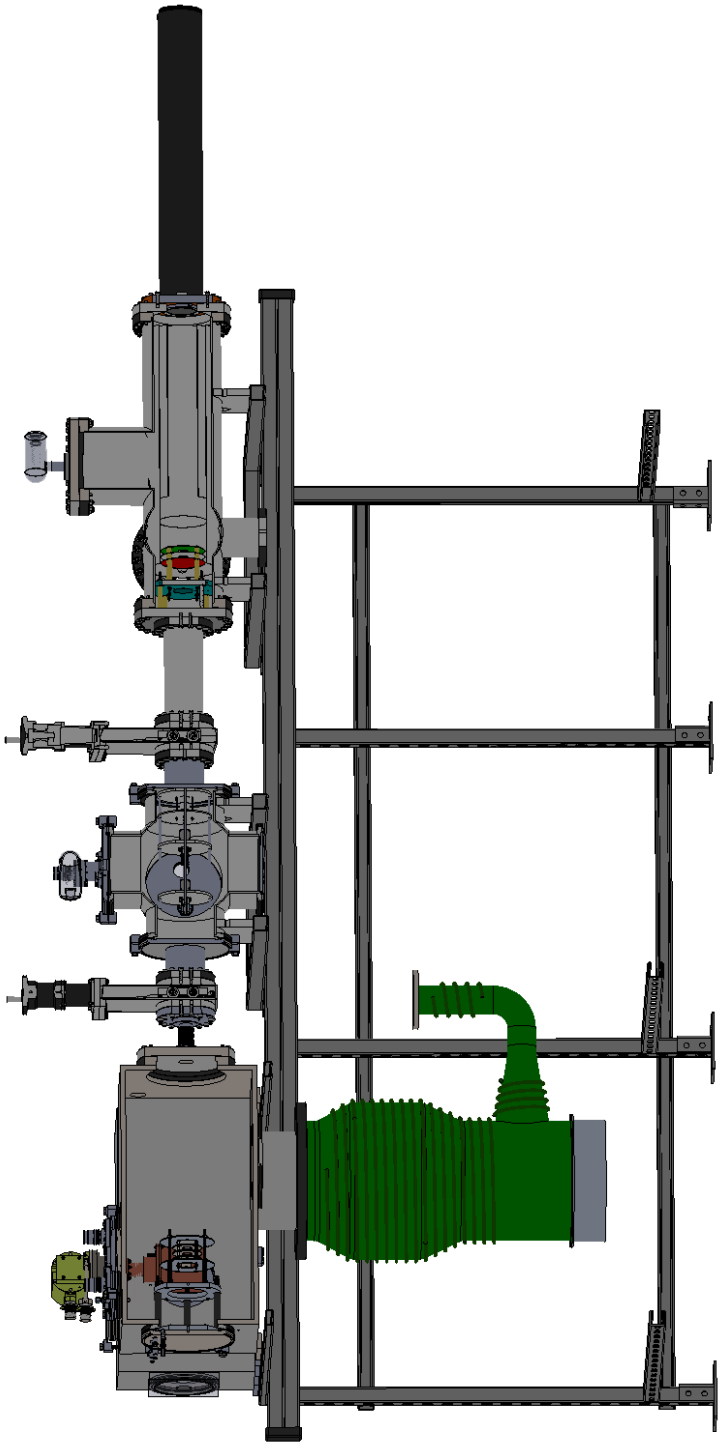

Figure 4.18c. Cutaway of the mass spectrometer side of the photoelectron velocity map imaging spectrometer with the QIT, showing all ion optics inside the chambers. Drawn to scale.

4.4 References for Chapter 4

1. P. E. Miler and M. B. Denton, J. Chem. Ed. **63** (1986).
2. R. E. March, Mass Spectrom. Rev. **28,** 961 (2009).
3. R. E. March, J. Mass Spec. **32** (1997).
4. W. Paul, H. P. Reinhardt, and U. v. Zahn, Z. f. Physik **152** (1958).
5. F. v. Busch and W. Paul, Z. f. Physik **164** (1961).
6. R. A. J. O'Hair, Chemical Communications**,** 1469 (2006).
7. D. Gerlich, in *State-selected and state-to-state ion-molecule reaction dynamics. Part 1: Experiment*; *Vol. 82*, edited by C.-Y. Ng and M. Baer (John Wiley & Sons, Inc., Freiburg, Germany, 1992), p. 1.
8. P. H. Dawson and C. Lambert, International Journal of Mass Spectrometry and Ion Physics **16,** 269 (1975).
9. G. Lawson and J. F. J. Todd, Anal. Chem. **49,** 1619 (1977).
10. J. E. Fulford and R. E. March, Intl. J. Mass Spec. Ion Phys. **30,** 39 (1979).
11. W. Paul, in *Nobel lectures, physics 1981-1990,* edited by G. Ekspong (World Scientific Publishing Co., Singapore, 1989).
12. I. Jordan TOF Products, in *Time of Flight Components: Ion Trap Time of Flight Products*; *Vol. 2016* (Jordan TOF Products, Inc., Grass Valley, CA, 2016).

Chapter 5

Conclusion and Future Works

The photoelectron velocity map imaging spectrometer performed efficiently when recording data for the diatomic molecules BeO^- and BeS^-. The $X\ ^2\Sigma^+ \rightarrow X\ ^1\Sigma^+$ transition of BeO^- was studied, and the electron binding energy was determined for the first time, with a value of 17535 ± 15 cm^{-1} (2.174 eV). Analysis of the spectra revealed that several detachment channels (ΔN = - 1, - 2, and – 3) became favorable when the photodetachment energy was near that of the detachment threshold. This favorability was due to the heightened probability of increasing the electron kinetic energy through rotational energy transfer, since slower electrons may allow extended interaction time for the mixing of rotational states. Also observed was the accidentally excited BeO^- (v = 3) dipole bound state.

The electron affinity of BeS was measured for the first time experimentally (18830 ± 17 cm^{-1}, 2.248(2) eV) from the excitation of the $X\ ^2\Sigma^+ \rightarrow X\ ^1\Sigma^+$ anion to neutral ground state transition. Once again, $\Delta N < 0$ dominated when the photon energy used for detachment was close to the detachment threshold. Autodetachment spectroscopy was used to observe the dipole-bound state $^2\Sigma^+$ – $X\ ^2\Sigma^+$ transitions, and it was found that the dipole-bound state 0 – 0 band origin was 141 ± 17 cm^{-1} below the detachment threshold, whereas the BeS^- (DBS, v = 1) level was 145 ± 25 cm^{-1} below BeS (X, v = 1) + e^-.

A notable point with both the BeO^- and BeS^- experiments was that the molecules created by laser ablation were vibrationally hot, as levels as high as $v = 3$ were observed. Currently, studies are being performed on the BeO_2^- anion but the spectra are difficult to characterize due to the high vibrational temperature of the anions. In order to achieve rotational resolution when photodetaching larger molecules and clusters, the spectrometer needed to be equipped with the ability to molecularly cool the anions. Designs were created for the implementation of a quadrupole ion trap (QIT) and quadrupole mass filter (QMF) into the velocity map imaging system. The QMF will provide mass-selection of the ions and guide them into the QIT, where they will be sufficiently cooled to a few Kelvin, allowing for the collection of rotationally-resolved velocity mapped images of heavier, polyatomic anions and metal clusters. Care was taken when designing the new system so that it will also have the capability of performing laser-induced fluorescence and resonantly-enhanced multi-photon ionization spectroscopies.

Once the new system is implemented, beryllium-containing polyatomic molecules such as BeS_2^- and BeO_2^- will be studied, as these molecules were observed by mass spectrometry when operating the ablation source in the previously described experiments. The system will also be capable of yielding resolvable spectra of beryllium cluster anions. The photoelectron velocity map imaging spectrometer and its ability to cool molecules will be an excellent means of gaining new insights into cluster growth, the bonding evolution of beryllium and its molecules, and details regarding the fundamental characteristics of beryllium-containing and other metal-containing molecules.